

AD A024346

**SUBSONIC TWO-DIMENSIONAL WIND TUNNEL INV  
OF THE HIGH LIFT CAPABILITY OF CIRCUI  
CONTROL WING SECTIONS**

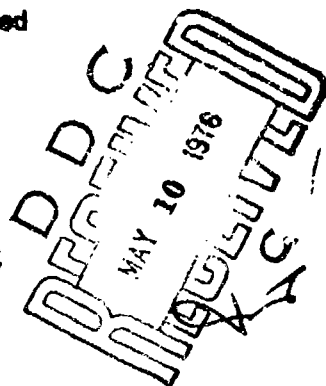
by

**Robert J. Englar**

**Approved for Public Release:  
Distribution Unlimited**

**Report ASED-274**

**April 1975**



UNCLASSIFIED

SECURITY CLASSIFICATION OF THIS PAGE (When Data Entered)

REPORT DOCUMENTATION PAGE		READ INSTRUCTIONS BEFORE COMPLETING FORM
1. REPORT NUMBER DINSRDC <del>ASD</del> /ASED-274	2. GOVT ACCESSION NO.	3. REPORT'S CATALOG NUMBER (9) Yept.
4. TITLE AND SUBTITLE SUBSONIC TWO-DIMENSIONAL WIND TUNNEL INVESTIGATIONS OF THE HIGH LIFT CAPABILITY OF CIRCULATION CONTROL WING SECTIONS		5. TYPE OF REPORT & PERIOD COVERED Final May 1972 - March 75
7. AUTHOR(s) Robert J. Englar		6. PERFORMING ORG. REPORT NUMBER
9. PERFORMING ORGANIZATION NAME AND ADDRESS David W. Taylor Naval Ship R&D Center Aviation and Surface Effects Department Bethesda, Maryland 20084		8. CONTRACT OR GRANT NUMBER(s) WF32-421 WF41-421
11. CONTROLLING OFFICE NAME AND ADDRESS Naval Air Systems Command AIR 320D Washington, D.C. 20361		10. PROGRAM ELEMENT, PROJECT, TASK AREA & WORK UNIT NUMBERS WE 32-421-212 (1660-120-30) WE 41-421-212 (1660-120-15)
14. MONITORING AGENCY NAME & ADDRESS (if different from Controlling Office)		12. REPORT DATE April 75
(12) 116 p.		13. NUMBER OF PAGES 107 +
16. DISTRIBUTION STATEMENT (of this Report)  Approved for Public Release: Distribution Unlimited		15. SECURITY CLASS. (of this report) Unclassified
17. DISTRIBUTION STATEMENT (of the abstract entered in Block 20, if different from Report)		15a. DECLASSIFICATION/DOWNGRADING SCHEDULE
18. SUPPLEMENTARY NOTES		
19. KEY WORDS (Continue on reverse side if necessary and identify by block number) High Lift Systems      Boundary Layer Control Circulation Control      Two-Dimensional Aerodynamics STOL Aircraft      Spoilers Tangential Blowing      Pulsed Blowing		
20. ABSTRACT (Continue on reverse side if necessary and identify by block number) Two series of Circulation Control Wing airfoil sections, formed by the conversion of the sharp trailing edge into a circular bluff surface with tangential upper surface blowing, were evaluated subsonically to determine their high lift characteristics as potential STOL wing sections. Parameters investigated which had noticeable effect on the blown airfoil performance include leading edge devices (type of device and degree of deflection), trailing edge configuration (radius, slot location, deflection, etc.), Reynolds number, airfoil incidence, momentum coefficient, slot height, (continued on back)		

DD FORM 1473

EDITION OF 1 NOV 65 IS OBSOLETE  
3/N 0102-014-6601

UNCLASSIFIED

SECURITY CLASSIFICATION OF THIS PAGE (When Data Entered)

387 695 46

SECURITY CLASSIFICATION OF THIS PAGE (When Data Entered)

and nozzle pressure ratio. Maximum lift coefficients roughly triple those of the flapped conventional sections were generated at incidence slightly less than the conventional stall angles and at blowing rates obtainable from bleed of state-of-the-art turbojet engines. An experimental investigation into the lift augmenting effects of pulsed unsteady blowing was conducted on a smaller radius trailing edge configuration. An additional investigation was conducted to determine the effects of spoilers or similar disturbances ahead of the jet exit. The results of the above investigations provide a data base for the prediction of the aerodynamic characteristics of aircraft employing Circulation Control trailing edges to increase their STOL capability.

100-557698

✓

100-557698

100-557698

100-557698

DISTRIBUTION

BY \_\_\_\_\_

DISTRIBUTION/AVAILABILITY C

Dist. \_\_\_\_\_

A

SECURITY CLASSIFICATION OF THIS PAGE(When Data Entered)

## TABLE OF CONTENTS

	Page
SUMMARY . . . . .	1
INTRODUCTION . . . . .	1
DESIGN CONSIDERATIONS . . . . .	3
MODELS AND EXPERIMENTAL APPARATUS . . . . .	4
MODELS . . . . .	4
EXPERIMENTAL APPARATUS AND TECHNIQUE . . . . .	5
RESULTS AND DISCUSSION . . . . .	6
NACA 66-210/CCW AIRFOIL . . . . .	6
Lift Augmentation . . . . .	6
Reynolds Number Effects . . . . .	9
Drag . . . . .	9
Pitching Moment . . . . .	10
NACA 64A-212/CCW AIRFOIL . . . . .	10
Lift Augmentation . . . . .	11
Slot Height Variation . . . . .	13
Reynolds Number Effects . . . . .	14
Drag . . . . .	15
Pitching Moment . . . . .	15
PULSED BLOWING INVESTIGATION . . . . .	16
SPOILER INVESTIGATION . . . . .	19
CONCLUSIONS . . . . .	20
RECOMMENDATIONS . . . . .	23
ACKNOWLEDGEMENT . . . . .	24
REFERENCES . . . . .	25
APPENDIX A - MODELS, EXPERIMENTAL APPARATUS, AND TECHNIQUE . . . . .	27

## LIST OF TABLES

Table I - Geometric Properties of NACA 66-210/CCW Airfoil Sections . . . . .	33
Table II - Geometric Properties of NACA 64A-212/CCW Airfoil Sections . . . . .	34

# LIST OF FIGURES

	Page
Figure 1 - Circulation Control Wing Modes of Operation, Short Chord Flap Configuration . . . . .	35
Figure 2 - Extended Trailing Edge Configuration . . . . .	36
Figure 3 - Model Geometry, NACA 66-210/CCW Airfoil . . . . .	37
Figure 4 - Model Geometry, NACA 64A-212/CCW Airfoil . . . . .	38
Figure 5 - 2-D Elliptic CC Airfoil with Spoilers Installed . . . .	39
Figure 6 - 2-D Inserts and NACA 64A-212/CCW Model Installed in 8- x 10-Foot South Subsonic Tunnel . . . . .	40
Figure 7 - Configuration CCW 243 Installed on Insert Turntables with Tangential Wall Blowing . . . . .	41
Figure 8 - Aft View Showing Wake Rake, Model, and Tangential Wall Blowing . . . . .	42
Figure 9 - Lift as a Function of Blowing for the NACA 66-210/CCW Airfoils, $q = 30$ psf, $Re \approx 0.64 \times 10^6$ , $h = 0.009"$ . .	43
Figure 10 - Effect of Droop on Preventing Leading Edge Separation, NACA 66-210/CCW Airfoil, $\alpha_c = 8.4^\circ$ , $C_{\mu} \approx 0.11$ , Experimental Pressure Distributions . . . . .	47
Figure 11 - Effect of Blowing on Experimental Pressure Distributions for NACA 66-210/CCW Airfoil, $\delta_{LE} = 43.6^\circ$ , $\alpha_c = -0.86^\circ$ . . . . .	48
Figure 12 - Effect of Incidence on NACA 66-210/CCW with No Leading Edge Droop at $C_{\mu} \approx .088$ , Experimental Pressure Distributions . . . . .	49
Figure 13 - Effect of Incidence on NACA 66-210/CCW Airfoil with $2^\circ$ Leading Edge Droop at $C_{\mu} \approx 0.173$ , Experimental Pressure Distributions . . . . .	50
Figure 14 - Lift Curves at Constant Momentum Coefficient for 66-210/CCW Airfoils, $q = 30$ psf, $Re \approx 0.64 \times 10^6$ , $h = .009"$ . . . . .	51
Figure 15 - $C_{l_{max}}$ and $\alpha_{STALL}$ as Functions of Momentum Coefficient and Nose Droop Angle for 66-210/CCW Airfoils . . . . .	55
Figure 16 - $C_{l_{max}}$ as a Function of Droop and Momentum Coefficient, NACA 66-210/CCW Airfoils . . . . .	56
Figure 17 - Effects of Reynolds Number on Lift Coefficient for NACA 66-210/CCW Airfoil, CCW 800, $\delta_{LE} = 0^\circ$ , $h = .009"$ . . .	57
Figure 18 - Drag as a Function of Blowing for the NACA 66-210/CCW Airfoils, $q = 30$ psf, $Re = 0.64 \times 10^6$ , $h = 0.007"$ . .	58
Figure 19 - Pitching Moment as a Function of Blowing for the NACA 66-210/CCW Airfoils, $q = 30$ psf, $Re = 0.64 \times 10^6$ , $h = 0.009"$ . . . . .	62

	Page
Figure 20 - Lift as a Function of Blowing for NACA 64A-212/CCW Airfoils, $q = 30$ psf, $R_e \approx 1.98 \times 10^6$ , $h = 0.027''$ . . .	66
Figure 21 - Small and Large Chord CCW Airfoil Comparison . . . . .	71
Figure 22 - Effects of Reduced Trailing Edge Radius - Comparison Between Configuration CCW 241 and CCW 244 Experimental Pressure Distributions . . . . .	72
Figure 23 - Lift Curves at Constant Momentum Coefficient for 64A-212/CCW Airfoils, $q = 30$ psf, $R_e = 1.98 \times 10^6$ , $h = .027''$ . . . . .	74
Figure 24 - Effective Incidence Corrections for Configuration CCW 241 . . . . .	79
Figure 25 - Lift Curve Comparison for the 64A-212/CCW Airfoils at $C_u = 0.16$ , $\alpha_g \leq 15^\circ$ , $h = .027''$ , $q = 30$ psf . . . . .	80
Figure 26 - Maximum Lift Coefficients within Test Limitations for 5 Configurations of a C.C. Wing on a 2-D NACA 64A212 Airfoil ( $\alpha_g \leq 15^\circ$ , $h = .027''$ , $q = 30$ psf) . . . . .	81
Figure 27 - $C_{l_{max}}$ and Stall Angles for the 64A-212/CCW Airfoils ( $h = .027''$ , $q = 30$ psf) . . . . .	82
Figure 28 - Slot Height and Dynamic Pressure Effects on $C_u$ , CCW 241, $\alpha_g = 9^\circ$ , $c = 24''$ . . . . .	83
Figure 29 - Slot Height and Pressure Ratio Effects on CCW 241, $\alpha_c = 9^\circ$ . . . . .	84
Figure 30 - Slot Height Effects on CCW 244, $\alpha_c = 0^\circ$ . . . . .	85
Figure 31 - Effect of Reynolds Number on Lift, CCW 245 ( $\delta_{LE} = 0^\circ$ , $\delta_f = 180^\circ$ ), $\alpha_c = 0^\circ$ , $h = .027''$ . . . . .	86
Figure 32 - Drag as a Function of Blowing for NACA 64A-212/CCW Airfoils, $q = 30$ psf, $R_e \approx 1.98 \times 10^6$ , $h = 0.027''$ . . .	87
Figure 33 - Drag Coefficient at $C_{l_{max}}$ within Test Limits for NACA 64A-212/CCW Airfoils, $\alpha_g \leq 15^\circ$ , $h = 0.027''$ , $q = 30$ psf . . . . .	92
Figure 34 - Pitching Moment Variation with Blowing for CCW 241, $h = 0.027''$ , $q = 30$ psf . . . . .	93
Figure 35 - Pitching Moment as a Function of Lift, Incidence and $C_u$ for NACA 64A-212/CCW Airfoils ( $h = .027''$ , $q = 30$ psf) . . . . .	94
Figure 36 - Pitching Moment Coefficient at $C_{l_{max}}$ within Test Limits for NACA 64A-212/CCW Airfoils, $\alpha_g \leq 15^\circ$ , $h = 0.027''$ , $q = 30$ psf . . . . .	99
Figure 37 - Mean Lift and Momentum Coefficients as Functions of Pulsing Rate, CCW 244 . . . . .	100
Figure 38 - Mean Mass Flow Measured by the Venturimeter, CCW 244 . . . . .	101
Figure 39 - Corrected Mean Lift and Momentum Coefficients as Functions of Pulse Rate, CCW 244 . . . . .	102

	Page
Figure 40 - Effect of Spoiler Deflection on Lift of Elliptical C.C. Airfoil ( $\alpha_g = 0^\circ$ , $q = 20$ psf, $h = .009"$ ) . . . . .	103
Figure 41 - Lift Loss as a Function of Spoiler Deflection . . . . .	104
Figure 42 - Reynolds Number and Flow Reattachment Effects on Elliptical C.C. Airfoil with Spoiler . . . . .	105
Figure 43 - Drag Increase due to Spoiler Deflection on Elliptical C.C. Airfoil . . . . .	106
Figure 44 - Pitching Moment Variation with Spoiler Deflection . . .	107

# SYMBOLS

$A_j$	jet exit area, ft <sup>2</sup>
$c$	airfoil undeflected chord, ft*
$c'$	deflected, rotated, or effective chord, ft*
$C_a$	section axial force coefficient
$C_d$	section drag coefficient
$C_{d\text{rake}}$	section drag coefficient from integrated momentum loss on wake rake
$C_l$	section lift coefficient
$\overline{C}_l$	mean section lift coefficient during pulsed blowing
$C_{l\text{clean}}$	section lift coefficient of airfoil with spoiler retracted
$C_{l\text{max}}$	section maximum lift coefficient
$C_{L\text{max}}$	aircraft maximum lift coefficient
$C_{l_\alpha}$	lift curve slope, per degree
$C_{m25}$	section quarter-chord pitching moment coefficient
$C_n$	section normal force coefficient
$C_p$	pressure coefficient, $\frac{p-p_\infty}{q}$
$C_\mu$	section momentum coefficient, $\frac{\dot{m}V_j}{qS}$
$\overline{C}_{\mu 1}$	mean momentum coefficient during pulsed blowing as measured by venturimeter
$\overline{C}_{\mu 2}$	calculated mean momentum coefficient during pulsed blowing
$h$	jet exit nominal slot height, ft*
$h_t$	tunnel height, ft
$\dot{m}$	measured jet mass efflux, slugs/sec

\* unless otherwise noted



$\dot{M}$	mean jet mass efflux during pulsed blowing, slugs/sec
$p$	local static pressure, psfa
$P_d$	plenum (duct) total pressure, psfa
$\bar{P}_d$	mean plenum total pressure during pulsed blowing, psfa
$P_{d_{max}}$	maximum plenum total pressure during pulsed blowing, psfa
$P_v$	line pressure upstream of venturimeter, psia
$P_\infty$	freestream static pressure, psfa
$q$	freestream dynamic pressure, psf
$R$	universal gas constant, 1715 ft <sup>2</sup> /(sec <sup>2</sup> °R)
$r$	trailing edge radius, ft*
$Re$	Reynolds number based on undeflected chord
$S$	wing or airfoil planform area, ft <sup>2</sup>
$t$	airfoil thickness, ft*
$T_d$	plenum total temperature, °R
$u_{max}$	maximum velocity in the wall jet velocity profile, ft/sec
$V_j$	isentropic jet velocity, ft/sec
$V_\infty$	freestream velocity, ft/sec
$x$	distance from undeflected leading edge, ft*
$x_{slot}$	slot location from undeflected leading edge, ft*
$\alpha_c$	corrected incidence; $\alpha_g$ corrected for tunnel boundary constraints, deg
$\alpha_{eff}$	effective incidence; $\alpha_c$ corrected for induced downwash effects, deg
$\alpha_g$	geometric incidence relative to chord, deg
$\alpha_{stall}$	stall incidence, deg

---

\* unless otherwise noted

$\gamma$	ratio of specific heats
$\delta$	mean line maximum camber relative to chord line, ft
$\delta_f$	flap deflection angle relative to chord, deg
$\delta_j$	jet deflection angle relative to chord, deg
$\delta_{LE}$	leading edge deflection angle relative to chord, deg
$\delta_s$	spoiler deflection angle relative to chord, deg
$\epsilon$	solid blockage correction factor
$\lambda_2$	two-dimensional airfoil shape factor
$\rho$	freestream density, slugs/ft <sup>3</sup>
$\rho_j$	density in the jet throat (exit), slugs/ft <sup>3</sup>
$\omega$	pulsed blowing frequency, cycles/sec

## SUMMARY

Two series of Circulation Control Wing airfoil sections, formed by the conversion of the sharp trailing edge into a circular bluff surface with tangential upper surface blowing, were evaluated subsonically to determine their high lift characteristics as potential STOL wing sections. Parameters investigated which had noticeable effect on the blown airfoil performance include leading edge devices (type of device and degree of deflection), trailing edge configuration (radius, slot location, deflection, etc.), Reynolds number, airfoil incidence, momentum coefficient, slot height, and nozzle pressure ratio. Maximum lift coefficients roughly triple those of the flapped conventional sections were generated at incidence slightly less than the conventional stall angles and at blowing rates obtainable from bleed of state-of-the-art turbojet engines. An experimental investigation into the lift augmenting effects of pulsed unsteady blowing was conducted on a smaller radius trailing edge configuration. An additional investigation was conducted to determine the effects of spoilers or similar disturbances ahead of the jet exit. The results of the above investigations provide a data base for the prediction of the aerodynamic characteristics of aircraft employing Circulation Control trailing edges to increase their STOL capability.

## INTRODUCTION

Recent investigation into the application to helicopter rotors of Circulation Control elliptical airfoils employing tangential blowing over bluff trailing edges has demonstrated the simultaneous generation of high lift and drag at low blowing rates and low angles of incidence (Reference 1). The concept offers promise of considerable payoff in STOL performance when applied to the more conventional airfoil sections of fixed wing aircraft. Based on the well-known Coanda principle, this Circulation Control Wing (CCW) concept involves converting the sharp trailing edge of the high speed cruise airfoil into a rounded surface to which a jet of air, blown tangentially from the upper surface, adheres. The jet sheet is able to turn nearly 180 degrees around the bluff

afterbody, initially acting as a boundary layer control, but primarily controlling the airfoil stagnation points and thus the circulation. The resulting high augmentation of circulation lift is obtained at values of blowing or momentum coefficient ( $C_{\mu}$ ) well within the ranges of mass flow and pressure which can be bled from state-of-the-art turbojet and turbofan engines. A problem frequently encountered with blown flap concepts is the conversion of the blowing momentum into wing thrust, and thus reduction of drag needed to maintain a low equilibrium approach velocity at large glide path angles. This is avoided by the Circulation Control concept, as large jet turning produces viscous mixing with the lower surface freestream, and jet thrust recovery is significantly reduced.

Application of the CCW to fixed wing carrier-based Naval aircraft is expected to produce considerable reduction in approach velocities and/or landing distances, increased aircraft payload and wing loadings, and the independence of high speed wing design from compromise resulting from low speed landing and takeoff requirements. In addition, the generation of lift independent of incidence implies increased pilot visibility during carrier approach. The existence of an aft upper surface blowing source provides the additional possibility for increased transonic maneuverability.

A characteristic Circulation Control Wing configuration is shown in Figure 1, where a short chord flap is rotated through 180 degrees to expose the cylindrical Coanda surface. Replacement of the conventional half-span single slotted flap of a 1/5-scale model T-2C aircraft with a Coanda trailing edge very similar to this configuration resulted in increases of 96 percent in  $C_{L_{max}}$  and 240 percent in the corresponding drag coefficient at  $C_{\mu} = 0.156$  (References 2 and 3). However, full rotation of the flap in this configuration results in a loss in chord of about 11 percent; additional lift augmentation should result if this loss can be eliminated. The extended configuration of Figure 2 was thus proposed, where the Coanda surface translates aft to the trailing edge as a split flap is deployed to form the lower surface.

It is the primary objective of the present investigation to provide section aerodynamic data on the above and additional CCW configurations for use as input to analyses for prediction of three-dimensional performance. This report also documents a preliminary investigation conducted on a small chord airfoil model which was used to confirm the effectiveness of the Coanda trailing edges on relatively thin conventional airfoil sections. In addition, it was desired to investigate the effects of unsteady pulsed blowing on the lift augmentation of CCW airfoils, and the effects of deflecting a spoiler or similar disturbance upstream of the blowing slot. Further goals of this investigation were to identify a leading edge device capable of preventing laminar separation under conditions of high circulation, and to examine the effects of Reynolds number and trailing edge parameter variation on overall airfoil performance.

#### DESIGN CONSIDERATIONS

Airfoil sections to be modified included those thought to be characteristic of state-of-the-art fixed wing aircraft. For the preliminary investigation on the small chord airfoil, an NACA 66-210 profile was chosen. A larger chord NACA 64A-212 airfoil was constructed to provide section data to correspond to the T-2C/CCW model of Reference 2. Previous 2-D investigations of 15-percent thick elliptic CC airfoils (Reference 4) indicated a serious problem with leading edge separation at high lift, and a primary concern of the 66-210/CCW investigation was the determination of sufficient means to prevent that problem. A Krüger leading edge flap and a leading edge droop were alternately incorporated for this purpose. The trailing edge geometries for both small and large chord models were based on those parameters which had proven effective in CC rotor airfoil evaluations. References 5 and 6 suggest that strongly attached Coanda flow is maintained for a slot height-to-radius ratio in the range  $0.01 \leq h/r \leq 0.05$ , while effective Coanda jet turning and lift augmentation result from a trailing edge radius-to-chord ratio in the range  $0.02 \leq r/c' \leq 0.05$ . This produces a slot-height-to-chord ratio of approximately  $0.0005 \leq h/c' \leq 0.0025$ ,

the lower limit being postulated as the point at which nozzle internal boundary layer thickness approaches the slot height (jet exit thickness) and seriously degrades the "potential core" characteristics of the jet. Once the trailing edge radius is chosen, the flap rotation point for the configuration of Figure 1 is determined by positioning the center of the radius at the airfoil chordwise location where the sum of radius plus slot height is equal to local airfoil thickness. This determines the length of the rotating flap chord and the slot longitudinal location. For most thinner airfoils, the resulting flap chord will be roughly 10 to 20 percent of the original or undeflected chord,  $c$ , and the slot location will be approximately  $.80c$  to  $.90c$ , or aft of 93 percent of the rotated chord  $c'$  (defined as the distance from the undeflected leading edge to the furthest aft point on the Coanda surface). It is essential that this resulting slot location be slightly ahead of the adverse pressure gradient downstream of the suction peak produced by attached flow accelerating around the bluff trailing edge. A more forward slot location can delay section stall due to better boundary layer control on the upper surface, but a slightly more aft slot produces higher lift augmentation due to higher jet momentum at the airfoil trailing edge. For the extended configuration of Figure 2, the slot location is at the original trailing edge, the effective chord  $c'$  is  $c + r$ , and limits on  $h/r$ ,  $r/c'$  and  $h/c'$  are the same as above. It should be noted that all nondimensional data in this report are referenced to the original undeflected chord  $c$  (or original planform area  $S$ ) regardless of the value of the effective chord  $c'$ ; all data are thus directly comparable. Also, incidence is relative to the chord line through the undeflected leading and trailing edge points of the conventional airfoil.

## MODELS AND EXPERIMENTAL APPARATUS

### MODELS

Based on the design considerations of the previous section, two airfoil sections were modified into various configurations of the Circulation Control Wing. A small chord (undeflected  $c = 8.0$  inches)

NACA 66-210 section was converted into the rotated flap configuration of Figure 1 and is shown in Figure 3. Krüger leading edge flaps of 5, 10 and 15 percent undeflected chord were initially employed for leading edge separation control, but due to their relative ineffectiveness, were replaced with a leading edge droop, hinged at the lower surface at .15c and deflected at angles of 0, 15.3, 29 and 43.6 degrees from the chord. These configurations are identified as CCW800, CCW815, CCW829, and CCW844 respectively. Additional details of the model are found in Appendix A, while geometric parameters are listed in Table 1.

A large chord ( $c = 24.0$  inches) model NACA 64A-212 was converted to include the .15c leading edge droop and a number of trailing edge variations. Figure 4 depicts this model, with additional details found in Appendix A and geometric parameters in Table II. Configuration CCW241 was similar to CCW829, including a  $30^\circ$  droop and  $180^\circ$  rotated flap. CCW242 was similar except the flap deflection was  $90^\circ$ . An extended trailing edge configuration similar to that of Figure 2 and with  $30^\circ$  leading edge droop comprised CCW243, while CCW244 was the same as CCW243 but with a reduced trailing edge radius having roughly half the value of  $r/c'$ . An investigation of pulsed blowing was also performed with this model. Configuration CCW245 was CCW241 with no leading edge droop.

A third model was employed to investigate the effects of upper surface distortions or deflections of control surfaces such as spoilers ahead of the slot. This model was a 20.6-percent thick cambered ellipse section characteristic of a rotor blade airfoil, and is shown in Figure 5. A 9.82-percent-chord spoiler with the hinge at 70-percent chord could be deflected up to 51 degrees relative to the chord line of the 10.18 inch model.

#### EXPERIMENTAL APPARATUS AND TECHNIQUE

The small chord 66-210/CCW model was installed and evaluated in the David W. Taylor Naval Ship Research and Development Center (DTNSRDC) 15- x 20-inch subsonic tunnel. For this model, as well as all the others, lift and moment coefficients were obtained from integration of surface static pressures near the midspan as recorded by a 144- port scannivalve system. Drag coefficient was obtained from integration of wake momentum

deficit as measured on a total head wake rake. Additional details relating to model installation; test apparatus and technique; data reduction and corrections; and control of tunnel two-dimensionability are presented in Appendix A. The 64A-212/CCW airfoil and the cambered ellipse section were installed in the two-dimensional parallel wall insert which converted the DTNSRDC 8- x 10-foot subsonic tunnel into a 3- x 8-foot 2-D channel. Figure 6 shows this installation, while Figures 7 and 8 show configuration CCW243 installed within the inserts, and details of the wall blowing slots and wake rake. Again, Appendix A presents further details of installation and technique, and references additional sources of explanation.

A fourth series of investigations was conducted to determine the effects of pulsed (unsteady) trailing edge blowing upon lift augmentation. Modifications made to the air supply system and data acquisition and reduction are explained in Appendix A. The model used was the CCW244 configuration of the 64A-212 airfoil.

## RESULTS AND DISCUSSION

### NACA 66-210/CCW AIRFOIL

As mentioned previously, the investigation of this smaller chord airfoil was primarily intended to confirm the effectiveness of Coanda type trailing edges applied to thin, cambered conventional airfoils for high lift generation, and to identify satisfactory leading edge devices to prevent flow separation caused by rapid flow acceleration around rather small leading edge radii. The following data shows that, indeed, lack of proper leading edge devices can produce quite severe consequences in lift augmentation, drag generation and pitching moments.

#### Lift Augmentation

Section lift coefficients, as determined from static pressure integration, are presented as functions of momentum coefficient at constant corrected incidence ( $\alpha_c$ ) for four different nose droop angles in Figure 9. Here, the coefficients are corrected for solid blockage and



tunnel boundary interference, but not for any induced effect which might result from spanwise non-uniformity due to interaction between trailing edge adverse pressure gradient and tunnel wall boundary layer (see Reference 7). The corrected incidence  $\alpha_c$  has been adjusted to account for tunnel boundary corrections. At low and negative incidence, all four configurations show a rapid rise in  $C_L$  with blowing. This initial rise is attributed to flow entrainment and boundary layer control, while the less steep slope at higher  $C_\mu$  is characteristic of stagnation point movement by the Coanda jet and resulting supercirculation. However, at low droop angles, as higher incidence is approached, a noticeable break in the curve occurs. The pressure distributions in Figure 10 for  $\alpha_c = 8.4^\circ$  and  $C_\mu \approx 0.11$  very clearly show leading edge separation at  $0^\circ$  droop and reattachment of the flow at higher droop. Furthermore, attached leading edge flow results in considerably higher trailing edge suction peaks at a constant  $C_\mu$ , indicating greater jet turning, flow entrainment, and lift augmentation. The inset plot shows an increase of over 1.5 in  $C_L$  produced by applying a  $43.6^\circ$  nose droop. As Figures 9 (c) and (d) show, the lift break is delayed by nose droop to much higher values of incidence.

Insight into the mechanism of lift augmentation due to blowing is given by Figure 11. With no blowing, the leading edge stagnation point is on the upper surface of the  $43.6^\circ$  drooped nose, but as  $C_\mu$  is increased, it moves to the lower surface, which approaches full stagnation ( $C_p \rightarrow 1.0$ ) along the entire bottom. On the upper surface, a suction spike at the droop knee is followed by a moderate adverse pressure gradient which leads, at higher  $C_\mu$ , to a long favorable gradient terminating somewhere aft of  $0.97c'$ . This high upper surface suction and lower surface overpressure result in high  $C_L$  at quite low  $C_\mu$ . Figures 12 and 13 present the effect of incidence on airfoil pressure distributions and lift with and without nose droop. At  $C_\mu \approx .088$  and  $\delta_{LE} = 0^\circ$ , Figure 12 shows serious leading edge separation at incidence of  $-0.68$  degrees and higher. This corresponds to the lift breaks in Figure 9 (a). For  $29^\circ$  droop and  $C_\mu \approx .173$  (Figure 13), higher incidence produces only slight separation at the leading edge but the major effect is gradual reduction in the suction peak at the knee of the droop, and much more pronounced reduction

in the trailing edge suction peak. Small changes in the leading edge flow apparently can quite strongly affect the boundary layer and downstream pressure distributions. As soon as the trailing edge peak begins to reduce (at incidence above 3.2 degrees for  $C_\mu \approx .17$ ) the lift break in Figure 9 (c) begins.

Figure 14 presents lift curves at constant  $C_\mu$ , obtained as crossplots of Figure 9. For all leading edge droop angles, stall occurs at progressively lower incidence with increased blowing; for no droop,  $\alpha_{\text{stall}}$  takes on negative values. As droop is increased, stall occurs at higher incidence, and lift augmentation due to blowing is supplemented by lift due to positive incidence. Figure 15 is a summary plot of this data, showing  $C_{l_{\text{max}}}$  and  $\alpha_{\text{stall}}$  as functions of blowing rate and droop angle. A comparison is made to the conventional NACA 66-210 with a 60° split flap (from Reference 8) operating at five times the test Reynolds number of the CCW airfoil. An increase of 250 percent in  $C_{l_{\text{max}}}$  is seen for the blown airfoil with  $\delta_{\text{LE}} = 43.6^\circ$  and  $C_\mu = 0.24$ ; operating at the same Reynolds number would produce an even larger increase. Figure 14 (d) shows a similar comparison of the blown and conventional airfoil. Also shown is the data resulting from the 0.15c Krüger leading edge flap at  $C_\mu = .142$ ; the loss of effectiveness due to lack of leading edge flow control is evident. Figure 16 presents maximum lift coefficient as a function of  $C_\mu$ ; in both this figure and Figure 15, it appears that the additional benefits of increasing droop from 29 to 43.6° are minimal. In fact, at lower blowing, higher droop reduces  $C_{l_{\text{max}}}$  due to suction on the lower surface of the leading edge. A droop of roughly 30 degrees appears to be more optimum over the entire  $C_\mu$  range, but a more effective use of droop would be to schedule  $\delta_{\text{LE}}$  as a function of  $C_\mu$  and incidence. However, the pressure distributions of Figure 13 suggest that, in spite of the droop's effectiveness, a device offering stronger control of the leading edge boundary layer (such as a slat or tangential leading edge blowing) might further improve the lift augmentation of this type of airfoil.

### Reynolds Number Effects

The majority of the preceding data was run at a nominal freestream dynamic pressure of 30 psf, yielding for this small chord model a Reynolds number of  $0.64 \times 10^6$  (based on undeflected chord  $c$  and corrected for model blockage). Figure 17 shows the effects of Reynolds number on lift for two incidences and two blowing rates for dynamic pressure from 10 to 57 psf. At  $C_{\mu} = 0$ , increase in  $R_e$  produces a slight increase in  $C_L$ , but above  $0.7 \times 10^6$  the difference appears negligible. However, with blowing, the increase in  $C_L$  with  $R_e$  is greater. The magnitude of this trend with higher  $C_{\mu}$  and  $R_e$  is not evident from this data. Additional evaluation will have to be achieved using the larger chord 64A-212 section data. It should also be mentioned here that maintaining a constant  $C_{\mu}$  requires higher jet pressure ratios and velocities ( $P_d/P_{\infty}$  and  $V_j$ ) at higher Reynolds number. The kinetic energy of the jet (proportional to  $V_j^3$ ) and jet turning thus increases with Reynolds number at constant  $C_{\mu}$  so that increments in the Figure 17 curves with blowing may not be due solely to  $R_e$ .

In the data of Figure 9, air supply limitations produced an upper  $C_{\mu}$  limit of roughly 0.12 at  $q = 30$  psf. Additional  $C_{\mu}$  up to 0.20 was obtained by reducing the dynamic pressure to 20 psf. The flagged data points of Figure 9 are obtained at this reduced Reynolds number, but the curves are faired slightly above these points using the increments of Figure 17, so that they are indicative of data for  $R_e \approx 0.64 \times 10^6$ .

### Drag

Drag measurements taken by a rake employing 54 total head probes and 8 static probes were integrated using the methods of Betz and Jones (Reference 9) and modified (see References 5, 7, and 10) to account for the additional momentum of the jet so that

$$C_d = C_{d_{\text{rake}}} - \frac{\dot{m} V_{\infty}}{qc} = C_{d_{\text{rake}}} - C_{\mu} \frac{V_{\infty}}{V_j}$$

where  $\dot{m}$  is slugs/sec/ft of span in this case.

For most blown airfoil concepts, the jet momentum is converted into thrust, and drag is reduced with blowing. As Figure 18 shows, the same is true of the CCW at low blowing rates and moderate incidence. However, as higher  $C_u$  is reached, the jet turns further around the bluff trailing edge and into the oncoming freestream, producing a large viscous wake and increased profile drag. Also, as Figure 18 (a) in particular shows, as soon as the lift break due to leading edge separation occurs, drag rises very rapidly, even though lift drop-off has not occurred (i.e., no " $C_u$  - stall" has developed). Also to be noted are the high values of zero blowing drag at low and negative incidence for increased nose droop, due primarily to separation from the underside of the nose.

#### Pitching Moment

As is typical of most blown airfoil schemes, the increased suction spike far aft on the airfoil generates rather large nose-down pitching moments about the quarter chord (0.25 undeflected chord). Figure 19 shows this to be the case with CCW sections as well, with largest values of nose-down moment occurring for low incidence and high blowing. Higher incidence of course adds leading edge suction peaks which oppose those at the trailing edge, and  $C_{m_{25}}$  becomes less negative when flow remains attached. A similar result occurs with little or no droop, but is caused by the separated flow reducing the jet effectiveness of the aft surface and thus the nose-down pitching moment. In general, however, the conditions of highest jet efficiency are also those of largest nose-down moment.

#### NACA 64A-212/CCW AIRFOIL

Based on the initial confirmation by the 66-210/CCW section of high lift and drag generation at low incidence and blowing, and on the identification of roughly 30° droop as an effective leading edge device, the 64A-212/CCW section was tested to investigate: additional trailing edge configurations; effects of higher Reynolds number and slot height variations; and the aerodynamic properties of the airfoil section employed in the T-2C/CCW investigations of Reference 2. The configurations have

been identified in the previous section on models and in Figure 4, and the geometric parameters are listed in Table II.

### Lift Augmentation

Figure 20 presents lift as a function of  $C_{\mu}$  at constant corrected incidence for five configurations, all run at a dynamic pressure of 30 psf and slot height of 0.027 inches. The lift break due to leading edge problems at higher incidences on the 66-210/CCW is still observed, although for similar configuration (CCW829 and CCW241) it now appears to be occurring at much higher incidence and greater  $C_L$  for the larger chord model. Figure 21 shows a clearer comparison of these airfoils. At zero incidence, the relatively small difference in  $C_L$  is probably due to Reynolds number, while at  $9^\circ$  geometric incidence, the much larger differences are probably due to more severe separation on the smaller leading edge radius of the 66-210 airfoil. Leading edge separation control on CCW241 allows this airfoil to generate  $C_L = 5.75$  at  $C_{\mu} = 0.19$  and  $\alpha_g = 9^\circ$  with a chord that is shortened 11.4 percent from the undeflected value. The pressure distributions for the 64A-212 airfoils show trends very similar to Figures 11, 12, and 13 for the smaller airfoil. In Figure 20 (e), CCW245 (no leading edge droop) displays separation problems similar to CCW800 in Figure 9 (a). Increased Reynolds number and nose radius appear to produce little improvement for the undrooped airfoils.

Configurations 242, 243, and 244 display the effects of trailing edge geometry variation, Figure 20 (b), (c), and (d). The  $90^\circ$  flap, an intermediate rotation angle for the shortened chord configuration of Figure 1, generates high  $C_L$  due primarily to the large effective camber and the fact that no chord loss exists in this partially rotated configuration. However, at higher  $C_{\mu}$ , operation at incidence above 0 degrees produces stall (i.e., decreased  $C_L$  with increased  $\alpha$ ). The reduced radius trailing edge configuration (CCW 244,  $r/c' = .021$ ) shows rather interesting trends when compared to the larger radius ( $r/c' = .041$ ) of CCW241 for incidence of 6 degrees and less. Figure 22 (a) indicates that for no blowing and  $\alpha_g = 3^\circ$ , the aft lower surface camber produced by the rotated flap produces additional  $C_L$  for the larger radius trailing edge. However

at higher  $C_{\mu}$ , the reduced radius trailing edge sustains pressure coefficients roughly twice that of CCW241 at the same blowing; this increased jet turning and entrainment produces significant additional  $C_L$ . At higher incidence, Figure 22 (b) shows the larger radius produces greater  $C_L$  in all cases. The aft camber predominates at low blowing, and the slightly farther forward slot (in terms of actual deflected chord) of CCW241 provides better upper surface boundary layer control at high incidence and higher  $C_{\mu}$ , even though the smaller radius still provides better jet turning. The extended trailing edge configuration (CCW243 of Figure 4) shows significant lift increase over CCW241 by regaining the chord lost during the airfoil's flap rotation. A  $C_{\mu}$  limit of roughly 0.08 was imposed by the model's long unsupported upper plenum surface between the adjustment screws; this expanded under pressure and consequently closed the blowing slot. However, based on similarity to CCW241, it is felt that the extrapolation to higher  $C_{\mu}$  in Figure 20 (c) is valid.

The more conventional lift curves ( $C_L$  vs  $\alpha_c$  at constant  $C_{\mu}$ ) are plotted in Figure 23, where the conventional 64A-212 data from Reference 8 is compared in Figure 23 (a). All configurations except CCW245 produce increases of at least 215 percent in  $C_{L_{max}}$  at  $C_{\mu} = .16$  over the conventional split flap airfoil at  $Re = 6 \times 10^6$ . Configurations 241, 243, and 244 all possess the conventional lift curve shapes with parallel slopes and positive stall angles, decreasing somewhat with increased  $C_{\mu}$  (analogous to increased conventional flap deflection). However, CCW242 and 245 possess low or negative stall angles at higher  $C_{\mu}$ , both apparently experiencing leading edge problems. The  $90^\circ$  flap data shows very little parallelism in lift curve slope. The operation of both airfoils seem to suggest problems in areas of positive  $\alpha$ -operation (such as gusts or conventional landing flares) and in systems to control blowing and incidence schedules in these regions of operation.

In Figure 23, additional dashed curves are provided which correspond to the actual effective incidence,  $\alpha_{eff}$ , at which the airfoil operates. These values are obtained from curves similar to Figure 24 for each airfoil. The effective incidence is  $\alpha_c$  modified as described in Appendix A

to account for the induced downwash field due to vorticity shed at the tunnel wall intersection with the model, and is a function of lift coefficient (i.e., trailing edge suction peak). As can be seen, the corrections are significant. At zero blowing,  $\alpha_{eff} = \alpha_c$  since no trailing edge peak is present. Using the effective incidence, Figures 25 and 26 summarize the data of Figure 23 in terms of  $C_L$  obtained at a higher value of  $C_\mu$  over the  $\alpha_{eff}$  range, and  $C_{L_{max}}$  as a function of  $C_\mu$ . Figure 27 plots  $C_{L_{max}}$  versus effective stall angle for the five configurations at various values of  $C_\mu$ .

#### Slot Height Variation

The momentum coefficient is a function of the parameters  $P_d/P_\infty$ ,  $T_d$ ,  $A_j$ ,  $S$  and  $q$  and for a two-dimensional airfoil may be defined as

$$C_\mu = \frac{\dot{m}V_j}{qc} = \frac{\rho_j h V_j^2}{\frac{1}{2} \rho V_\infty^2 c} = 2 \frac{\rho_j}{\rho} \frac{h}{c} \left( \frac{V_j}{V_\infty} \right)^2$$

Figure 28 shows experimental variation in the momentum coefficient for configuration 241 at 9° geometric incidence. Although theoretical  $C_\mu$  is not a function of incidence (see Appendix A), when mass flow is measured experimentally the significant pressure ratio is total pressure divided by local static pressure at the slot exit, which will of course vary with  $q$ , airfoil configuration, lift coefficient and incidence.

Figures 29 and 30 show the effects of slot height variations on lift for CCW241 and CCW244. Both figures show that for a constant value of  $C_\mu$ , greater lift results from a smaller slot. This is of course due to the fact that the reduced slot area is compensated for by increased jet velocity to maintain a constant  $C_\mu$ . Increased  $V_j$  implies increased kinetic energy, jet turning and lift augmentation. However, these figures show that there are crossovers where reduced slot height corresponds to reduced  $C_L$  at constant  $C_\mu$ . It will be noted that these values of  $h/c$  approach the lower limit of .0005 suggested in the Design Considerations section, where internal nozzle boundary layer thickness

begins to equal the slot height. Figure 29 also indicates lines of constant pressure ratio for the two larger slot heights; these lines represent constant jet velocity. In this case, an increase in slot height produces increased lift due to the resulting higher mass flow and  $C_u$ . The final decision concerning use of reduced or increased slot height will depend on the method of air supply: a fixed pressure ratio system would suggest increase in slot height, whereas a constant  $C_u$  system might suggest reduced slot height for improved performance (although the required power, proportional to  $V_j^3$ , would be an important consideration).

In contrast to the detrimental effects of too small a slot height, Figure 30 also confirms the problem of partial jet detachment with large slots (see Reference 11 for additional details). Under certain conditions of high pressure ratio, large slot height, and reduced trailing edge radius, the Coanda mechanism begins to break down, and the jet turning is considerably reduced, if not totally eliminated, by jet detachment from the surface. The higher  $C_u$  data points for  $h = .054''$  show significant scatter and indications of jet ineffectiveness; pulsating turbulence from the vicinity of the model confirmed this. The parameter  $h/c'$  is at the upper limit suggested in the Design Considerations. Thus, both upper and lower limits on slot height are confirmed, but the associated values of  $C_u$  which should not be exceeded at those parameters have not been established for all configurations and incidences.

#### Reynolds Number Effects

Use of the larger chord model allowed Reynolds number variation up to  $2.4 \times 10^6$ , corresponding to  $q = 50$  psf. The effects on lift are given in Figure 31 for CCW245 at  $\alpha_g = 0^\circ$ . Again, low  $C_u$  produces relatively little  $C_L$  variation with  $R_e$ , but at higher  $C_u$  a rather noticeable increase is present. The effects of  $R_e$  alone cannot be distinguished from the effects of increasing the pressure ratio (jet velocity) in order to maintain constant  $C_u$  at increased  $q$ . It is suggested that lines of constant



$C_{\mu} M_j$ ,  $C_{\mu} P_d/P_{\infty}$  or  $C_{\mu} (1 - \frac{V_1}{V_{\infty}})$  might separate the Reynolds number and jet velocity effects.

### Drag

Results of variations in section drag coefficient with blowing in Figure 32 are very similar to those of Figure 18 for the small chord airfoil: (1) nose droop produces high  $C_d$  at no blowing and low incidence, (2) application of blowing brings on rapid drag reductions at all incidences, and (3) viscous mixing on the aft lower surface or leading edge separation result in rapid drag increases with increased  $C_{\mu}$ . A number of the data points found in Figure 20 have had to be eliminated from the drag plots due to movement of the momentum deficit region of the wake off the lower limits of the rake. In addition, data scatter at higher  $C_{\mu}$  is attributable to more sparsely located total head probes near this lower limit of the rake. The absence of drag data for CCW242 at higher  $C_{\mu}$  is due to large regions of turbulence behind the 15% chord flap perpendicular to the flow. (This large turbulent wake could produce serious problems when applied to a finite wing aircraft if the wake should fall on the horizontal tail surface.) With the above limitations in mind, a comparison of the drag data for the five configurations at  $C_{l_{max}}$  points of Figure 26 is made in Figure 33. With the exception of the 90° flap case, all configurations show a rapid decrease in  $C_d$  with  $C_{\mu}$ , followed by either a drag rise or a change in slope which indicates the beginning of a drag rise. In contrast, CCW242 shows constantly decreasing drag with no apparent change in slope indicative of a drag rise; this is due to the fact that  $C_{l_{max}}$  for this airfoil always occurs at relatively low incidence, and to the fact that the jet can turn no further than 90° due to the existence of the flap surface. A characteristic jet flap mode with a higher degree of thrust recovery is evident.

### Pitching Moment

The variation of quarter-chord (25 percent undeflected chord) pitching moment with  $C_{\mu}$  at constant  $\alpha_c$  is presented for CCW241 in Figure 34. As is characteristic of almost all high lift schemes, the

suction peak produced by the trailing edge device (be it blowing or a flap) generated additional nose-down pitching moment. There appears to be little variation with incidence (except above  $12^\circ$ ), indicating that at constant  $C_\mu$  the trailing edge suction peak is dominant over the variation in leading edge peak due to incidence. Figure 35 presents  $C_l$  vs  $C_{m25}$  along lines of constant incidence and  $C_\mu$  for all five configurations. The larger nose-down moments associated with the  $90^\circ$  flap case are due to the near vertical component of jet thrust acting parallel to the flap surface with the high thrust recovery characteristic of jet flaps. This thrust contribution to moment is considerably reduced for all the bluff trailing edge configurations due to jet mixing. However, the extended trailing edge configuration (CCW243) does exhibit somewhat higher moments than the other bluff versions in that its jet suction peak is located near the undeflected airfoil trailing edge, roughly .15c further aft. Figure 36 points out these relative comparisons by plotting the pitching moment corresponding to  $C_{l_{max}}$  at various  $C_\mu$ . In addition to the above explanation, the greater nose-down moments of the  $90^\circ$  flap also occur because  $C_{l_{max}}$  for this airfoil is always at low incidence, where the more favorable aft pressure gradients serve to create even higher jet suction peaks over the Coanda surface, and where the counter-acting leading edge suction peaks are less.

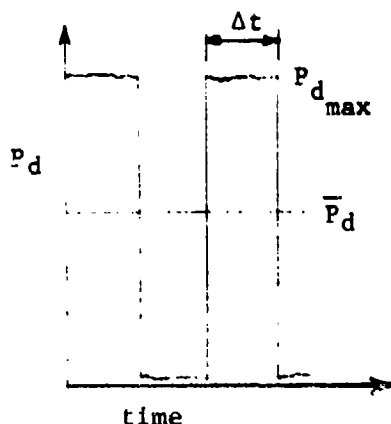
#### PULSED BLOWING INVESTIGATION

Investigations conducted with pulsed unsteady blowing over a blown flap (Reference 12) and on a cambered CC ellipse (Reference 13) indicated that definite additional lift augmentation above the steady-state value could be obtained by this technique. For equal values of effective momentum coefficient (time-averaged  $C_\mu$  in the unsteady case), the pulsed blowing produced higher trailing edge suction peaks and lift augmentation because of the instantaneous higher values of duct pressure and jet velocity which produced greater flow entrainment and jet turning. This of course allows a desired lift coefficient to be produced at reduced mass flow rates. The results of Reference 12 indicate this reduction in required  $\dot{m}$  to be as much as 50 percent. Both investigations identified optimum pulsing frequencies, above or below which lift generation was less.

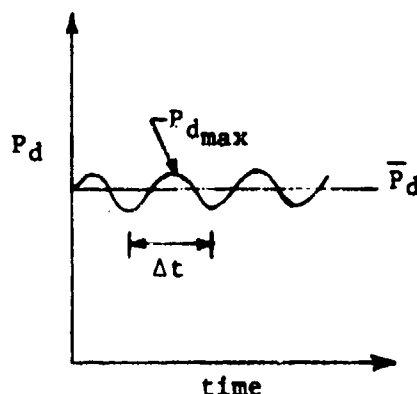
A similar investigation was conducted on configuration CCW244, which has the reduced trailing edge radius ( $r/c' = .021$ ), to determine if similar reductions in required mass flow could be realized for a configuration of the CCW. Appendix A describes the test setup and data reduction techniques employed; the major difference from the previous tests was the insertion of a rotating butterfly valve between the venturimeter used to measure system mass flow and the plenum of the model. Figure 37 plots averaged lift and momentum coefficients as functions of pulsing rate. The lift is averaged automatically by the damping of the static pressure tubing, while mass flow is averaged by recording mean readings of the venturimeter pressures. Duct pressure and jet velocity are obtained by identifying mean values of  $P_d$  from oscillograph traces of the model plenum pressure transducer output. There is no apparent trend in lift augmentation as a function of pulsing rate from 0 to 69 cycles per second in Figure 37, with the exception that all unsteady data appears to be less effective than the steady case ( $\omega = 0$  cps). It was suggested by the lack of any smooth trend with variation of  $\omega$  that some error was being introduced by the venturimeter. Figure 38 plots mean mass flow recorded from this flow meter as a function of line pressure upstream of the pulsing valve. As data from Reference 12 confirms, a given mass flow at the slot should always require higher upstream line pressure than the steady case, for which the cyclic valve is producing no pressure loss. However, as Figure 38 shows, mean mass flow for the 20 and 40 cps cases is produced at lower line pressure than the steady case. It was concluded that the venturimeter was being adversely affected by the pressure fluctuations feeding back upstream from the butterfly valve, and its measurements were unreliable.

As an alternative, mean duct pressure  $\bar{P}_d$  read from the oscillograph traces was used with a previous calibration to determine slot height deflection under pressure, and the resulting slot areas and pressure ratios were substituted into the isentropic equations in Appendix A to yield mean mass flow, jet velocity and  $C_{\mu}$ . The results in Figure 39 indicate that for the cases investigated, pulsed blowing has little discernable lift augmenting effect. This may be due to two aspects of

the test setup. The pulsing device of Reference 12 produced a square wave variation of duct pressure in which the minimum was almost zero-- this produced a maximum value almost twice the mean, and thus jet turning and augmentation that were considerably higher than for the mean  $C_D$ . The pulsating valve used for the present investigation produced a sinusoidal pressure variation in which the maximum pressure was never more than 15 percent higher than the mean or comparable steady state pressure. Thus the augmentation was minimal. The comparison is sketched below.



Reference 12



Present Investigation

Secondly, the trailing edge configuration was probably not ideal for this investigation. The small radius ( $r = .4375''$ ) and larger slot produced  $h/r = 0.0617$ , which under conditions of higher jet velocity could produce detrimental effects. Furthermore, as Reference 12 indicates, the vorticity produced by jet pulsing which is responsible for the additional augmentation begins to decay when the time intervals between the pulsing become greater than approximately  $50 r/U_{\max}$ , where  $U_{\max}$  is the maximum value in the wall jet velocity profile. Thus small radii are detrimental to unsteady augmentation under higher jet velocities or greater pressure ratios. Therefore, considering this along with the ineffective pulsing valve used, the present investigation did not verify the positive effects of pulsed blowing determined in References 12 and 13, but did suggest more appropriate model and valve configurations for any further experiments.

## SPOILER INVESTIGATION

The application of CCW airfoil sections promises to lower the approach and take-off speeds of fixed wing aircraft to the point where conventional aerodynamic control devices may become ineffective. Reference 2 data shows that ailerons on a partially blown wing can be exposed to severe spanwise flow or outboard separation, and in addition can generate adverse yawing characteristics. It was surmised that spoilers, located upstream of the blown trailing edge, would be a far more effective roll control and would not produce the adverse yaw problem. The possibility of a spoiler being too effective when deflected into the boundary layer just upstream of the tangential jet led to a preliminary two-dimensional investigation. The model, a 20.6 percent thick ellipse with 3.6 percent circular arc camber and  $r/c = 0.045$  had previously been installed in the 3- x 8-foot inserts, and was felt to be characteristic of the trailing edge region of a CCW profile even though it was a rotor blade section. Figure 5 depicts the model and the two spoiler configurations employed. Both were made from angle iron to provide rigidity over the 36-inch span, and were located so as to pivot about a point on the upper surface at  $0.70c$ . The spoiler length  $c_s$  was  $0.0982c$ , and deflection relative to the airfoil chord was from  $-9^\circ$  (flush to the surface) to  $+51^\circ$ . The slotted version of the full spoiler was constructed by removing half the spoiler length nearest to the airfoil, so that part of the airfoil boundary layer flow could penetrate through to the jet slot. All tests were run at zero airfoil incidence at  $q = 20$  psf ( $Re = 0.66 \times 10^6$ ). Wall blowing to prevent three-dimensionality was not employed. Data are corrected for tunnel blockage and boundary constraints, but not for induced incidences.

Figure 40 presents lift as a function of blowing for various spoiler deflections and types, and for the clean airfoil ( $\delta_s = -9^\circ$ ). The effect on  $C_L$  of deflection of the full spoiler is quite severe; supercirculation is heavily restricted and the airfoil behaves quite like a jet flap, with lift almost linearly proportional to blowing. Even with the small spoiler deflection of zero degrees (a perpendicular aft-facing step of only 3 percent chord), lift at  $C_{\mu} = 0.16$  is reduced to 28 percent of the clean

airfoil value. The slotted spoiler shows some improvement: lift returns to the more conventional form where  $C_L = f(\sqrt{C_D})$  and supercirculation is partly restored. Figure 41 plots lift loss ( $\Delta C_L = C_L - C_{L_{clean}}$ ) as a function of spoiler deflection and  $C_D$ . The full spoiler possesses the undesirable trait that lift loss is not linearly proportional to spoiler deflection; the majority of reduction occurs between  $-9^\circ$  and  $0^\circ$ . The slotted spoiler is more linear and should have more desirable control characteristics.

Figure 42 shows that at an increased blowing rate, the separated flow behind the full spoiler at  $\delta_s = 0^\circ$  can be made to reattach due to increased flow entrainment at higher  $C_D$ . The effect of Reynolds number is seen to be minimal for this case, at least below the reattachment point, but there appears to be some Reynolds number effect on the clean airfoil.

The increase in drag due to spoiler deflection is evident in Figure 43; a smaller increase in drag occurs when using the slotted spoiler. Similar trends in pitching moment are seen in Figure 44; nose-down values are greatly reduced by spoiler deflection. Both of these trends may provide effective control when applied to fixed wing operation, although the non-linearity with  $\delta_s$  may present a control system design problem. Furthermore, it appears that the slotted spoiler at relatively low deflection should provide a more satisfactory control system for the CCW. Reduced lateral span of the spoiler might reduce the roll sensitivity to deflection, but this parameter and deflection schedules will have to be determined relative to a specific three-dimensional configuration.

#### CONCLUSIONS

A series of subsonic two-dimensional investigations conducted on a number of configurations of Circulation Control Wing airfoil profiles has confirmed the ability of thin sections employing the concept to generate high lift at relatively low values of momentum coefficient and incidence. A data base has been established for use in predicting the aerodynamic characteristics of aircraft with CC trailing edges, and the effects of variation of a number of aerodynamic and geometric parameters

on airfoil performance have been identified. The experimental data obtained from the four investigations yielded the following conclusions:

NACA 66-210/CCW Airfoil (tested over a range of  $\alpha$ ,  $C_\mu$ ,  $\delta_{LE}$ , and  $Re$ )

- A 0.15c leading edge droop of  $43.6^\circ$  and  $C_\mu = 0.24$  produced a section  $C_L = 5.5$  and satisfactory airfoil operation at higher positive incidence (uncharacteristic of CC rotor blade sections). Reduced droop angle resulted in leading edge separation, reduced jet turning, strong breaks in the  $C_L$  vs  $C_\mu$  curves, rapid drag rise at onset of separation, and failure of the section to operate effectively at positive incidence. Similar results were observed for Krüger leading edge flaps.
- Effects of Reynolds number on lift were minimal with no blowing, but produced positive lift increments with increased  $Re$  at constant  $C_\mu$ .
- For attached leading edge flow, increased  $C_\mu$  initially reduced drag but eventually caused a rapid drag increase as lower surface viscous mixing occurred. Separated flow at the leading edge caused immediate drag increase.
- Pitching moment rapidly became more negative with blowing, and took on the largest negative values at reduced incidence and greatest jet effectiveness.

NACA 64A-212/CCW Airfoil (tested over a range of  $\alpha$ ,  $C_\mu$ ,  $\delta_{LE}$ ,  $h$ ,  $Re$  and trailing edge configuration)

- The 2-D section representing the reduced chord T-2C/CCW airfoil yielded  $C_L = 5.95$  at  $C_\mu = 0.20$  and  $\alpha_c = +9^\circ$ ; this was extrapolated to  $C_L = 6.30$  for the extended trailing edge configuration at the same blowing and slightly lower incidence.
- The greatest net lift was generated by the  $90^\circ$  flap configuration due to its full flap chord and high effective camber, but it displayed a number of disadvantages subtracting from its suitability. These include very large nose-down pitching moment, large turbulent wake, low or negative stall angles and negative lift curve slope at most positive incidences.

- A reduction of 50% in the trailing edge radius of the shortened chord airfoil produced comparable or better lift performance due to very high jet effectiveness. Its performance was slightly reduced compared to the larger radius at higher incidence due to its slightly further aft slot location in terms of effective chord.
- Drag, pitching moment, and Reynolds number trends were similar to those of the 66-210/CCW airfoil, with the exception of the 90° flap discussed above.
- Slot height increase can have differing effects on lift augmentation, depending on the mode of operation of the blowing system. Increased  $h$  yielded reduced  $C_L$  for constant values of  $C_{\mu}$  due to reduced jet kinetic energy, but increased  $C_L$  resulted if the pressure ratio was retained constant and  $h$  increased. Suggested upper and lower limits on slot height were confirmed, beyond which adverse effects on lift augmentation occurred.

#### Pulsed Blowing Investigation (variation in $C_{\mu}$ and $\omega$ )

- Results showed that no benefits were gained from unsteady blowing as performed. This was due to the poor response pattern of the valve and a small trailing edge radius on the airfoil.
- A valve capable of a square wave variation of  $P_d$  with time (resulting in much higher  $P_{d_{max}}$  for a given mean duct pressure) and a larger trailing edge radius appear necessary to realize any lift augmentation due to pulsed blowing.

#### Spoiler Investigations (variation in $C_{\mu}$ , $\delta_s$ and spoiler type)

- The full spoiler showed very large reductions in  $C_L$ ,  $C_d$  and nose-down pitching moment as compared to the clean airfoil. All reductions appeared to be non-linear with spoiler deflection.
- The slotted spoiler showed reductions in lift, drag, and pitching moment not quite as large as those for the full spoiler, and the variations appeared to be much more linear with deflection.



## RECOMMENDATIONS

The following recommendations are suggested by the present investigations and by the listed conclusions:

- Whereas leading edge droop appeared to control leading edge separation, it was detrimental at lower incidence and appeared to still allow some undesirable boundary layer development at high incidence and lift. A more effective leading edge device, such as a slat or leading edge tangential blowing, should be substituted for droop in a future experiment.
- The significant performance variations with trailing edge configuration suggest that other geometries might prove more optimum. The deviation from circular into cycloidal or other geometrically similar shapes is suggested. A parametric study of trailing edge variation needs to be undertaken, and the development of an analytic method able to predict the viscous characteristics of this type of airfoil is strongly suggested.
- To further investigate the possible advantages of pulsed blowing, an additional 2-D investigation is recommended with a larger trailing edge radius and an alternate pulsing mechanism which produces larger  $P_{d_{max}}$  relative to the mean duct pressure.
- Additional spoiler investigations are suggested where small deflections in the range of -9 to 0 degrees for the full spoiler, and -9 to 25.5 degrees for the slotted spoiler are evaluated for possible linearity in those ranges. Also, a spoiler on a 3-D configuration should be investigated in which variations in spanwise length and lateral location of the spoiler are conducted.

## ACKNOWLEDGEMENT

The author would like to express his appreciation to the following individuals for their assistance in conducting the wind tunnel investigations reported in this study:

- Mr. Phil Dodd for assistance in tunnel operation and data recording during the 66-210/CCW investigations in February through May, 1972, and Mr. Jonah Ottensoser for design, installation, and testing of the Krüger leading edge configuration of this model in the spring of 1971.
- Messrs. Jonah Ottensoser, Jerome Winkler, and Dulany Davidson for assistance in model installation, tunnel operation and data collection during the 64A-212/CCW investigation in May and June of 1974.
- Mr. Fred Krause for similar assistance during the pulsed blowing investigation in August and September 1974.
- Mr. Rod Hemmerly for similar assistance in the spoiler tests in March 1975.

## REFERENCES

1. Stone, M. B. and R. J. Englar, "Circulation Control - A Bibliography of NSRDC Research", July 1973, Naval Ship Research and Development Center Report 4108.
2. Englar, Robert J., "Subsonic Wind Tunnel Investigation of the High Lift Capability of a Circulation Control Wing on a 1/5-Scale T-2C Aircraft Model", May 1973, Naval Ship Research and Development Center Report ASER 299.
3. Englar, Robert J., "Investigation into and Application of the High Velocity Circulation Control Wall Jet for High Lift and Drag Generation on STOL Aircraft", AIAA Paper No. 74-502 presented at AIAA 7th Plasma and Fluid Dynamics Conference, Palo Alto, Calif., June 1974.
4. Englar, R. J., "Two-Dimensional Subsonic Wind Tunnel Tests of Two 15-Percent Thick Circulation Control Airfoils", Aug 1971, Naval Ship Research and Development Center Report ASER 211. (AD 900 210L)
5. Englar, R. J., "Two-Dimensional Subsonic Wind Tunnel Tests of a Cambered 30-Percent Thick Circulation Control Airfoil," May 1972, Naval Ship Research and Development Center Report ASER 201. (AD 913-411L)
6. Englar, R. J. and R. M. Williams, "Design of a Circulation Control Stern Plane for Submarine Applications", Mar 1971, Naval Ship Research and Development Center Report ASER 200. (AD 901-198)
7. Englar, R. J. and R. M. Williams, "Test Techniques for High Lift Two-Dimensional Airfoils with Boundary Layer and Circulation Control for Application to Rotary Wing Aircraft", Canadian Aeronautics and Space Journal, Vol. 19, No. 3, pp 93-102, Mar 1973.
8. Abbott, Ira H. and Albert E. Von Doenhoff, "Theory of Wing Sections", N.Y., Dover Publications, Inc., 1959.

9. Schlichting, Hermann, "Boundary Layer Theory", 6th ed., N.Y., McGraw-Hill, 1968.
10. Kind, R. J., "A Proposed Method of Circulation Control", Cambridge, Eng., June 1967 (Cambridge Univ. Ph.D. Thesis).
11. Englar, R. J., "Experimental Investigation of the High Velocity Coanda Wall Jet Applied to Bluff Trailing Edge Circulation Control Airfoils", June 1973, Naval Ship Research and Development Center Report ASED 308. (M. S. Thesis, Dept. of Aerospace Engineering, University of Maryland, 1973).
12. Williams, J. R., et.al., "Analysis of a Pulsing Wall Jet", Oct 1972, Columbus Aircraft Division, North American Rockwell Report NR72H-325.
13. Walters, R. E., et. al., "Circulation Control by Steady and Pulsed Blowing for a Cambered Elliptical Airfoil," July 1972, West Virginia University Department of Aerospace Engineering TR-32.
14. Englar, R. J. and J. Ottensmeyer, "Calibration of Some Subsonic Wind Tunnel Inserts for Two-Dimensional Airfoil Experiments", September, 1972, Naval Ship Research and Development Center Report ASED 275.
15. Pope, Alan, "Wind-Tunnel Testing", 2nd ed. N. Y., John Wiley & Sons, Inc., 1964.

## APPENDIX A

### MODELS, EXPERIMENTAL APPARATUS, AND TECHNIQUE

#### MODELS

Both CCW modifications of conventional airfoil sections were based on the geometric parameters of Tables I and II and are shown in Figures 3 and 4. Coordinates of the airfoils ahead of the slot are identical to the original airfoils with the exception of deflected leading edge devices. Leading edge droop for both airfoils involved rotation of the nose about a lower surface hinge point at 15 percent of the original chord, and filling the resulting gap with a circular arc with center at the hinge point. Slot height was adjustable by means of compression and jack screws; the slot was contoured to be the minimum area of a smoothly converging nozzle. Nominal slot height is the value measured with feeler gage stock with zero plenum pressure. Slot expansion with pressure was measured for each configuration and found to be linear for the 66-210/CCW airfoil, but of no specific trend for the 64A-212/CCW airfoil since the plenum geometry was not always identical for all configurations. On the 66-210/CCW section, the trailing edge was fixed in the fully rotated position of Figure 1 and only the slot height and droop were variable. For the 64A-212/CCW configuration, the trailing edge configurations were interchangeable as shown in Figure 4, and droop and slot height were variable. The CC rotor airfoil used in the spoiler test (Figure 5) was built by Lockheed-California Company under contract for application to a research rotary wing aircraft; for the present tests, only the deflection of the added spoilers was variable. All models had a chordwise distribution of static pressure taps at or near the midspan, and one to three rows of spanwise static taps to measure two-dimensionality from wall to wall. Plenum total pressure and temperature were recorded by a total pressure probe and thermocouple located in the plenum near midspan.

## TEST APPARATUS AND TECHNIQUE

The small chord model 66-210/CCW airfoil was installed in the DTNSRDC 15- x 20-inch subsonic model tunnel, spanning the short dimension of the test section and attached to circular wall mounts which rotated to vary incidence. All pressure data from the airfoil and wake rake was recorded automatically by a 144-port scannivalve system, punched on paper tape, and reduced by XDS-930 digital computer. Mass flow into the model was measured by orifice plate or venturimeter in the supply line. Test technique was identical to that employed in previous tests of elliptic rotor blade airfoils (Reference 1) and presented in detail in Reference 7. One exception was that the strong three-dimensional induced effects produced by interference between wall boundary layer and jet adverse pressure gradient were controlled by tangential blowing from the tunnel vertical sidewalls at stations ahead of the nose and on the upper surface ahead of the jet suction peak. Blowing rates from these jets were set to those values which best restored two-dimensionality to the spanwise pressure taps as displayed on manometer boards.

Both the 64A-212/CCW and the elliptic airfoil were installed on rotatable endplates in the walls of the 3- x 8-foot 2-D inserts installed in the DTNSRDC 8- x 10-foot subsonic South Tunnel. Figure 6, 7, and 8 show this installation, and Reference 14 describes in detail the development, calibration and operation of this facility. Data recording, mass flow measurement, and test technique were similar to the small tunnel investigations, with the exception that only one set of wall blowing slots was used to control two-dimensionality due to limited facility air supply. It was found later that these were not totally effective, and it was necessary to correct the data for induced effects, as discussed below. For the spoiler tests, no wall blowing was employed at all, since only data trends were of interest there.

## DATA REDUCTION AND CORRECTIONS

As mentioned previously, all force and moment data was from integration of model static pressures or deficits in wake momentum distributions. All coefficients have been nondimensionalized by the original

chord which connects undeflected leading and trailing edges (8 inches for 66-210, 24 inches for 64A-212, and 10.6 inches for the cambered ellipse). Incidence is referenced to this chord, and Reynolds number is based on it as well. This allows direct comparison of all airfoil results. It should be noted however, that the pressure distributions for the 66-210/CCW airfoil are plotted in terms of  $x/c'$  to stretch out the longitudinal coordinates. Normal and axial force coefficients from pressure integration (subscript "p") were modified by the jet thrust component and then combined to yield the lift coefficient:

$$C_n = C_{n_p} + C_\mu \sin \delta_j \quad \text{where } C_{n_p} = \int C_p \frac{x}{c} dx$$

$$C_a = C_{a_p} - C_\mu \cos \delta_j \quad \text{where } C_{a_p} = \int C_p \frac{y}{c} dy$$

$$C_d = C_n \cos \alpha_c - C_a \sin \alpha_c$$

where  $\delta_j$  is the angle between the chord and line of jet thrust, and  $\alpha_c$  is the corrected incidence. The drag integration employs the methods of Betz and Jones (Reference 9) to determine the drag coefficient  $C_{d_{rake}}$ , which must then be modified (References 5, 7 and 10) to account for the additional jet momentum in the control volume:

$$C_d = C_{d_{rake}} - \frac{\dot{m} V_\infty}{q c} = C_{d_{rake}} - C_\mu \frac{V_\infty}{V_j}$$

The pitching moment coefficient  $C_{m_{25}}$  is determined from integration of the normal and axial components of static pressure and the jet thrust reaction about the quarter-chord point. The freestream dynamic pressure is corrected for solid blockage as follows:

$$q = q_u (1+2\epsilon)$$

$$\text{where } \epsilon = 0.822 \lambda_2 (t/h_t)^2$$

and  $\lambda_2$  is an airfoil shape factor from Reference 15.

The above coefficients are referenced to this corrected value of dynamic pressure, and corrections for tunnel wall constraint (induced camber) are then applied (where subscript "u" is the uncorrected value as determined above):

$$C_l = C_{l_u} - \frac{\pi^2}{48} \left( \frac{c'}{h_t} \right)^2 C_{l_u}$$

$$C_{m_{25}} = C_{m_{25u}} + \frac{\pi^2}{192} \left( \frac{c'}{h_t} \right)^2 C_{l_u}$$

$$\alpha_c = \alpha_g + \frac{57.3\pi}{96} \left( \frac{c'}{h_t} \right)^2 (C_{l_u} + 4C_{m_{25u}})$$

The momentum coefficient was calculated as

$$C_\mu = \frac{\dot{m}V_j}{qS} = \frac{\dot{m}V_j}{qc} \quad (\text{if } \dot{m} \text{ is per unit span})$$

where the total mass flux ( $\dot{m}$ ) was recorded experimentally from the installed flowmeter, and the jet velocity was calculated assuming an isentropic expansion from plenum total conditions to freestream static condition:

$$V_j^2 = 2RT_d \left( \frac{\gamma}{\gamma-1} \right) \left[ 1 - \left( \frac{P_\infty}{P_d} \right)^{\frac{\gamma-1}{\gamma}} \right]$$



For the pulsed blowing cases where it was necessary to calculate the isentropic mass flows, these were determined as follows:

$$\text{choked flow: } \dot{m} = A_j P_d \sqrt{\frac{\gamma}{RT_d}} \left( \frac{2}{\gamma+1} \right)^{\frac{\gamma+1}{2(\gamma-1)}}$$

$$\text{unchoked flow: } \dot{m} = A_j P_d \left\{ \frac{2\gamma}{(\gamma-1)RT_d} \left[ \left( \frac{P_\infty}{P_d} \right)^{2/\gamma} - \left( \frac{P_\infty}{P_d} \right)^{\frac{\gamma+1}{\gamma}} \right] \right\}^{1/2}$$

For the 64A-212/CCW airfoils, one additional set of data corrections was applied. In this case, the tangential tunnel wall blowing did not prove totally effective in eliminating the three-dimensionality and induced effects discussed in the text, and it was evident that the airfoil was operating at an effective incidence less than  $\alpha_c$ . As discussed in References 5, 7, and 10, this effective incidence could be determined by matching potential flow pressure distributions with the experimental distributions at the same effective  $C_L$  over a range of incidence, and determining that incidence at which the theoretical and experimental leading edge stagnation points coincided. This would be the true effective incidence of the experimental data. With increasing  $C_L$ , this incidence becomes considerably less than  $\alpha_c$ . Incidence correction curves similar to Figure 24 were calculated in this manner for each configuration of the 64A-212/CCW airfoil, and the lift curves of Figure 23 were corrected accordingly.

#### PULSED BLOWING APPARATUS

For this investigation, a housing containing a rotating flat disc driven by a variable frequency motor was installed in the air supply line roughly 8 feet downstream of the venturimeter. When this butterfly valve disc was perpendicular to the flow, the entire cross sectional area of the supply line was closed off. However, for frequencies of rotation between 20 and 69 cycles per second, the area was closed off for such a small portion of the period that the pressure downstream in the model plenum never varied more than 15 percent from the mean plenum pressure. As discussed in the text, the sinusoidal plenum pressure variation was

recorded by oscillograph traces and the mean was used to calculate jet velocity. Upstream and differential pressure across the venturimeter were sensed by transducers whose output was displayed on TIC readout units, where the mean was recorded by hand. When these venturimeter readings proved questionable, the isentropic mass flow was calculated using the previous equations and the calibrated variation of slot height with duct pressure as shown below.

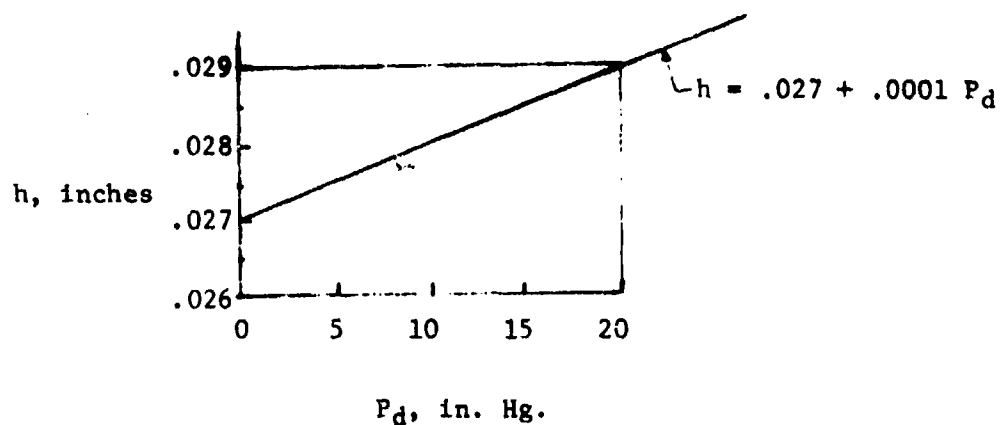


TABLE - I GEOMETRIC PROPERTIES OF NACA 66-210/CCW  
AIRFOIL SECTIONS

Parameters common to all four configurations:

$c' = 7.083''$	$c = 8.000''$
$\delta_f = 180^\circ$	
$r = 0.276''$	
$h = 0.009''$	
$r/c' = 0.03897$	$r/c = 0.0345$
$h/r = 0.0326$	
$h/c' = 0.00127$	$h/c = .00113$
$x_{slot} = 6.819''$	
$x_{slot}/c' = 0.9627$	$x_{slot}/c = 0.8524$
$t = 0.813''$	
$t/c' = 0.1148$	$t/c = 0.0102$
$r_{LE} = 0.0530''$	
$r_{LE}/c' = 0.00748$	$r_{LE}/c = 0.00662$
$x_{droop} = 1.200''$	
$x_{droop}/c' = .1694$	$x_{droop}/c = .1500$

Leading Edge Deflection:

Configuration	$\delta_{LE}$ , deg	$c_{droop}/c$	$c_{droop}/c'$
CCW			
800	0	.8854	1.00000
815	15.3	.8879	1.00282
829	29.0	.8853	0.99989
844	43.6	.8711	0.98385

( $c_{droop}$  is chord from drooped leading edge to rotated trailing edge,  
but is not used in coefficient calculation)

TABLE II - GEOMETRIC PROPERTIES OF NACA 64A-212/CCM AIRFOIL SECTIONS

$c = 24.00"$ ,  $x_{slot} = 20.40"$  ( $= 24.00"$  for CCM 243),  $t/c = 0.120$ ,  $t_{LE}/c = .00994$

Configuration, CCM-	$\delta_{LE}$ , deg	$\delta_f$ , deg	$c'$ , inches	$r$ , inches	$h$ , inches	$r/c'$	$h/r$	$h/c'$	$\frac{x_{slot}}{c}$	$t/c'$	$r/c$	$h/c$	$\frac{x_{slot}}{c}$	$q$ , psf
241 (Rotated flap)	30 ↓	180 ↓	21.272 ↓	0.875 ↓	0.027 0.020 0.014 0.007	.04113 ↓	.03086 .02286 .01600 .00800	.00127 .00094 .0 .00029	.9590 ↓	.1354 ↓	.03646 ↓	.00113 .00083 .00058 .00029	.8500 ↓	10, 20, 30, 40, 50 30 30 30
242 (90° Flap)	30	90	21.272	0.875	0.027	.04113	.03086	.00127	.9590	.1354	.03646	.00113	.8500	30
243 (Extended T.E.)	30	180	24.875	0.875	0.027	.03318	.03086	.00109	.9648	.1158	.03646	.00113	1.0000	30
244 (Reduced T.E.)	30 ↓	180 ↓	20.835 ↓	0.4375 ↓	0.027 0.014 0.054	.02100 ↓	.06171 .03200 .12343	.00130 .00067 .00259	.9791 ↓	.1382 ↓	.01823 ↓	.00113 .00058 .00225	.8500 ↓	30 ↓
245 ( $\delta_{LE} = 0$ )	0	180	21.272	0.875	0.027	.04113	.03086	.00127	.9590	.1354	.03646	.00113	.8500	10, 20, 30, 40, 50

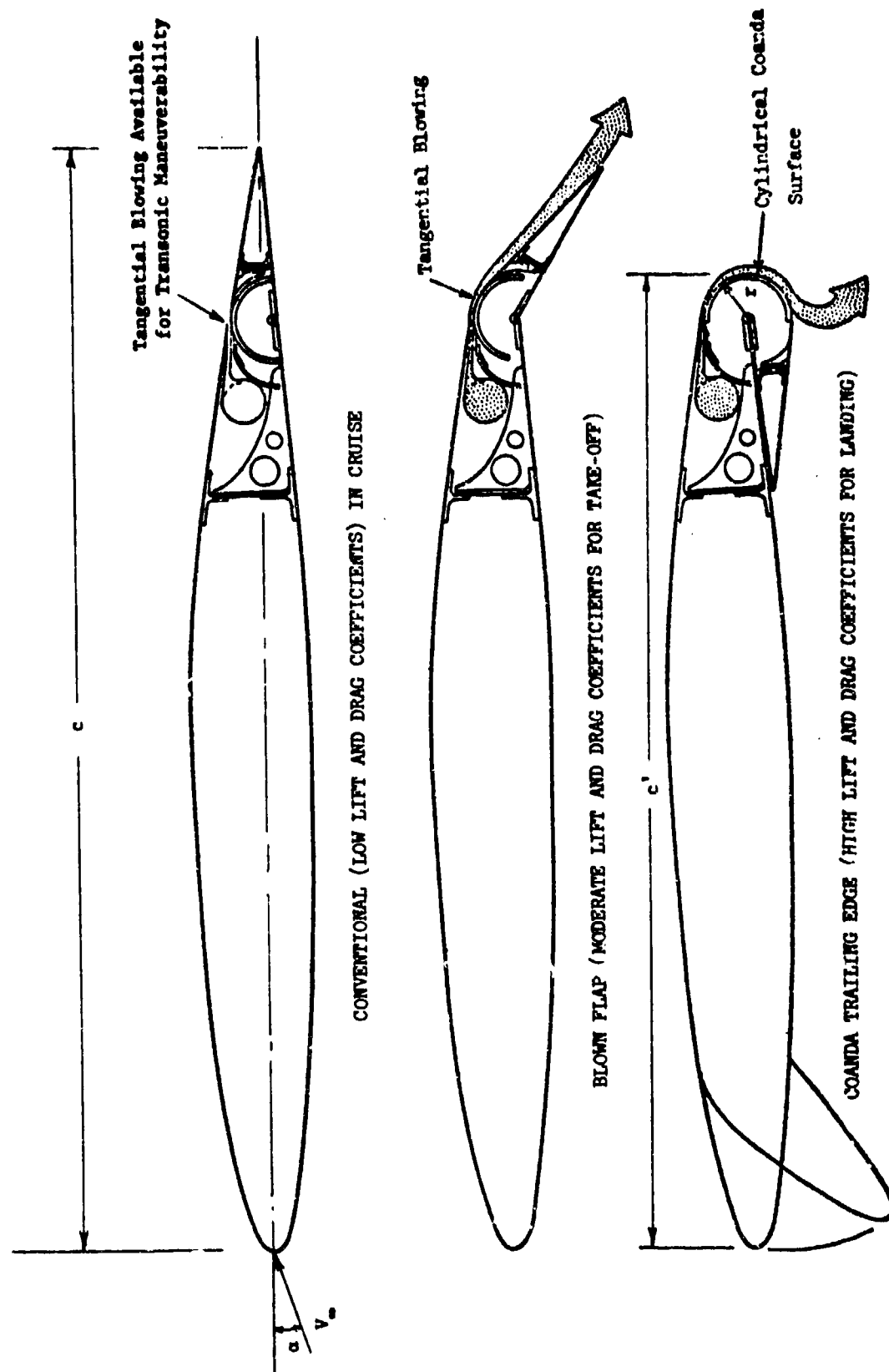
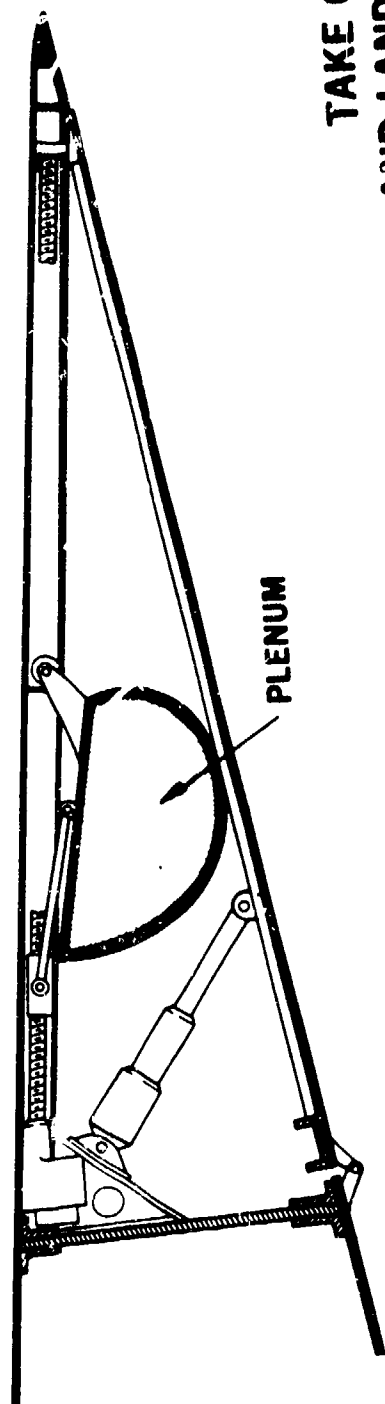


Figure 1 Circulation Control Wing Modes of Operation, Rotating Short Chord Flap Configuration

CRUISE

TAKE OFF  
AND LANDING



PLENUM

PLENUM

COANDA  
SURFACE

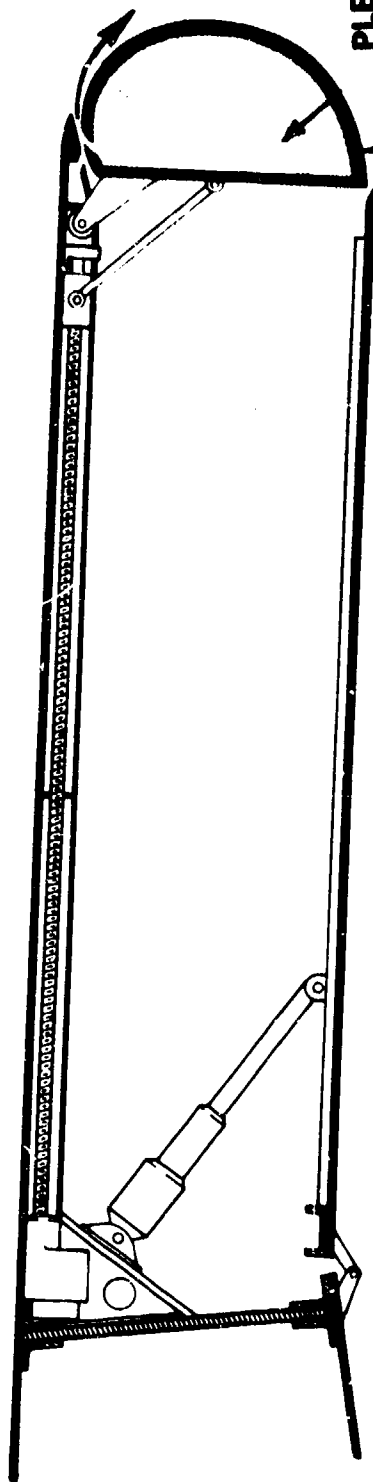


Figure 2 - Extended Trailing Edge Configuration



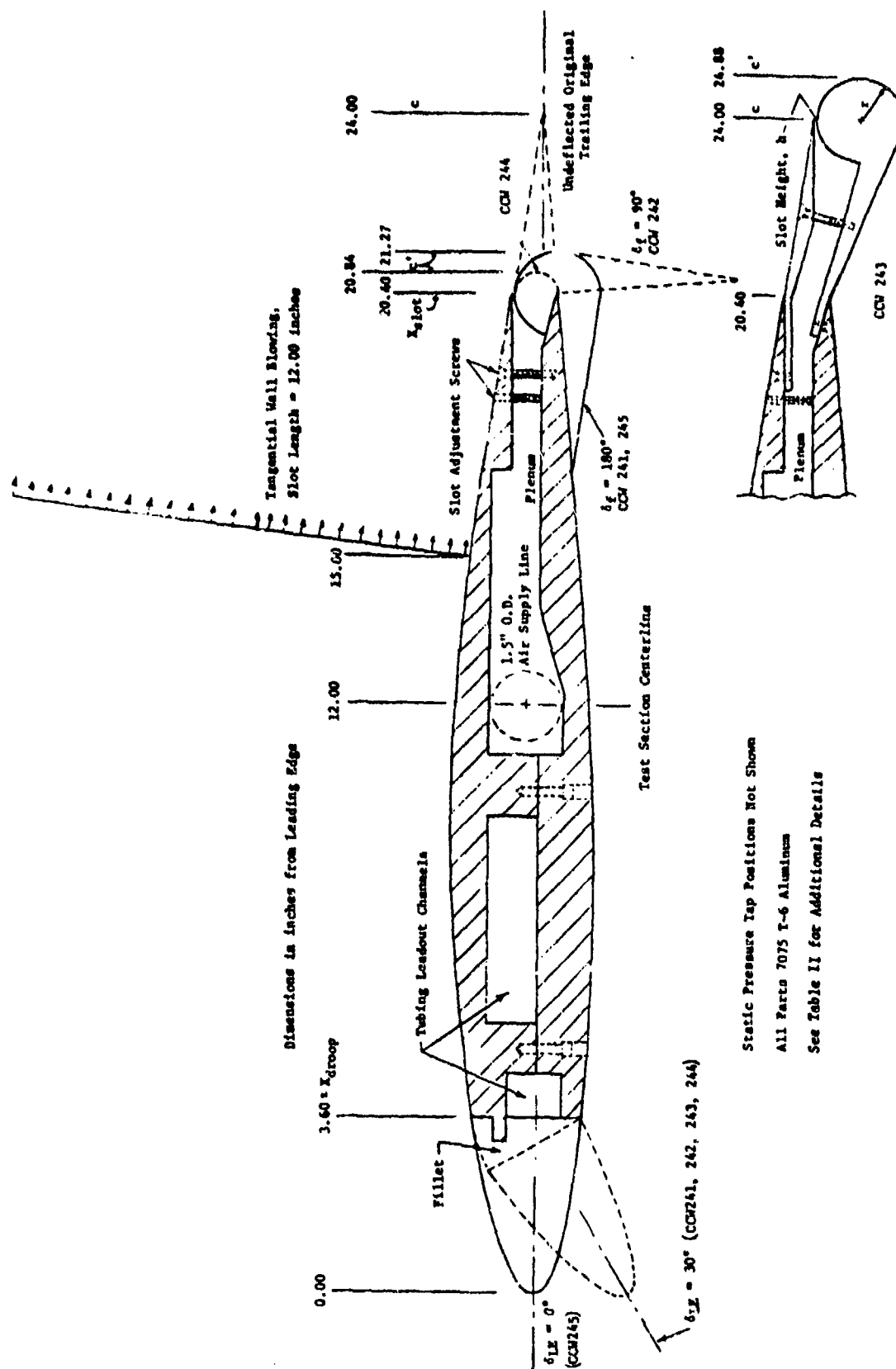


Figure 4 - Model Geometry, NACA 64A-212/CCW Airfoil



$c = 10.18$   
 $\tau = .458$   
 $h = .005$   
 $t/c = .206$   
 $\delta/c = .036$   
 $\tau/c = .045$   
 $h/c = .00049$   
 $h/\tau = .0109$   
 $x_r = 7.123$   
 $x_r/c = .700$   
 $x_{slot} = 9.90$   
 $x_{slot}/c = .9725$   
 $C_s = 1.00$   
 $C_{s/c} = .0982$

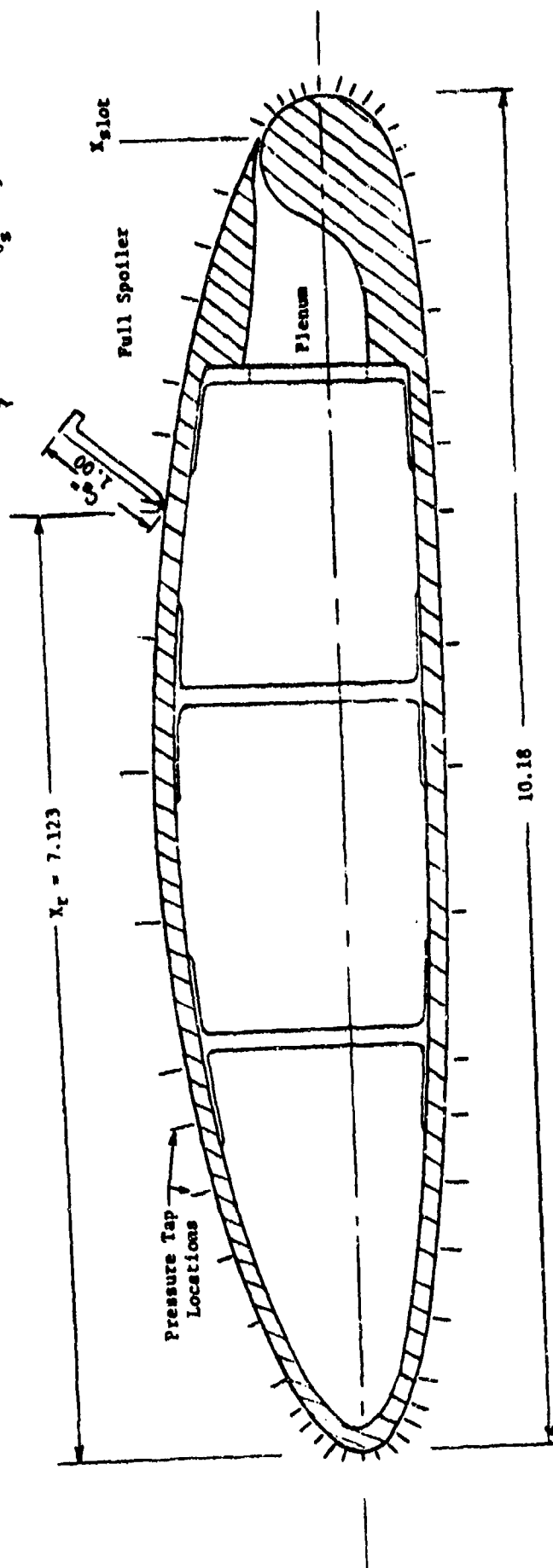
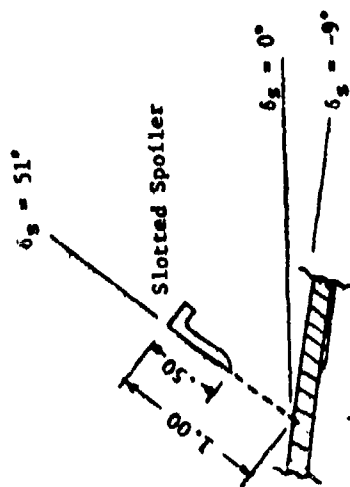


Figure 5 - 2-D Elliptic CC Airfoil with Spoilers Installed  
 (Basic Airfoil Constructed by Lockheed-California Co.)



Figure 6 - 2-D Inserts and MACA 64A-212/CCW Model Installed  
in 8 x 10-Ft South Subsonic Tunnel



Figure 7 - Configuration CCM 243 Installed on Inert Turntables with  
Tangential Wall Blowing

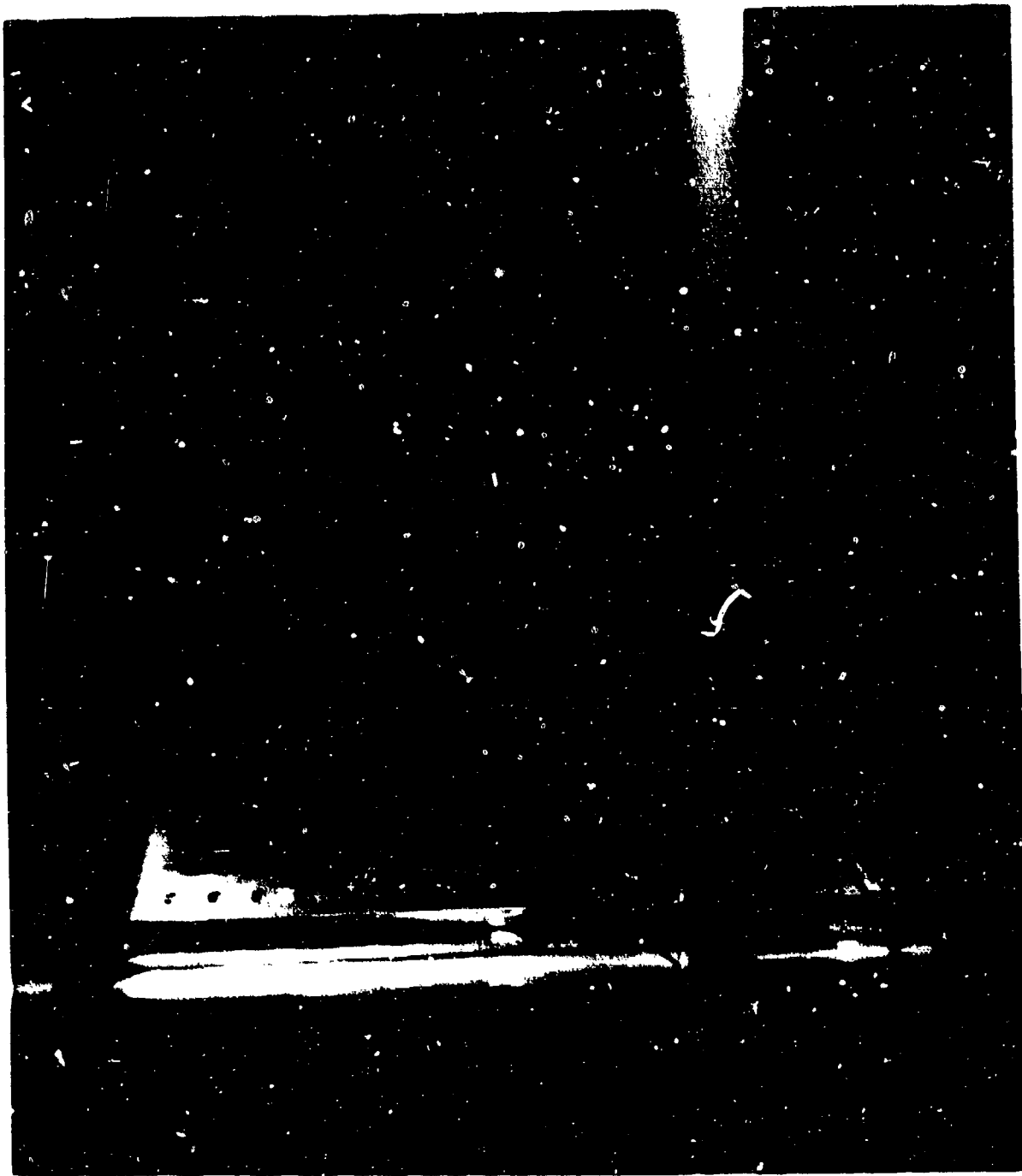


Figure 8 - Aft View Showing Wake Rake, Model, and Tangential Wall Blowing

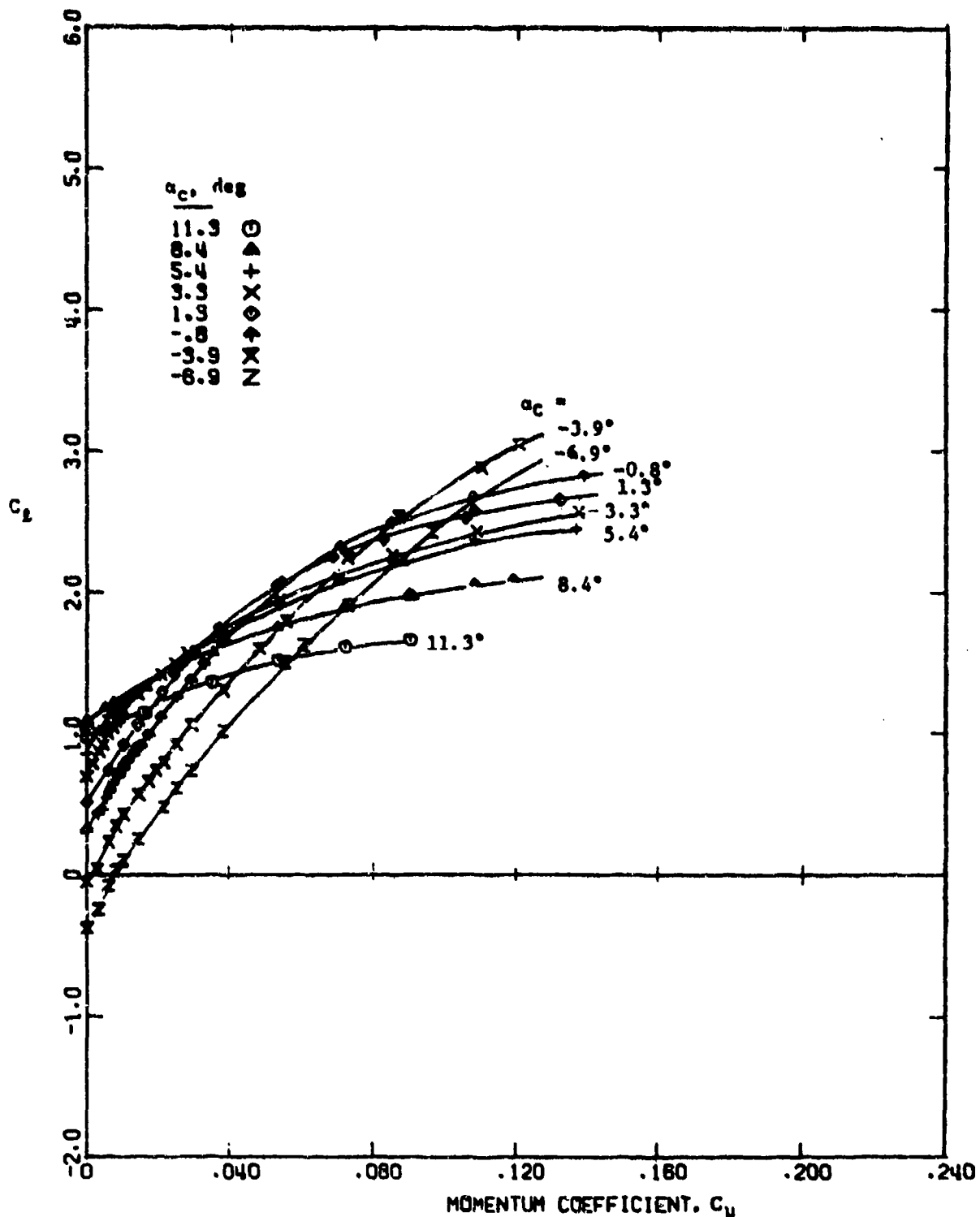


Figure 9 - Lift as a Function of Blowing for the NACA 66-210/CCW  
Airfoils,  $q = 30$  psf,  $R_e \approx 0.64 \times 10^6$ ,  $h = 0.009''$   
(a) CCW 800,  $\delta_{LE} = 0^\circ$

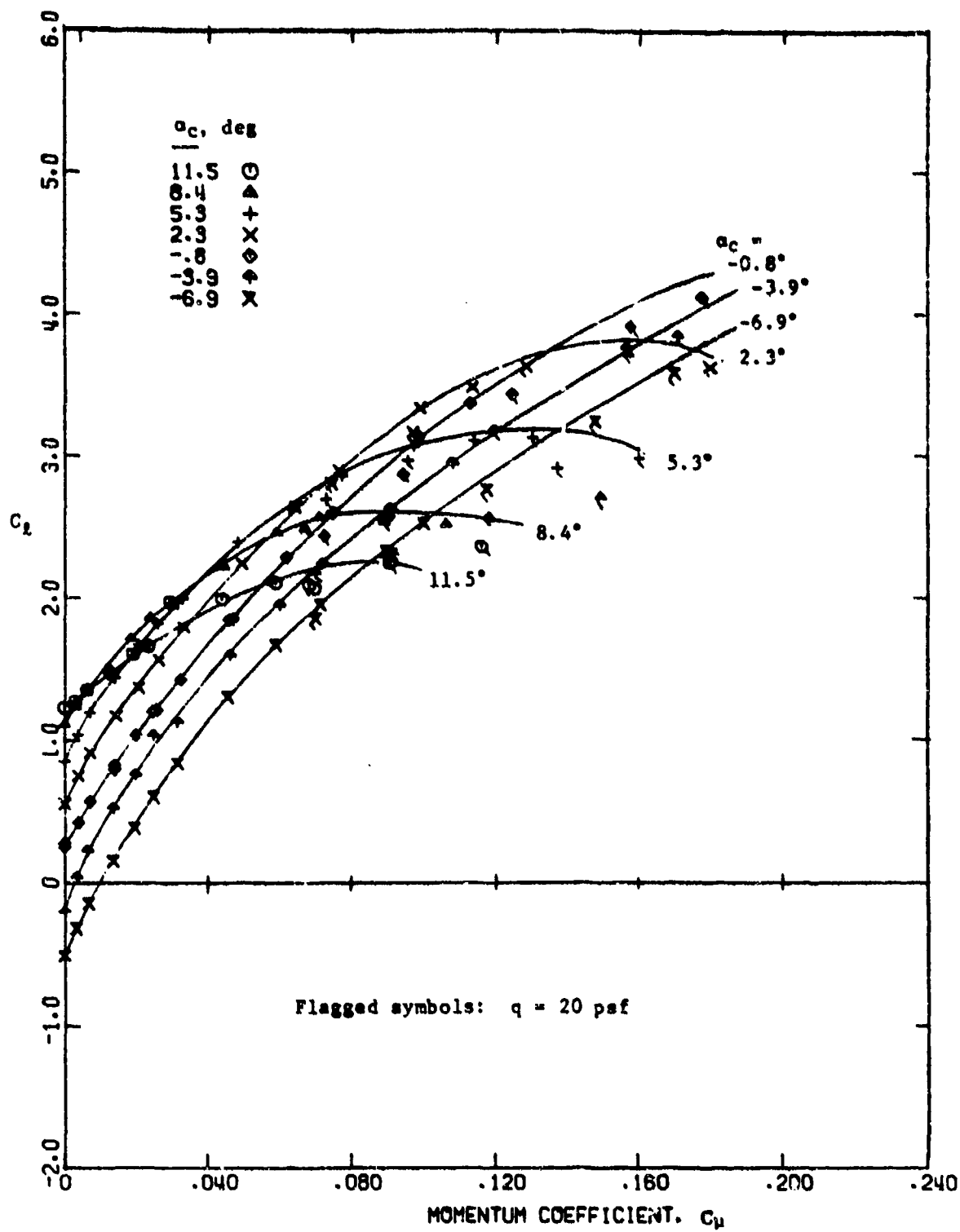


Figure 9 - (Continued)

(b) CCW 215,  $\delta_{LE} = 15.3^\circ$

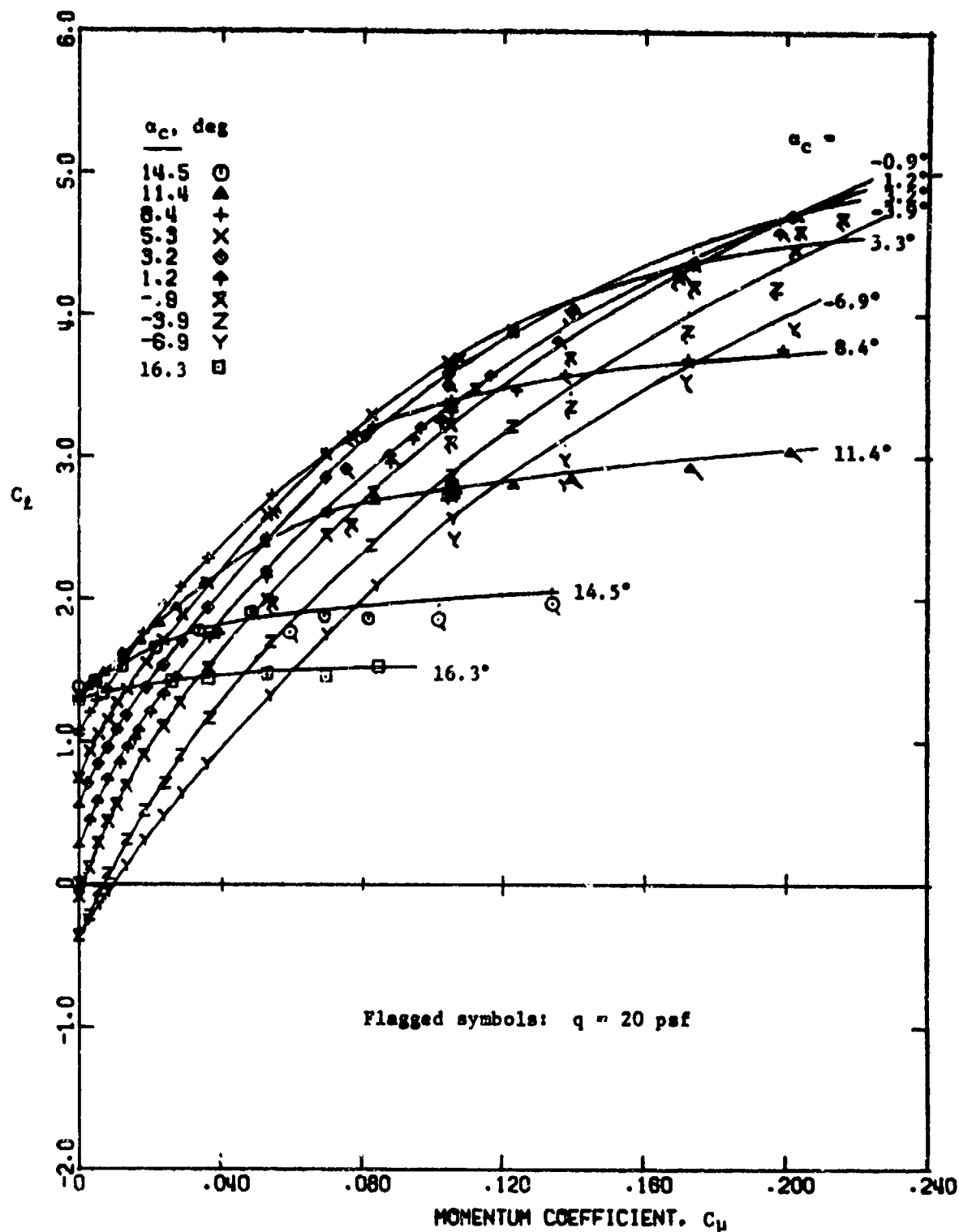


Figure 9 - (Continued)

(c) CCW 829,  $\delta_{LE} = 29^\circ$

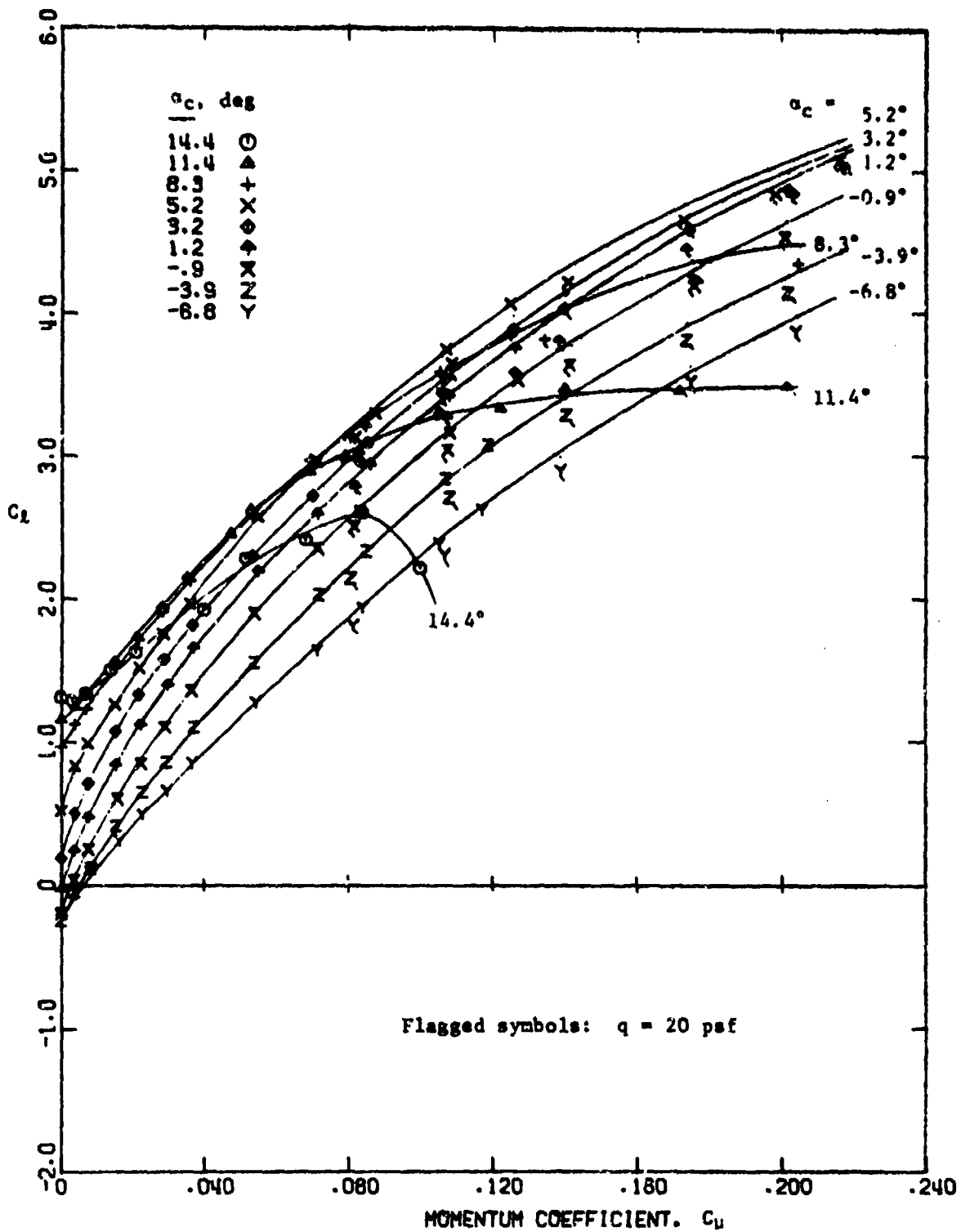


Figure 9 - (Concluded)

(d) CCW 844,  $\delta_{LE} = 43.6^\circ$



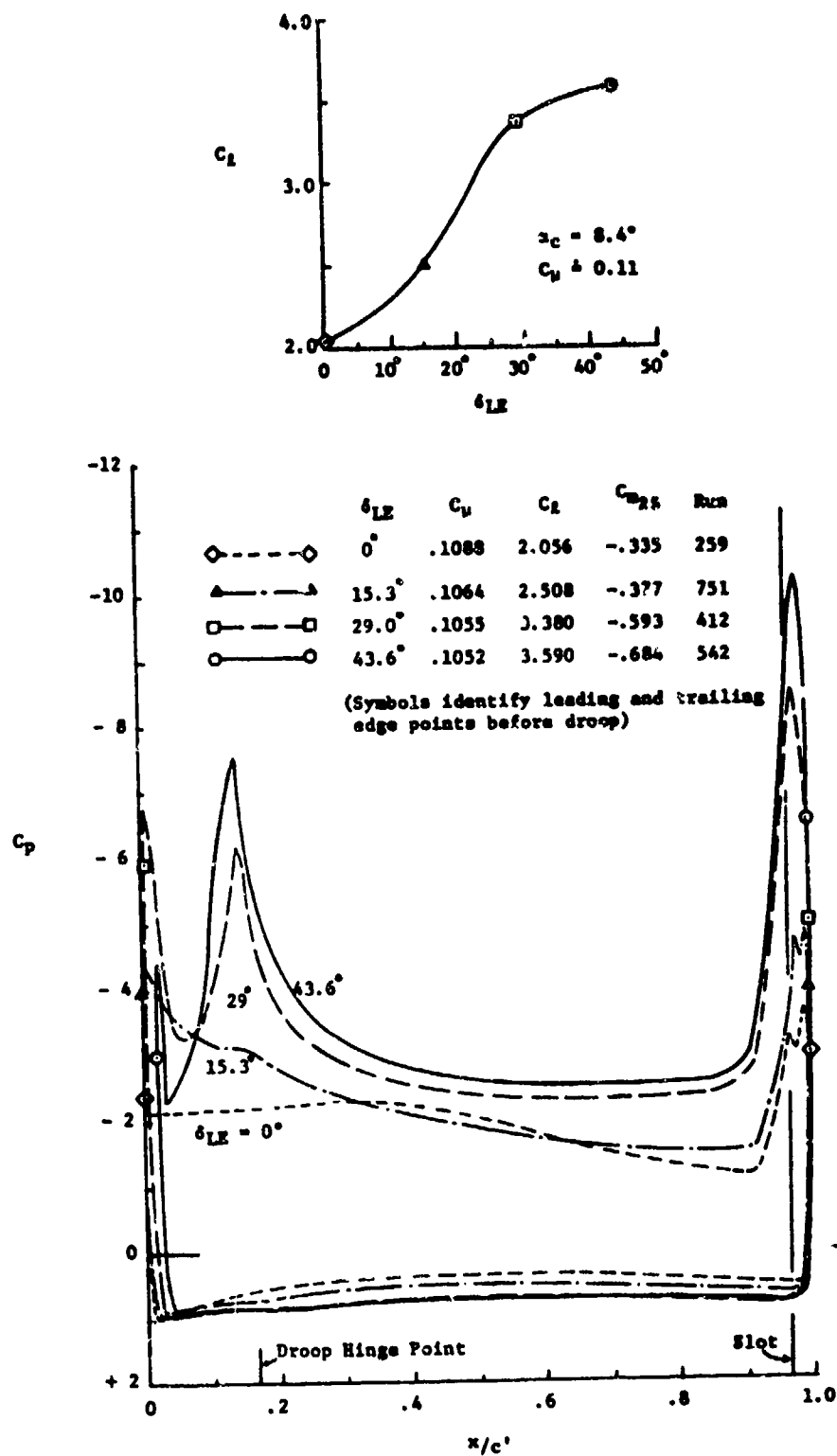


Figure 10 - Effect of Droop on Preventing Leading Edge Separation, NACA 66-210/CCW Airfoil,  $\alpha_c = 8.4^\circ$ ,  $C_{\mu} \approx 0.11$ , Experimental Pressure Distributions

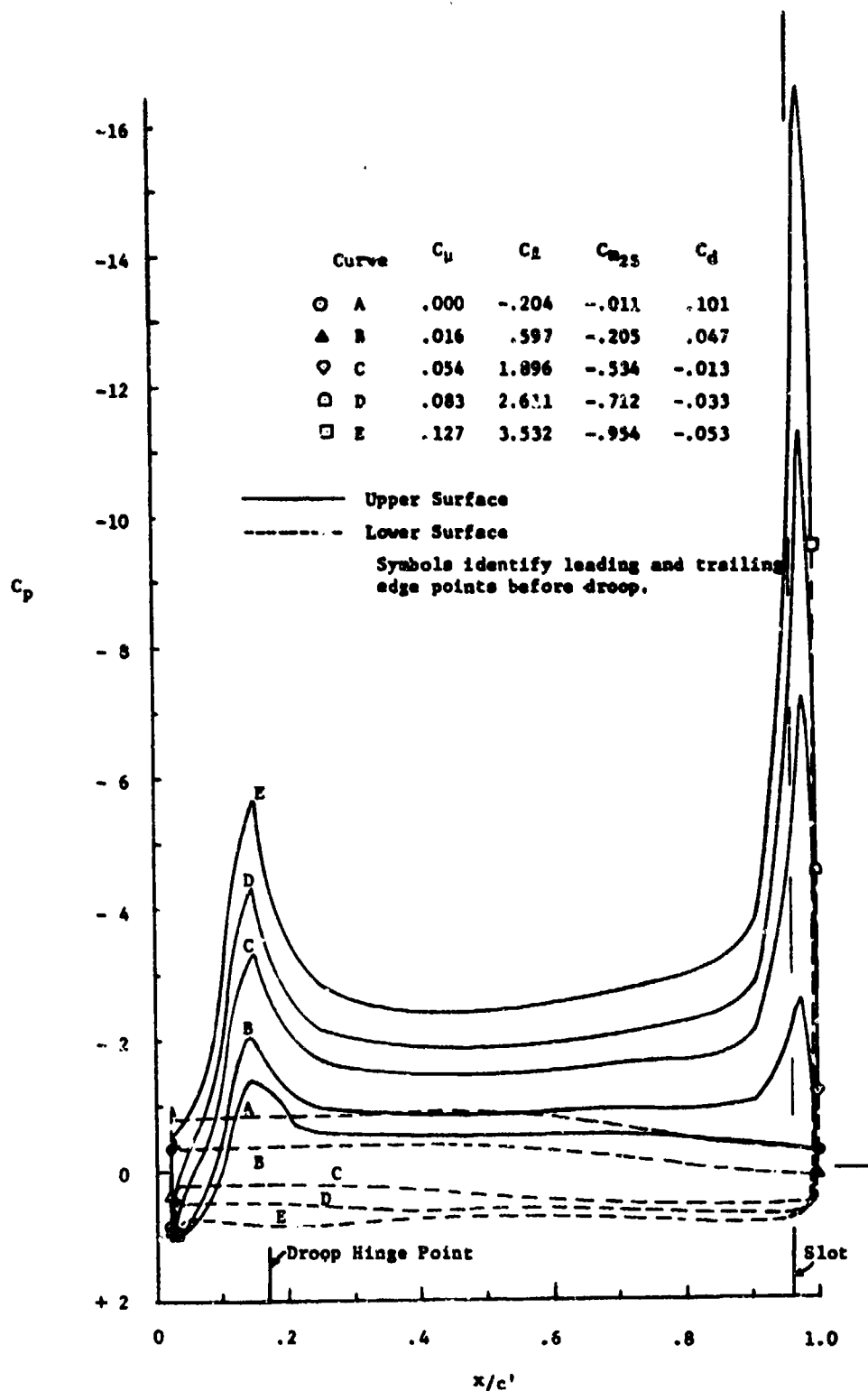


Figure 11 - Effect of Blowing on Experimental Pressure Distributions for NACA 66-210/CCW Airfoil,  $\delta_{LE} = 43.6^\circ$ ,  $\alpha_c = -0.86^\circ$

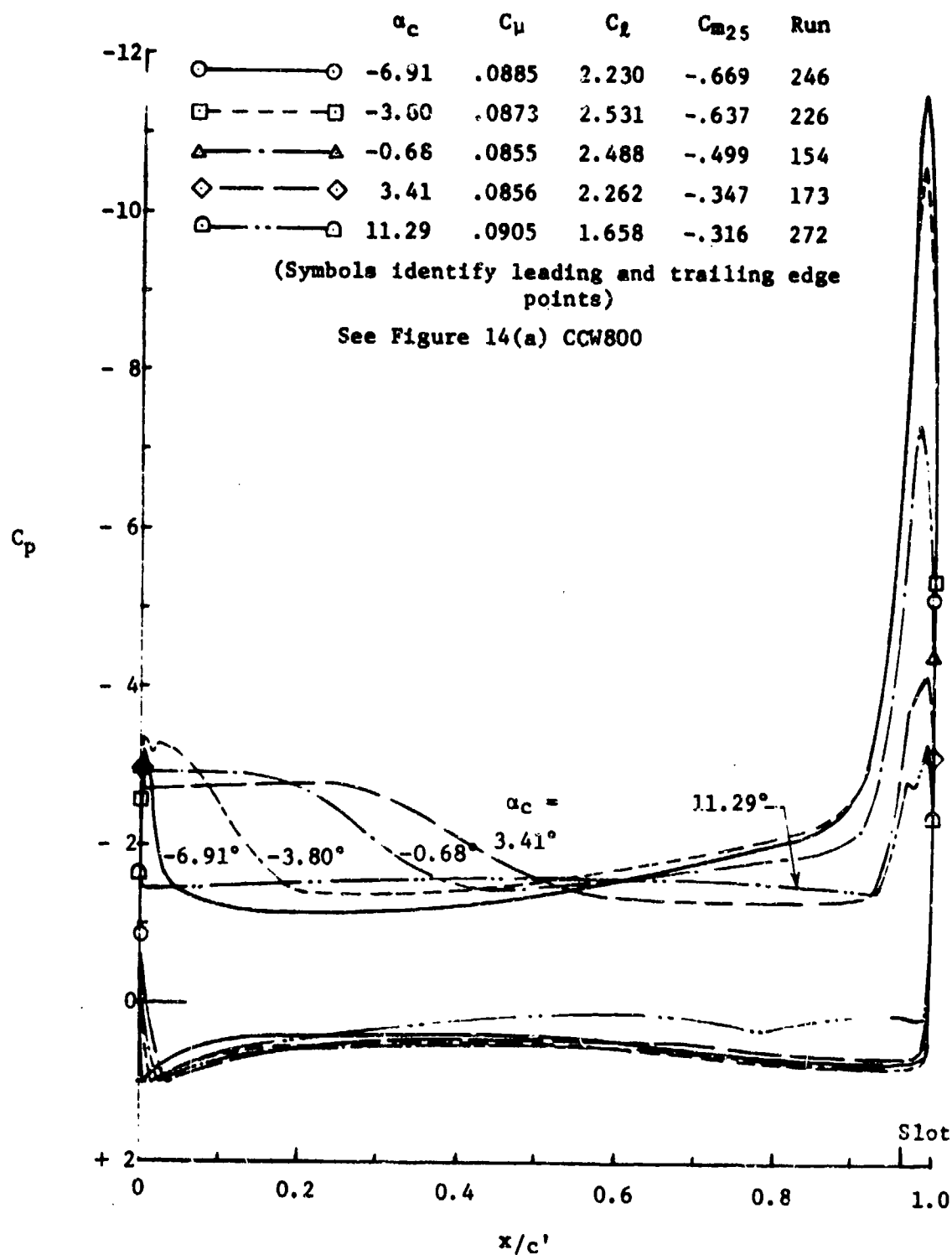


Figure 12 - Effect of Incidence on NACA 66-210/CCW with No Leading Edge Droop at  $C_\mu \approx .088$ , Experimental Pressure Distributions

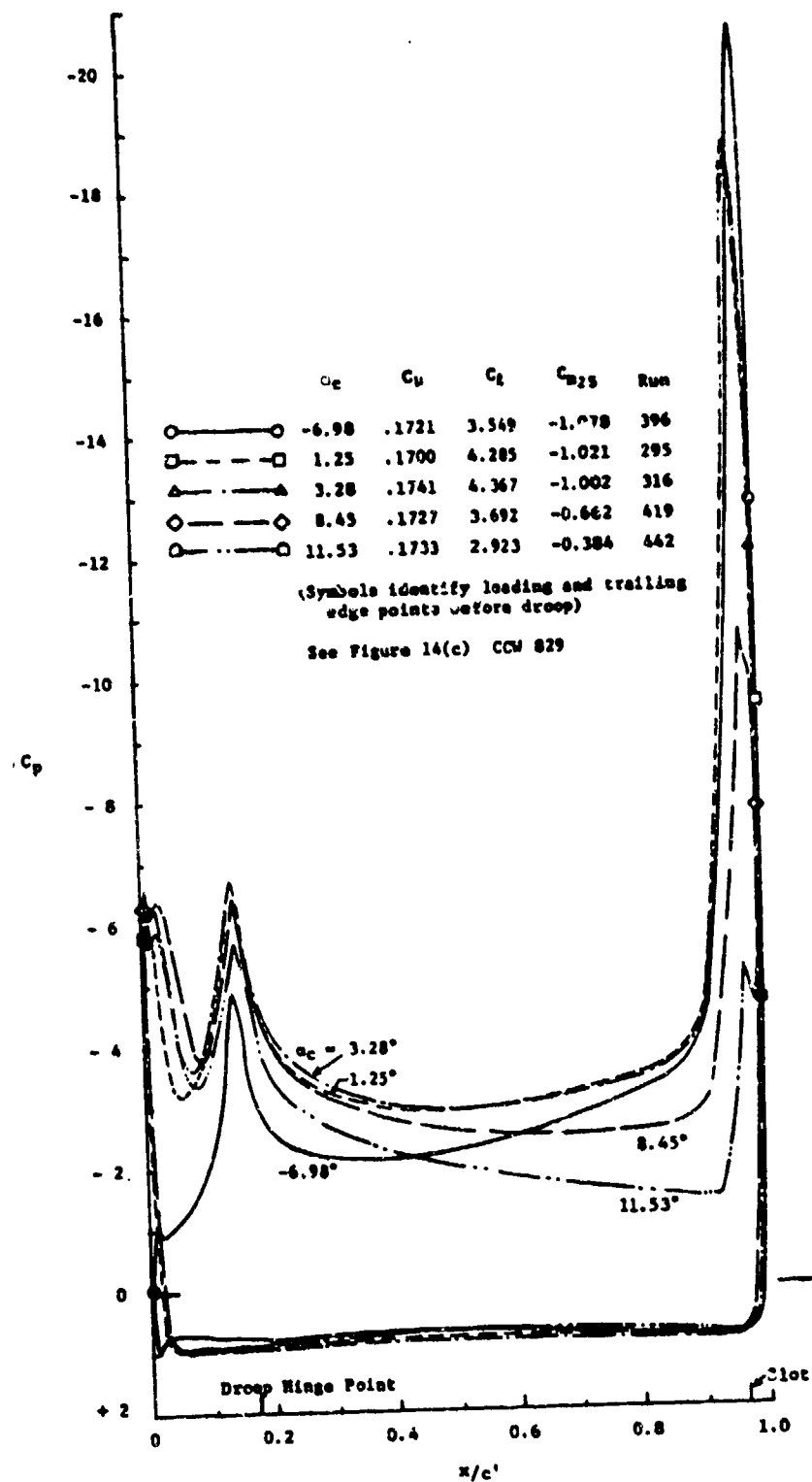


Figure 13 - Effect of Incidence on NACA 66-210/CCW Airfoil with 29° Leading Edge Droop at  $C_u \approx 0.173$ , Experimental Pressure Distributions

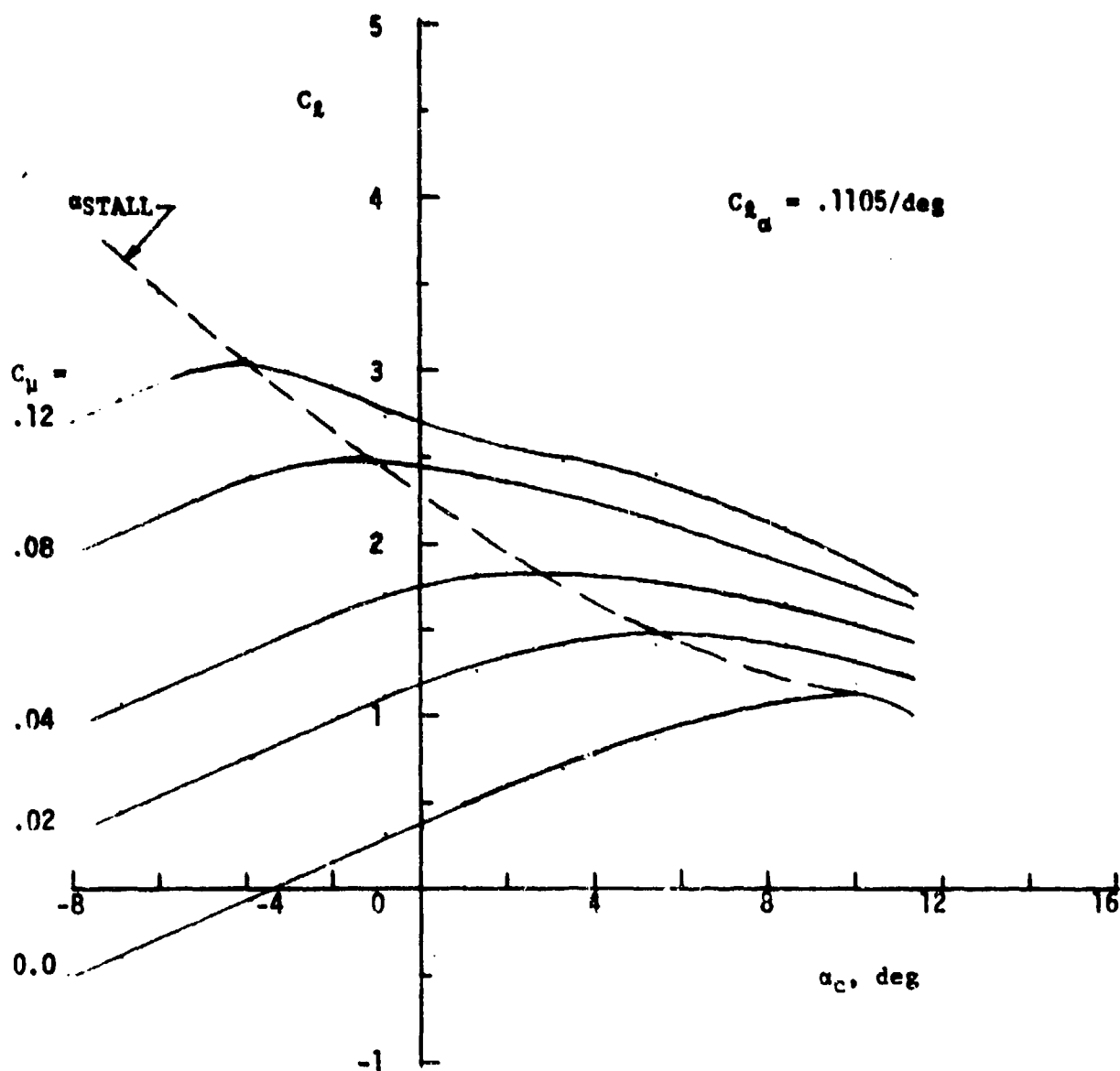


Figure 14 - Lift Curves at Constant Momentum Coefficient for  
66-210/CCW Airfoils,  $q = 30$  psf,  $R_e \approx 0.64 \times 10^6$ ,  
 $h = .009''$

(a) CCW 800,  $\delta_{LE} = 0^\circ$

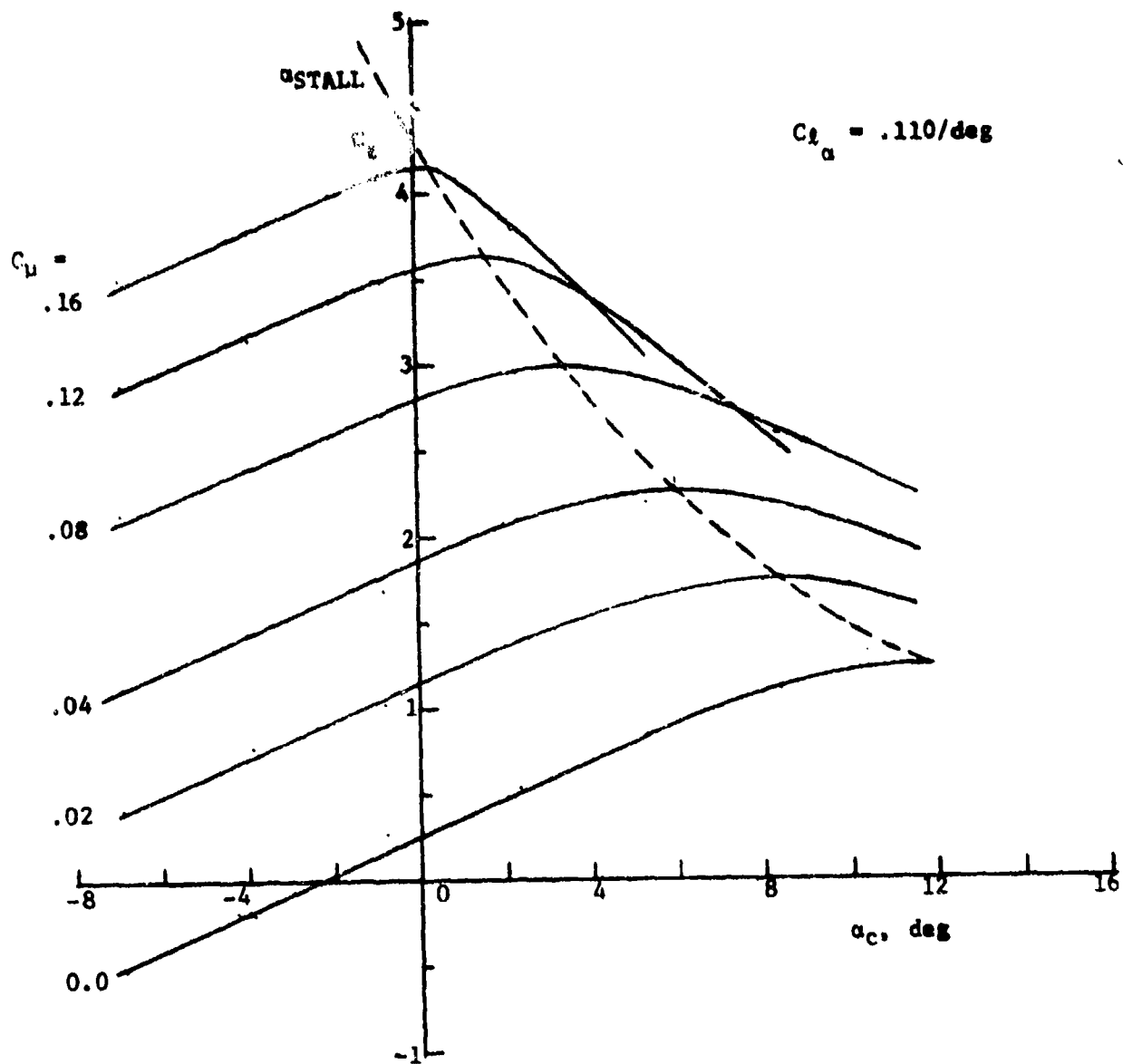


Figure 14 - Continued  
(b) CCW 815,  $\delta_{LE} = 15.3^\circ$

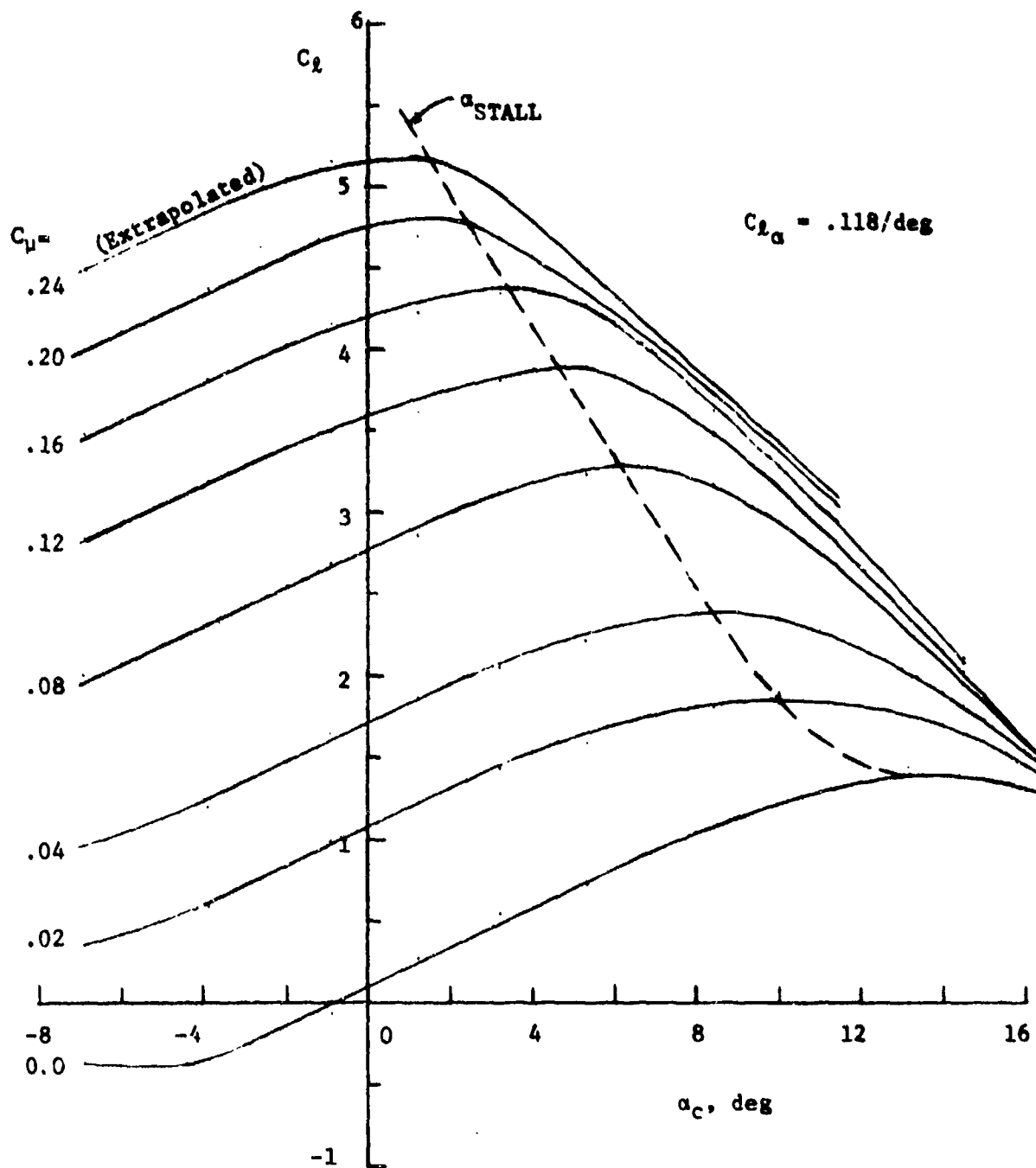


Figure 14 - Continued  
(c) CCW 829,  $\delta_{LE} = 29^\circ$

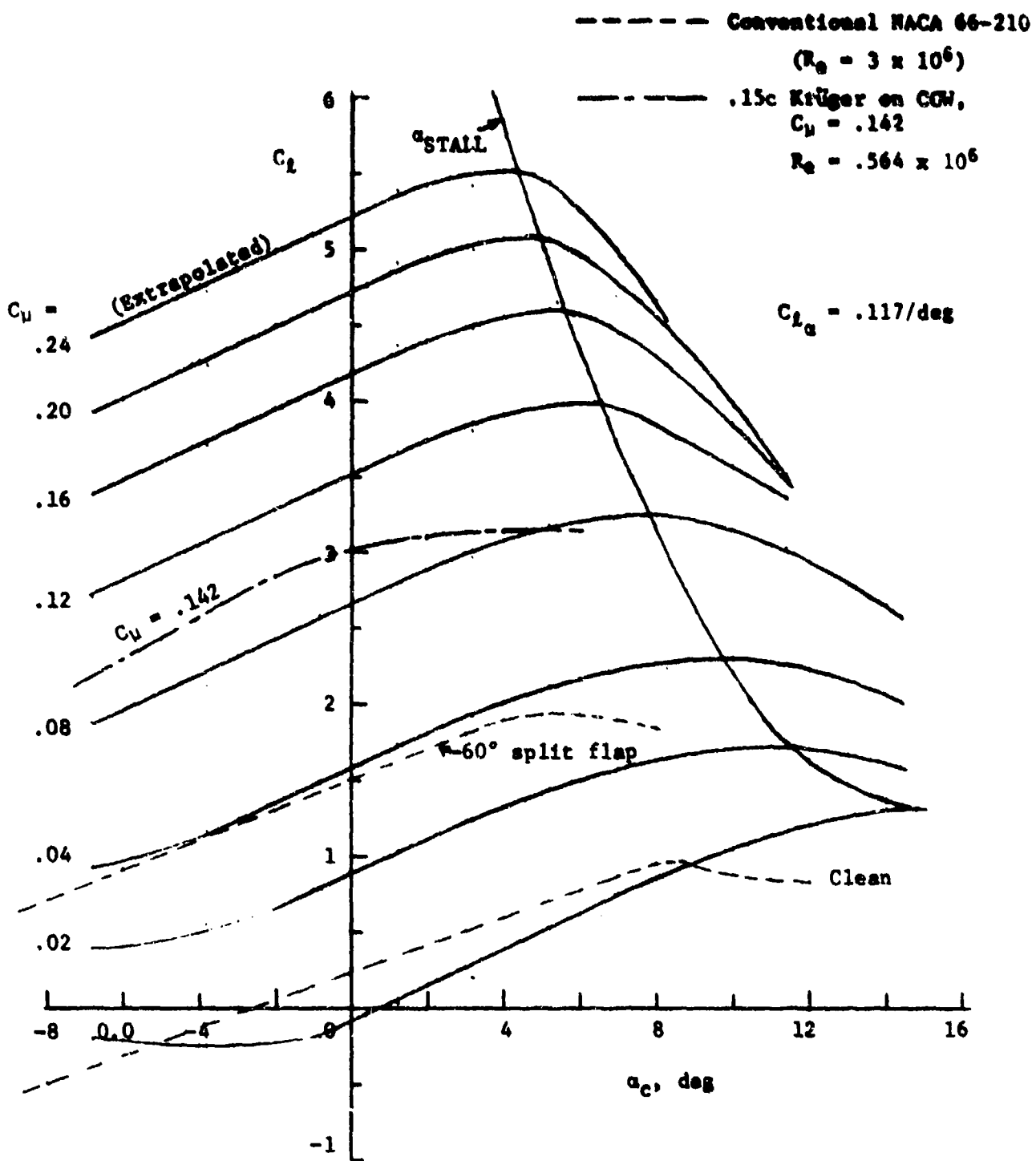


Figure 14 - Concluded  
 (d) CCW 844,  $\delta_{LE} = 43.6^\circ$



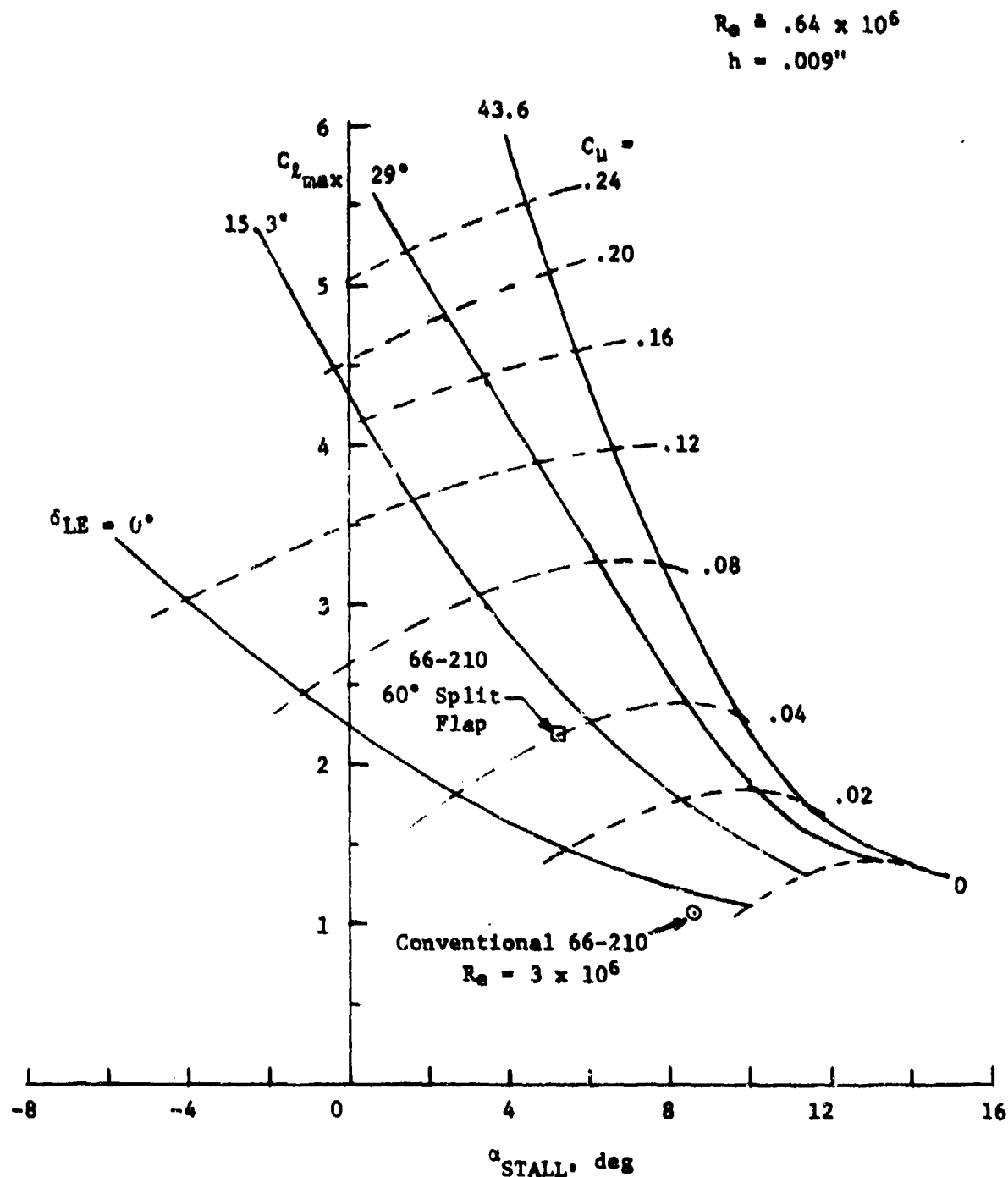


Figure 15 -  $C_{L_{max}}$  and  $\alpha_{STALL}$  as Functions of Momentum Coefficient and Nose Droop Angle for 66-210/CCW Airfoils

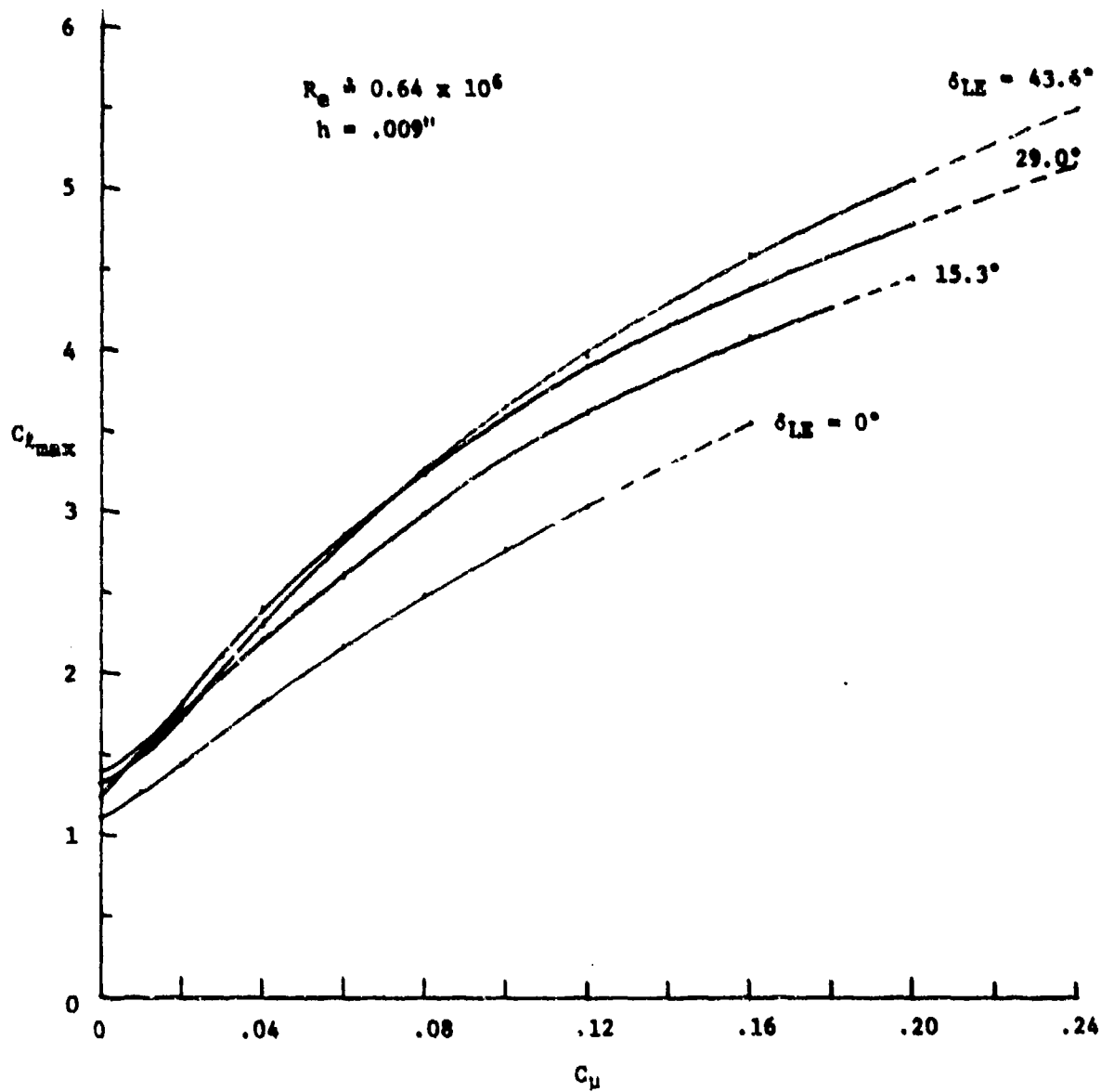


Figure 1C -  $C_{l_{max}}$  as a Function of Droop and Momentum  
 Coefficient, NACA 66-210/CCW Airfoils

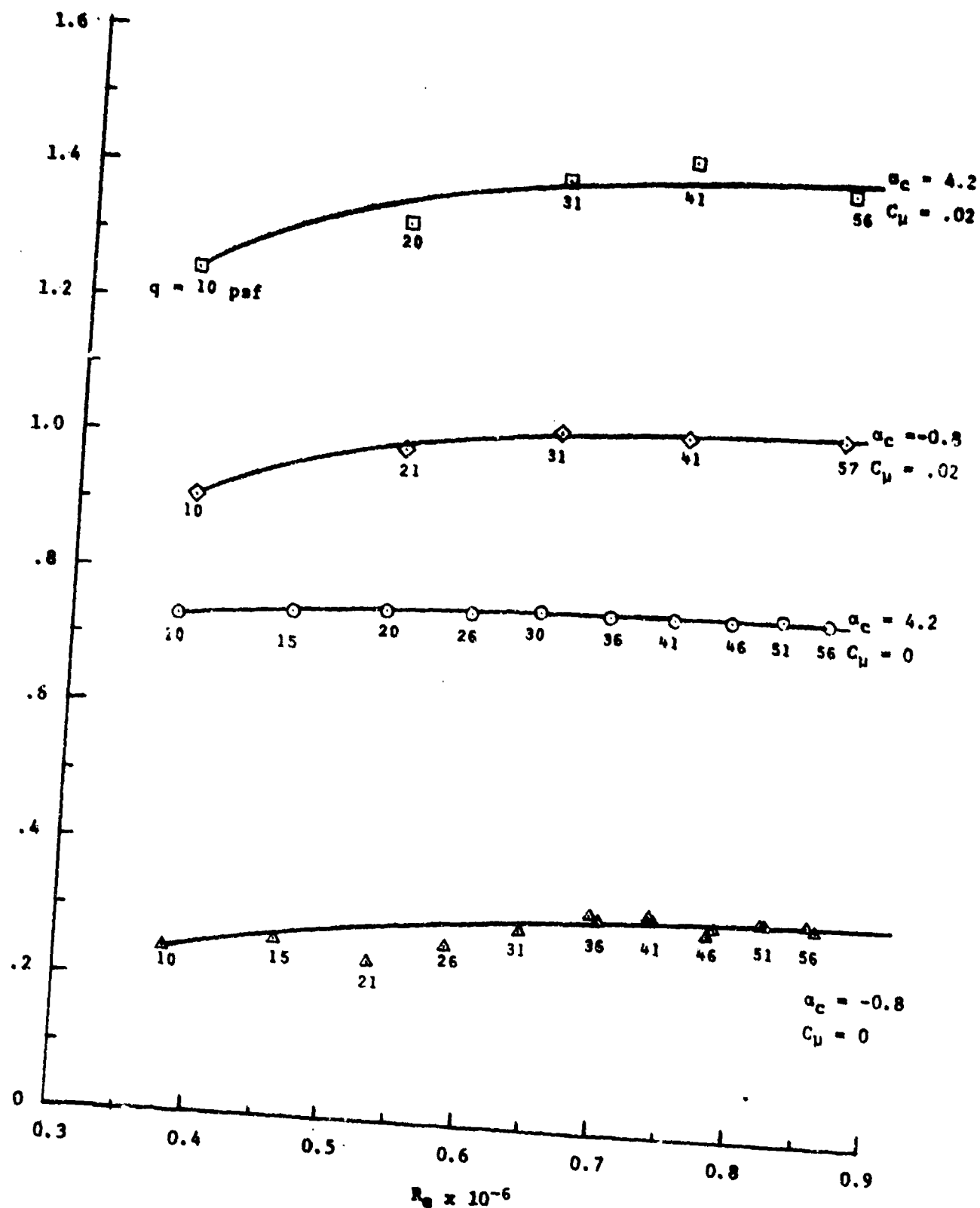


Figure 17 - Effects of Reynolds Number on Lift Coefficient for NACA 66-210/CCW Airfoil, CCW 800,  $\delta_{LE} = 0^\circ$ ,  $h = .009$ "

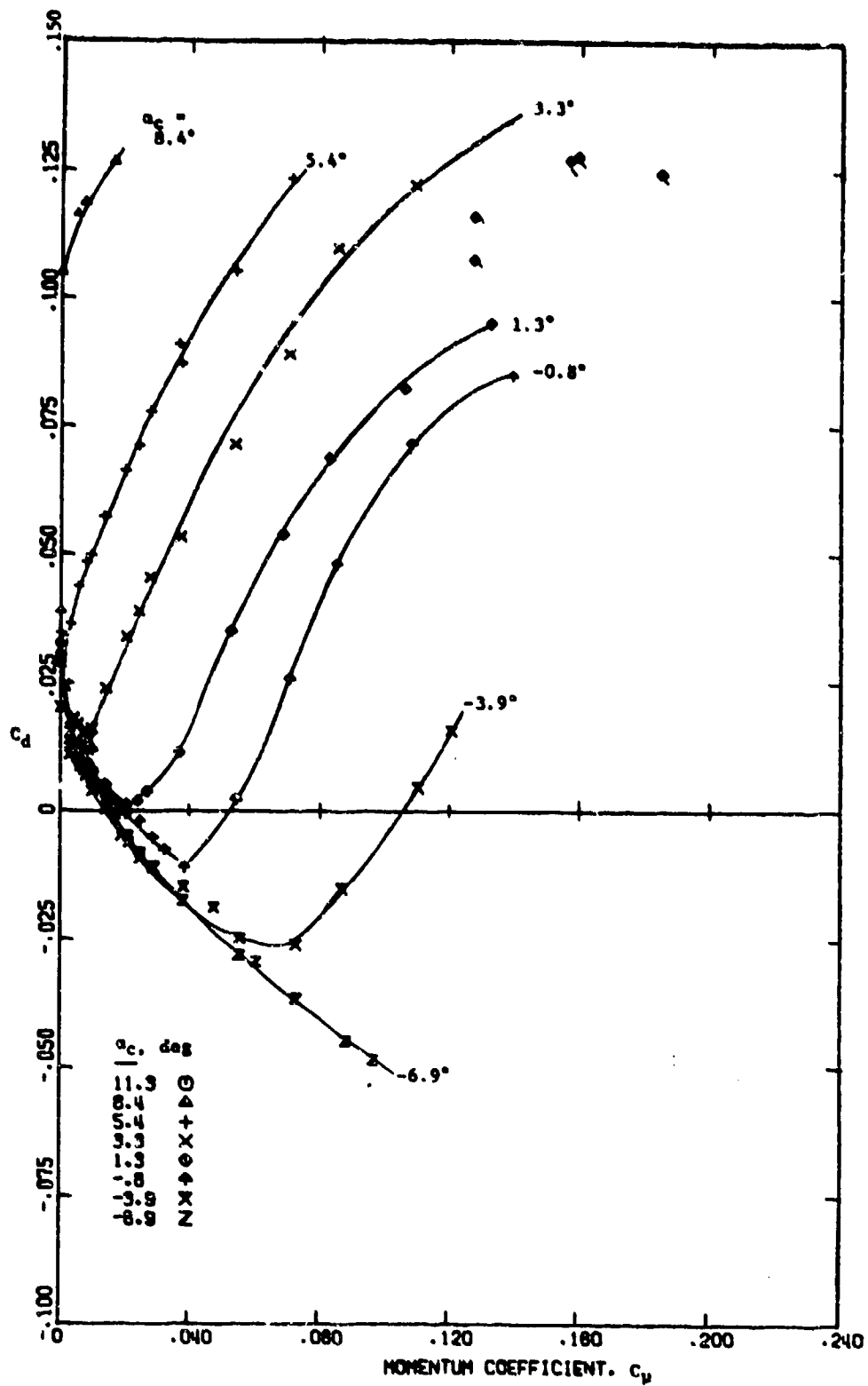


Figure 18 - Drag as a Function of Blowing for the NACA 66-210/CCW  
Airfoils,  $q = 30$  psf,  $R_e = 0.64 \times 10^6$ ,  $h = 0.009''$   
(a) CCW 800,  $\delta_{LE} = 0^\circ$

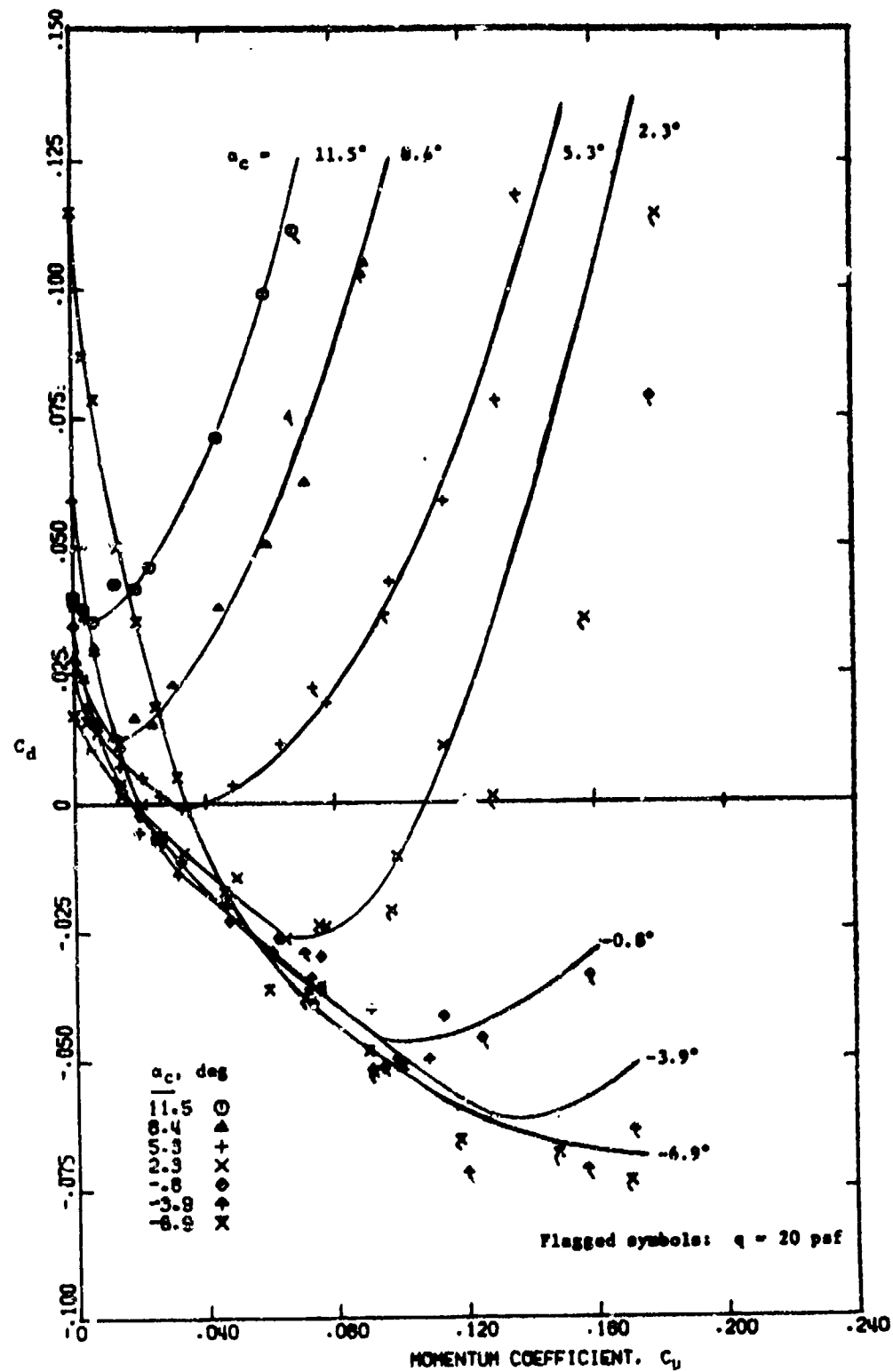


Figure 18 - (Continued)

(b) CCW 815,  $\delta_{LE} = 15.3^\circ$

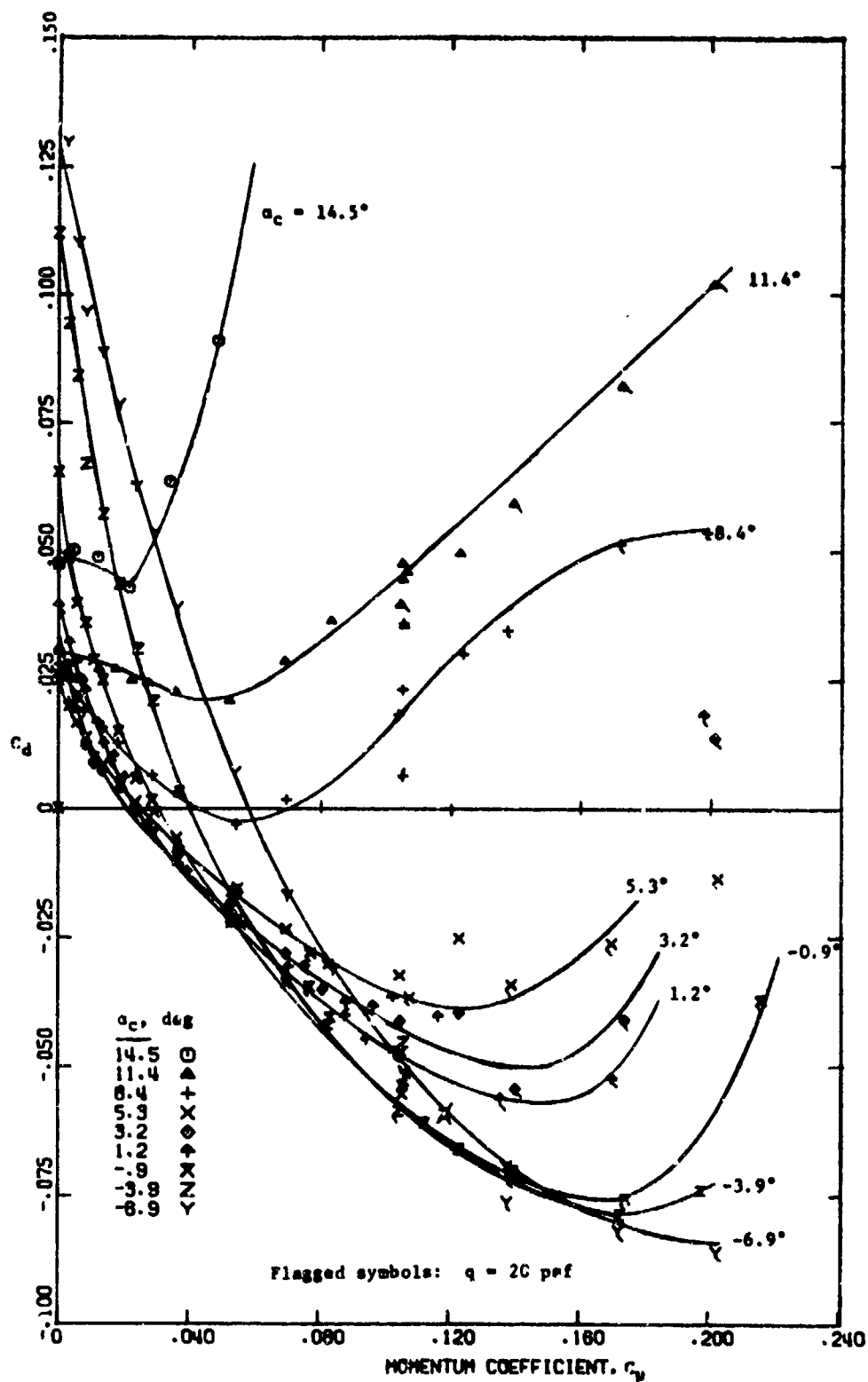


Figure 18 - (Continued)

(c) CCW 829,  $\delta_{LE} = 29^\circ$

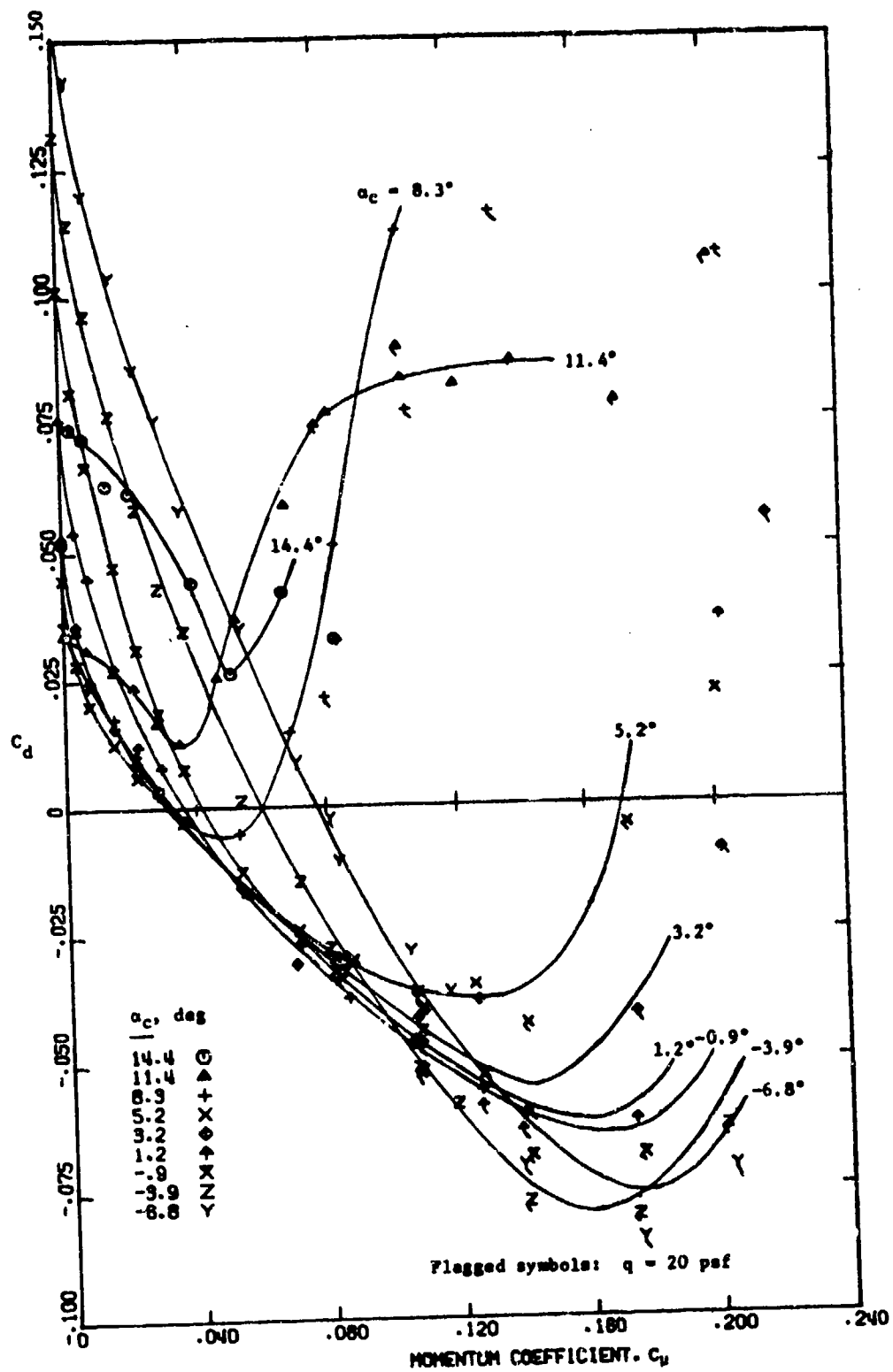


Figure 18 - (Concluded)

(d) CCW 844,  $\delta_{LE} = 43.6^\circ$

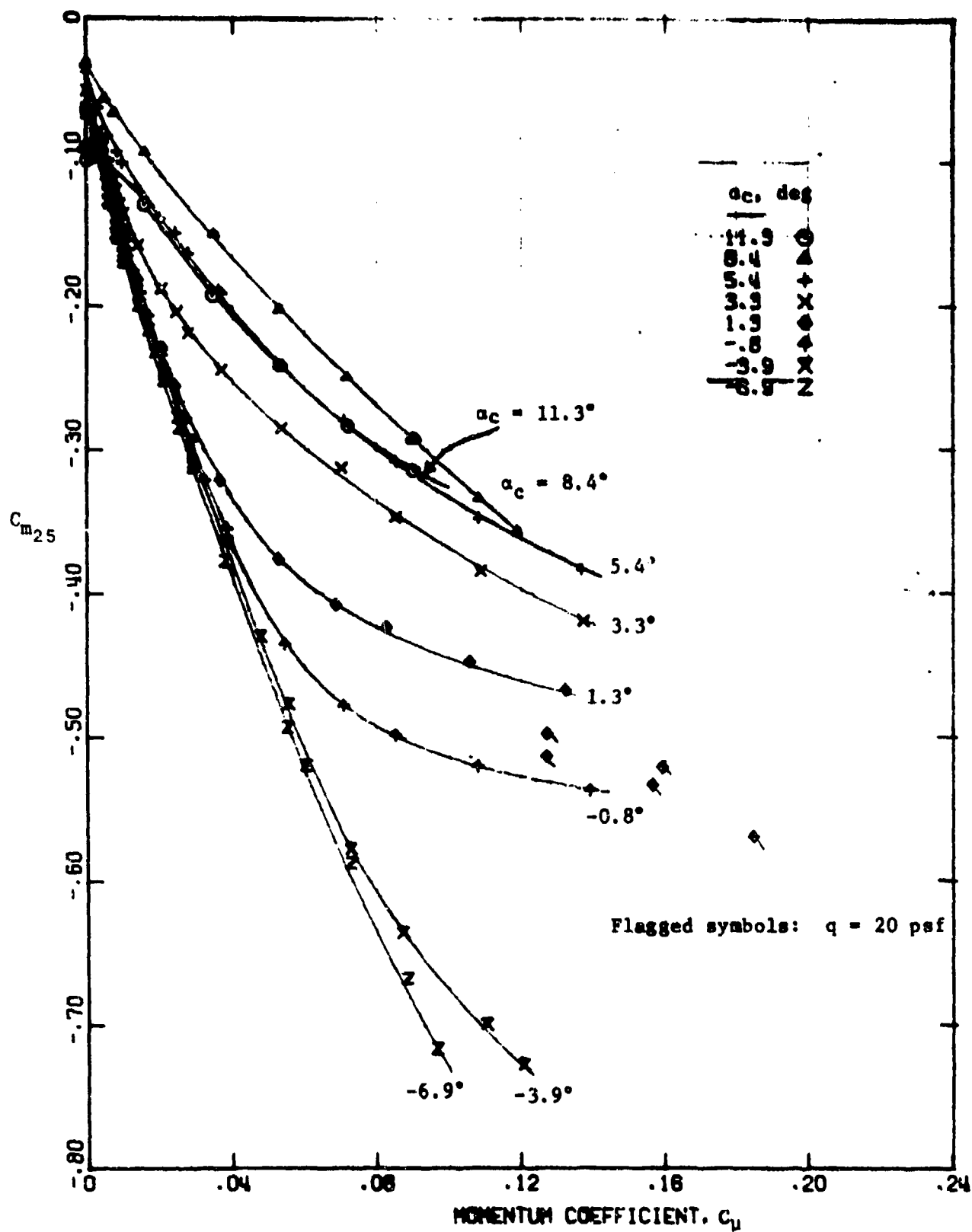


Figure 19 - Pitching Moment as a Function of Blowing for the NACA 66-210/CCW  
Airfoils,  $q = 30$  psf,  $R_e = 0.64 \times 10^6$ ,  $h = 0.009''$   
(a) CCW 800,  $\delta_{LE} = 0^\circ$



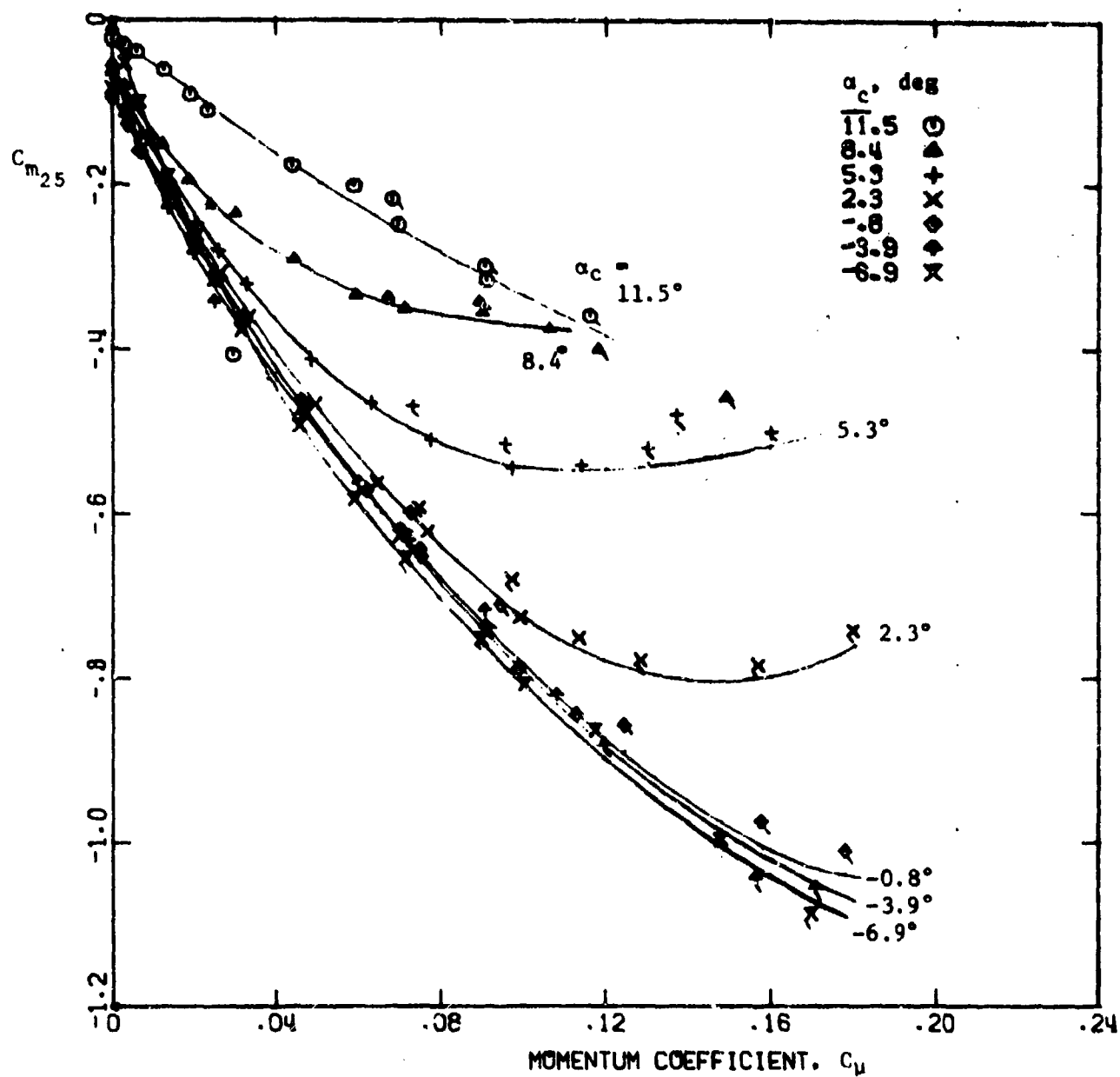


Figure 19 - (Continued)

(b) CCW 815,  $\delta_{LE} = 15.3^\circ$

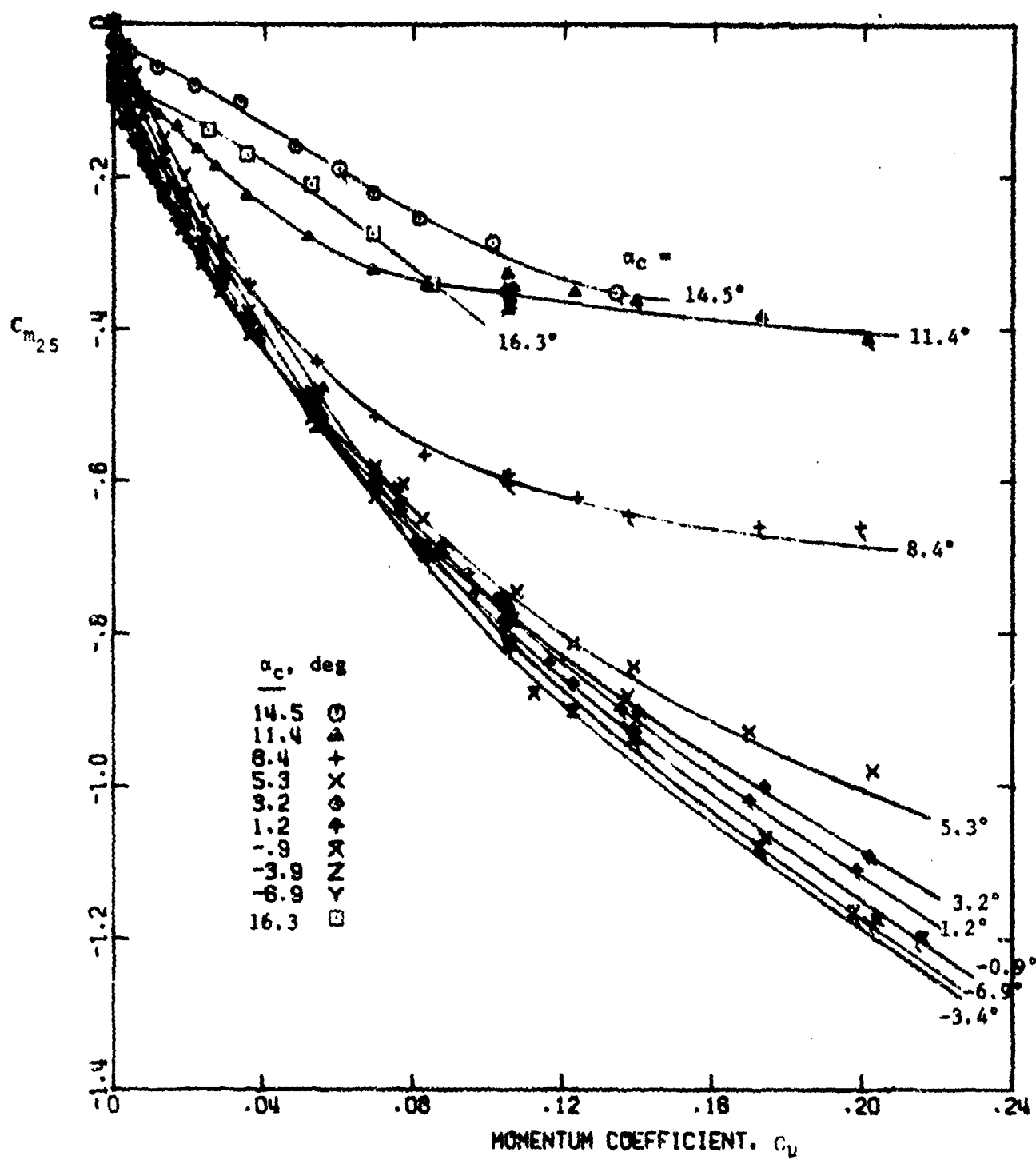


Figure 19 - (Continued)

(c) CCW 829,  $\delta_{LE} = 29^\circ$

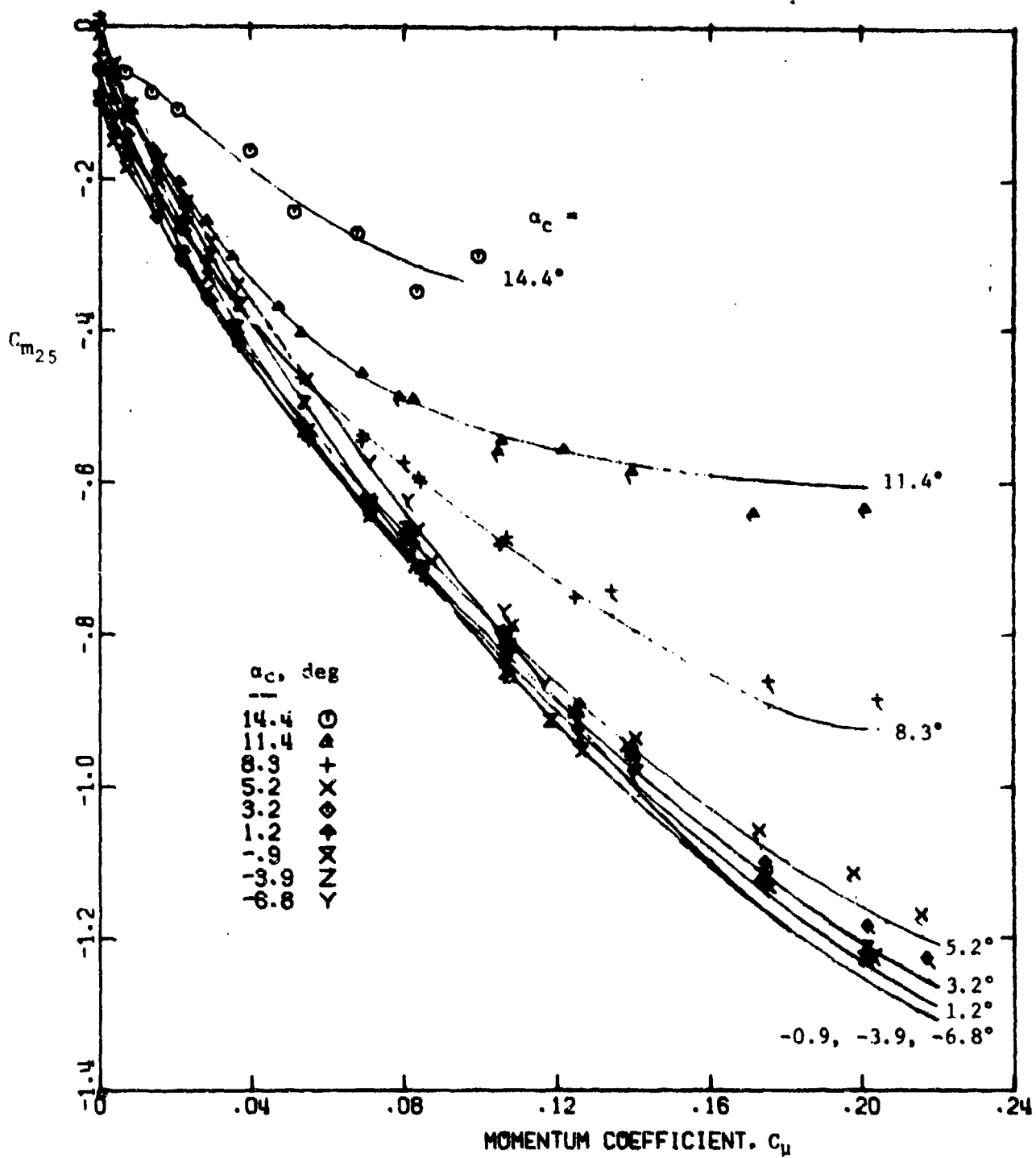


Figure 19 - (Concluded)

(d) CCW 844,  $\delta_{LE} = 43.6^\circ$

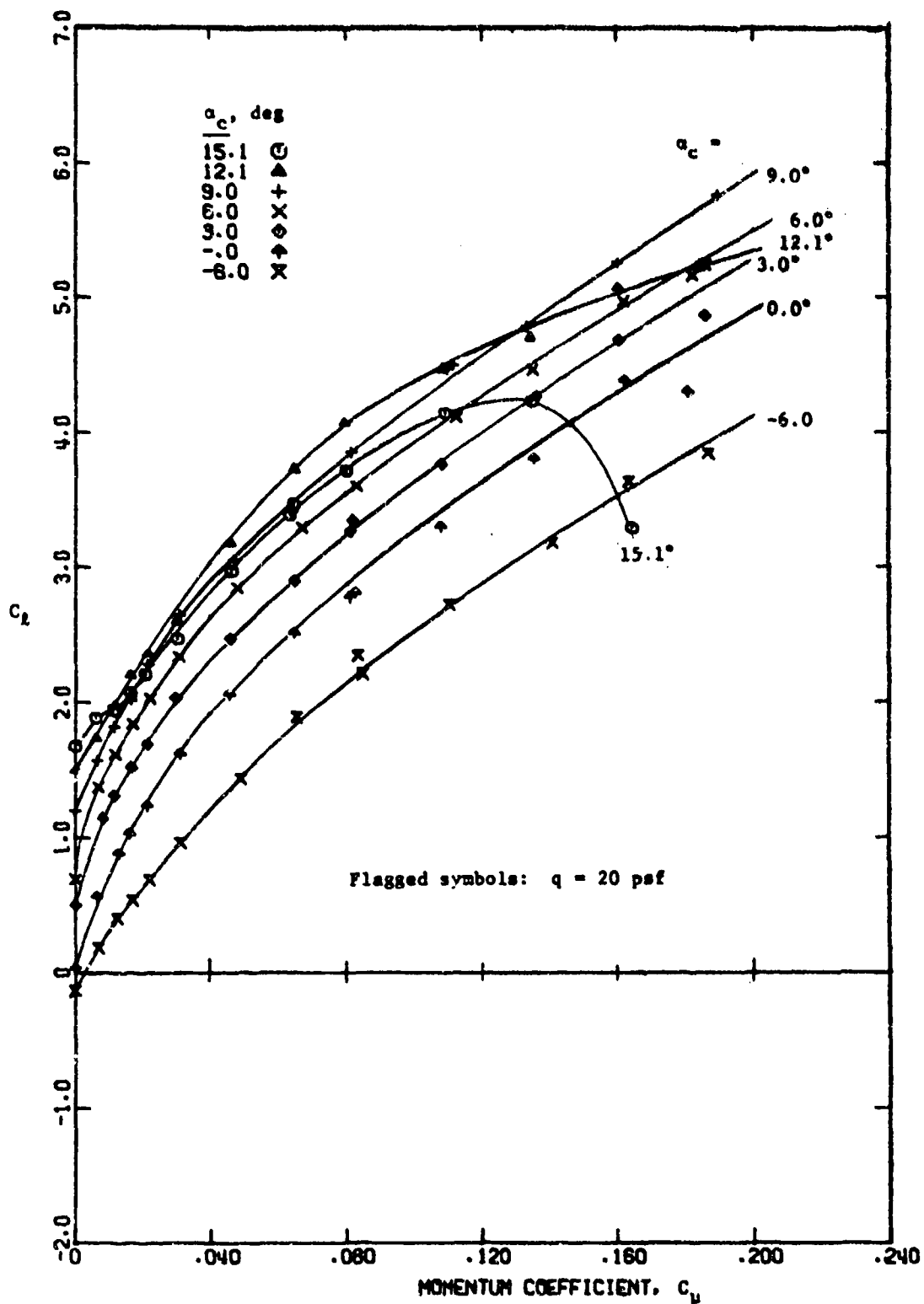


Figure 20 - Lift as a Function of Blowing for NACA 64A-212/CCW Airfoils,  
 $q = 30$  psf,  $R_e \approx 1.98 \times 10^6$ ,  $h = 0.027''$   
 (a) CCW 241,  $\beta_f = 180^\circ$ ,  $\delta_{LE} = 30^\circ$

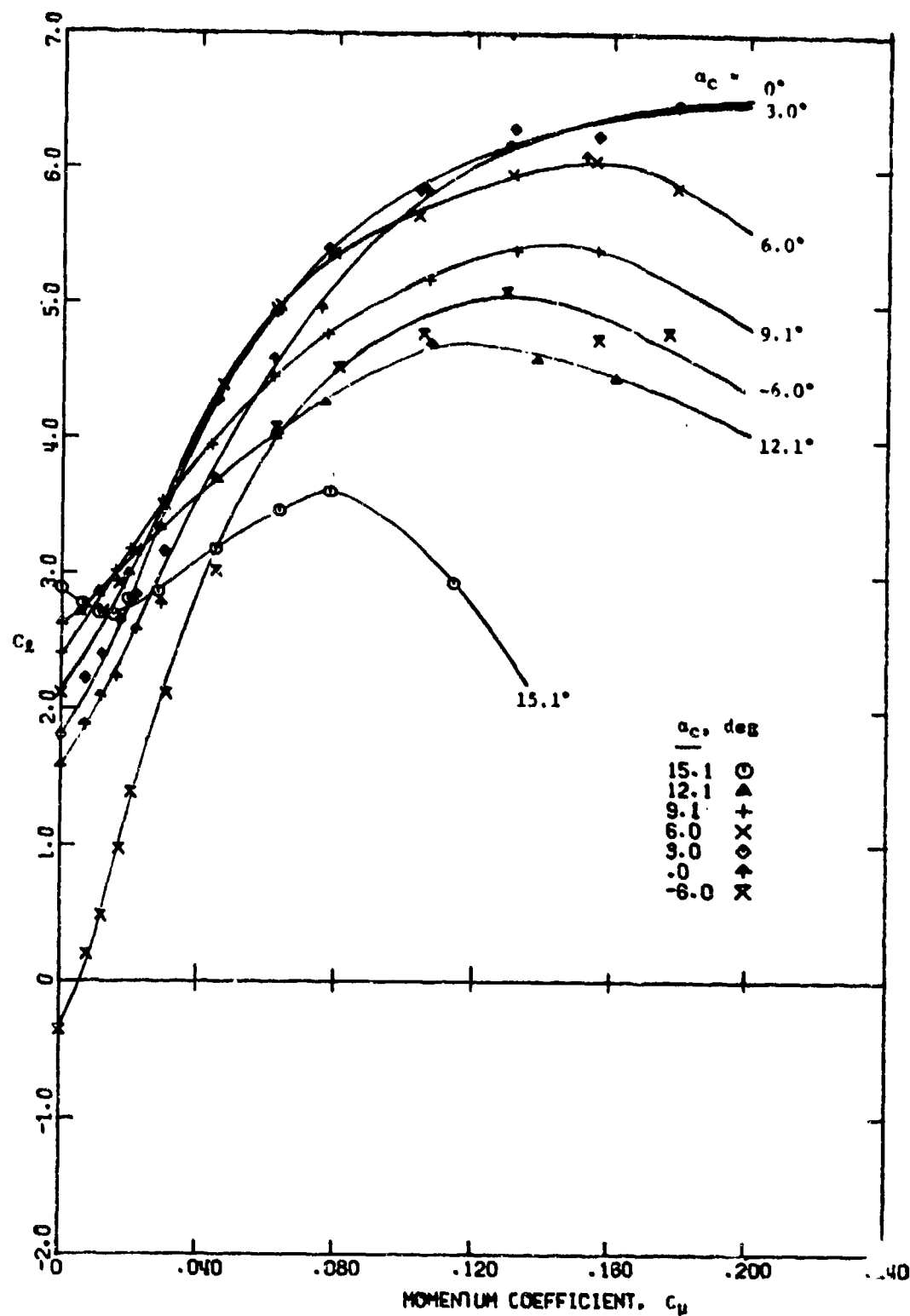


Figure 20 - (Continued)

(b) CCW 242,  $\delta_f = 90^\circ$ ,  $\delta_{LE} = 30^\circ$

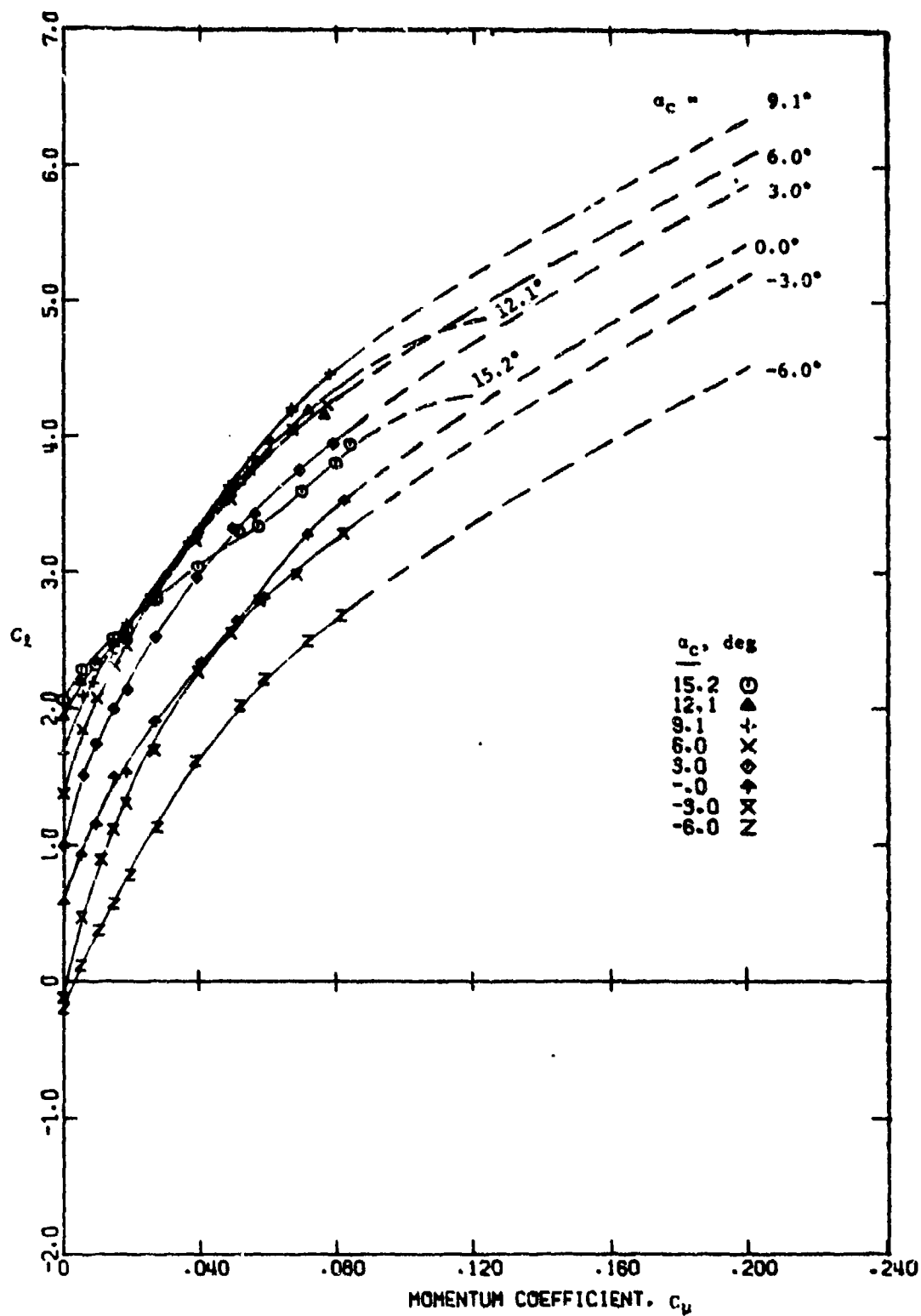


Figure 20 - (Continued)

(c) CCW 243, Extended T.E.,  $\delta_{LE} = 30^\circ$

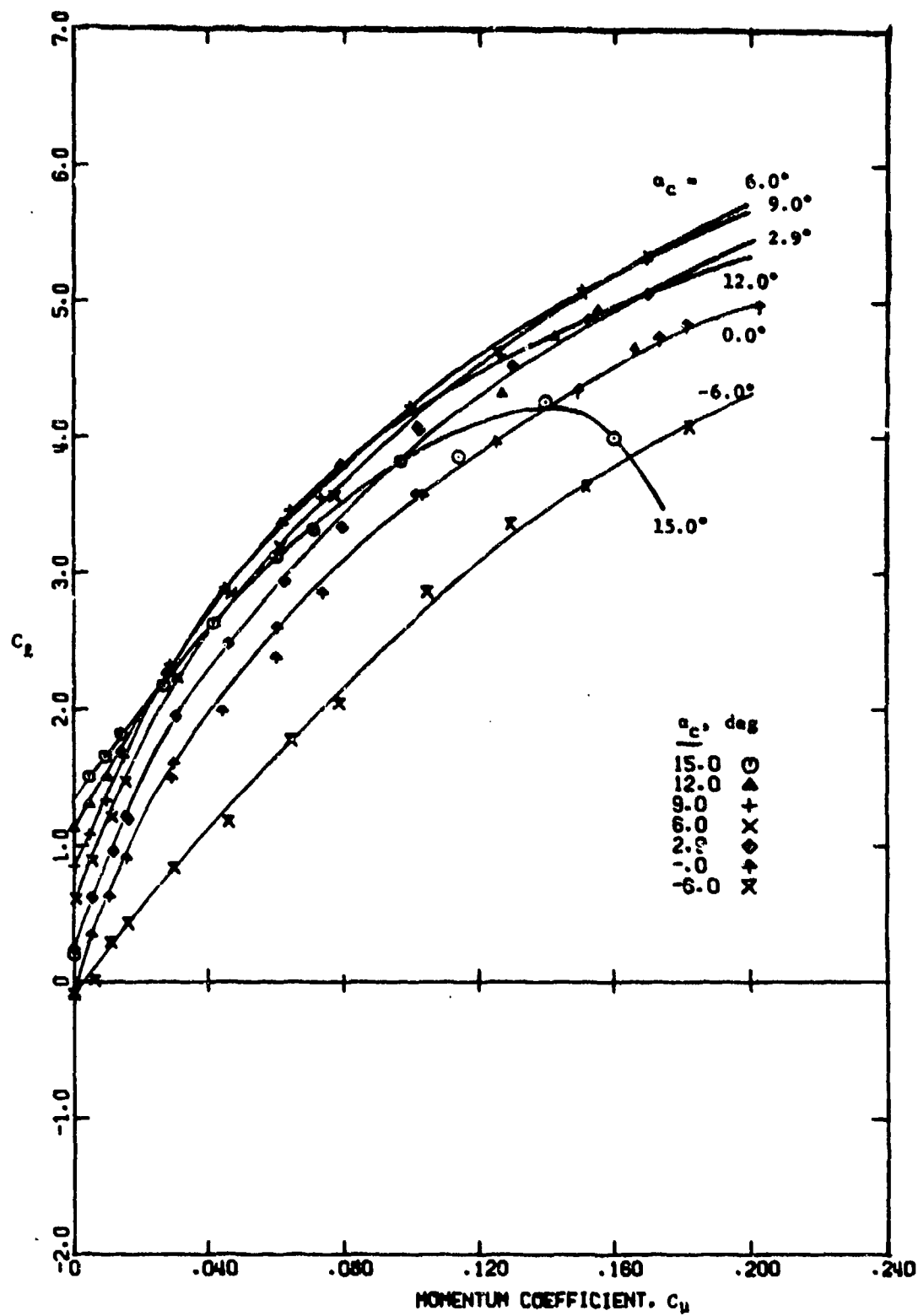


Figure 20 - (Continued)

(d) CCW 244, Reduced T.E.,  $\delta_{LE} = 30^\circ$

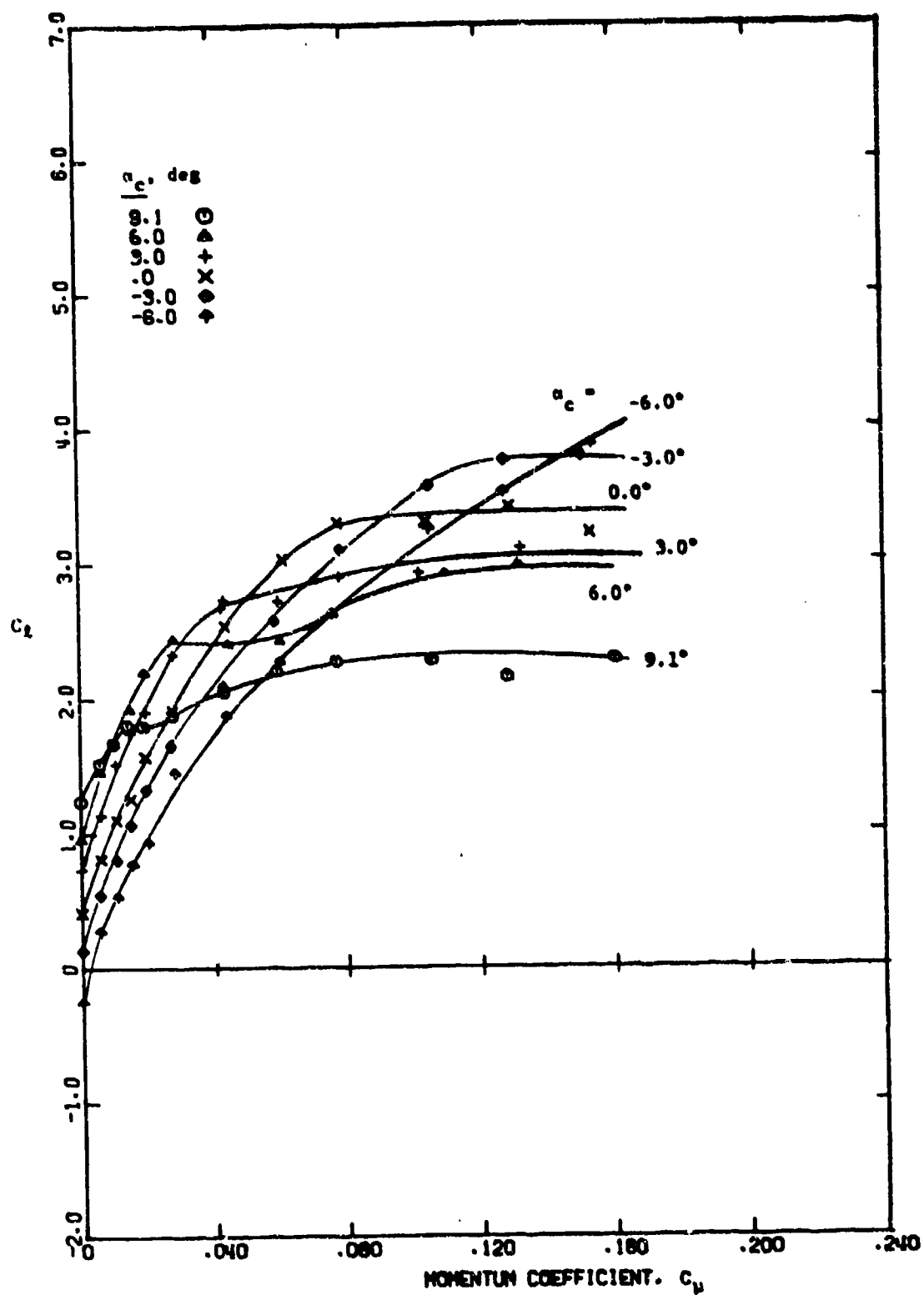


Figure 20 - (Concluded)

(e) CCW 245,  $\delta_f = 180^\circ$ ,  $\delta_{LE} = 0^\circ$



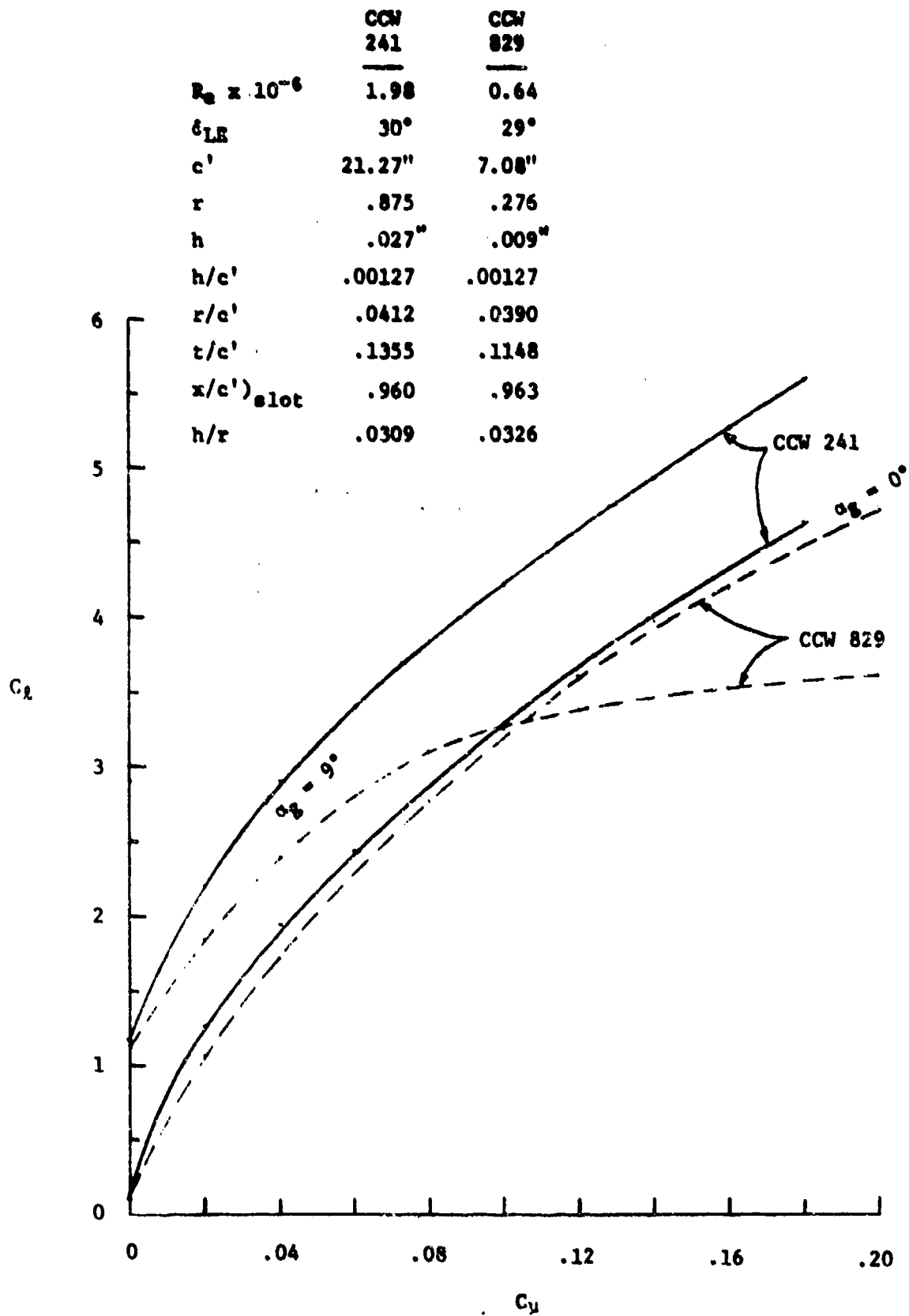


Figure 21 - Small and Large Chord CCW Airfoil Comparison

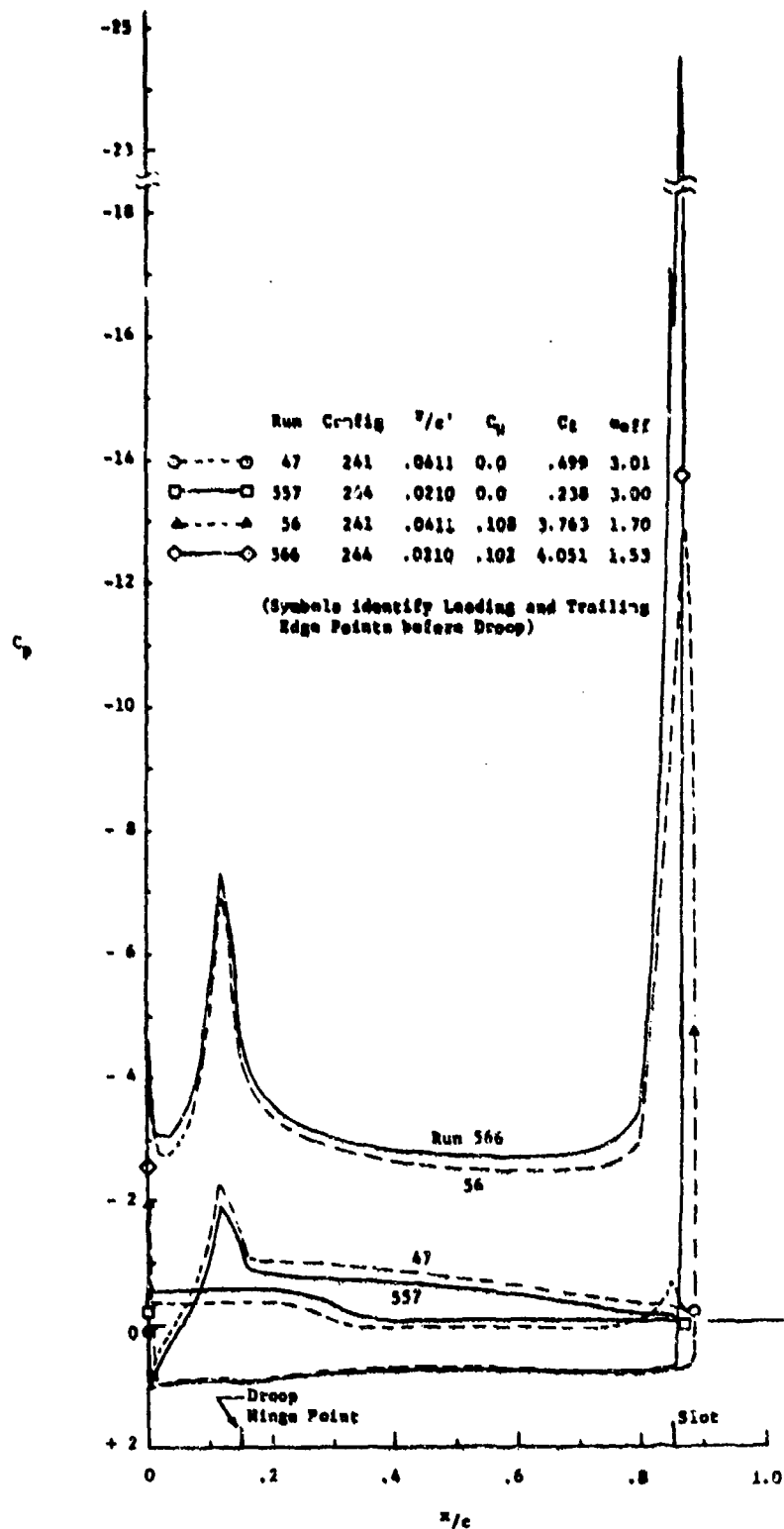


Figure 22 - Effects of Reduced Trailing Edge Radius - Comparison Between Configuration CCW 241 and CCW 244 Experimental Pressure Distributions

(a)  $\alpha_c \approx 3^\circ$

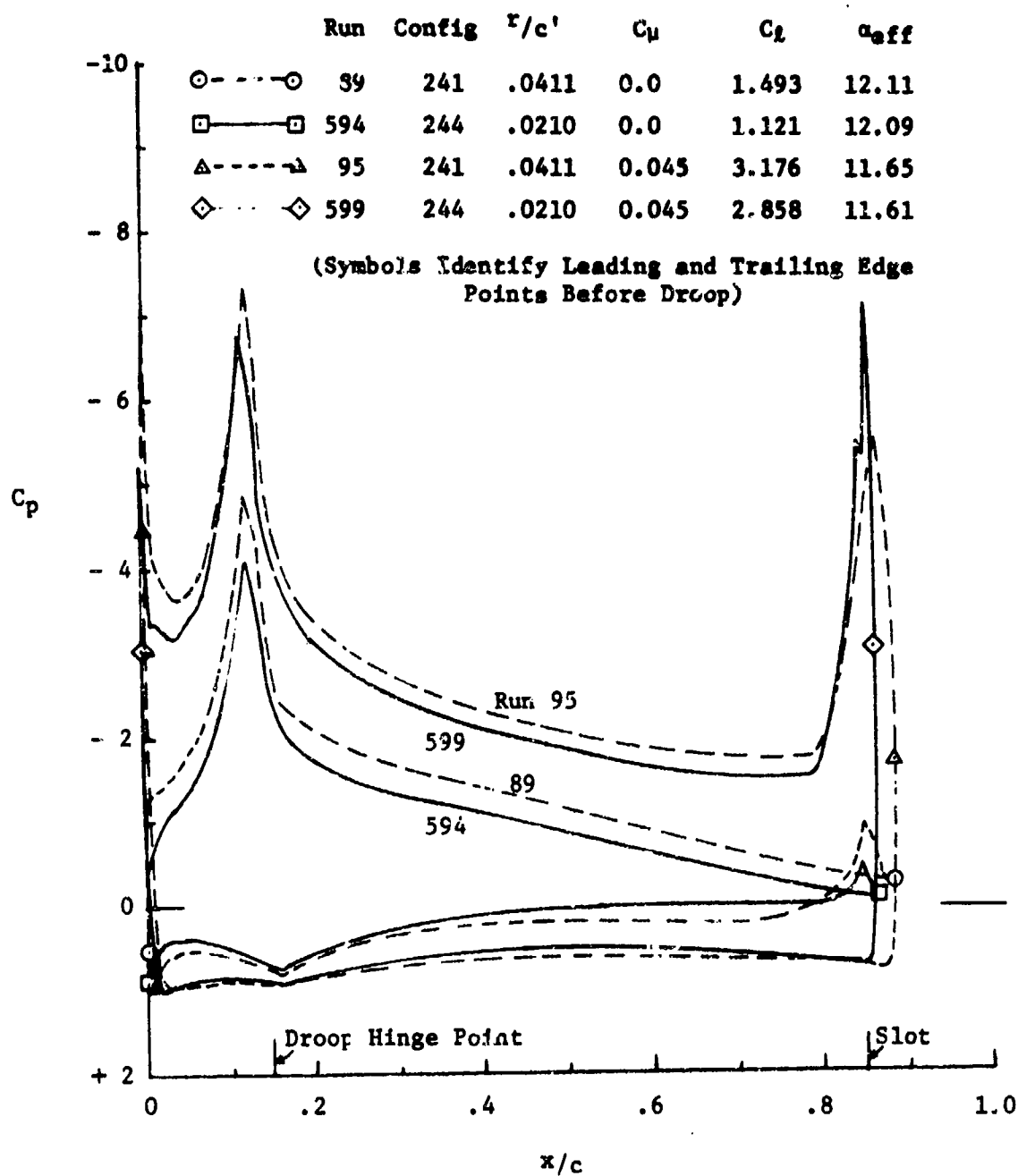


Figure 22 - Continued  
(b)  $\alpha_c \sim 12^\circ$

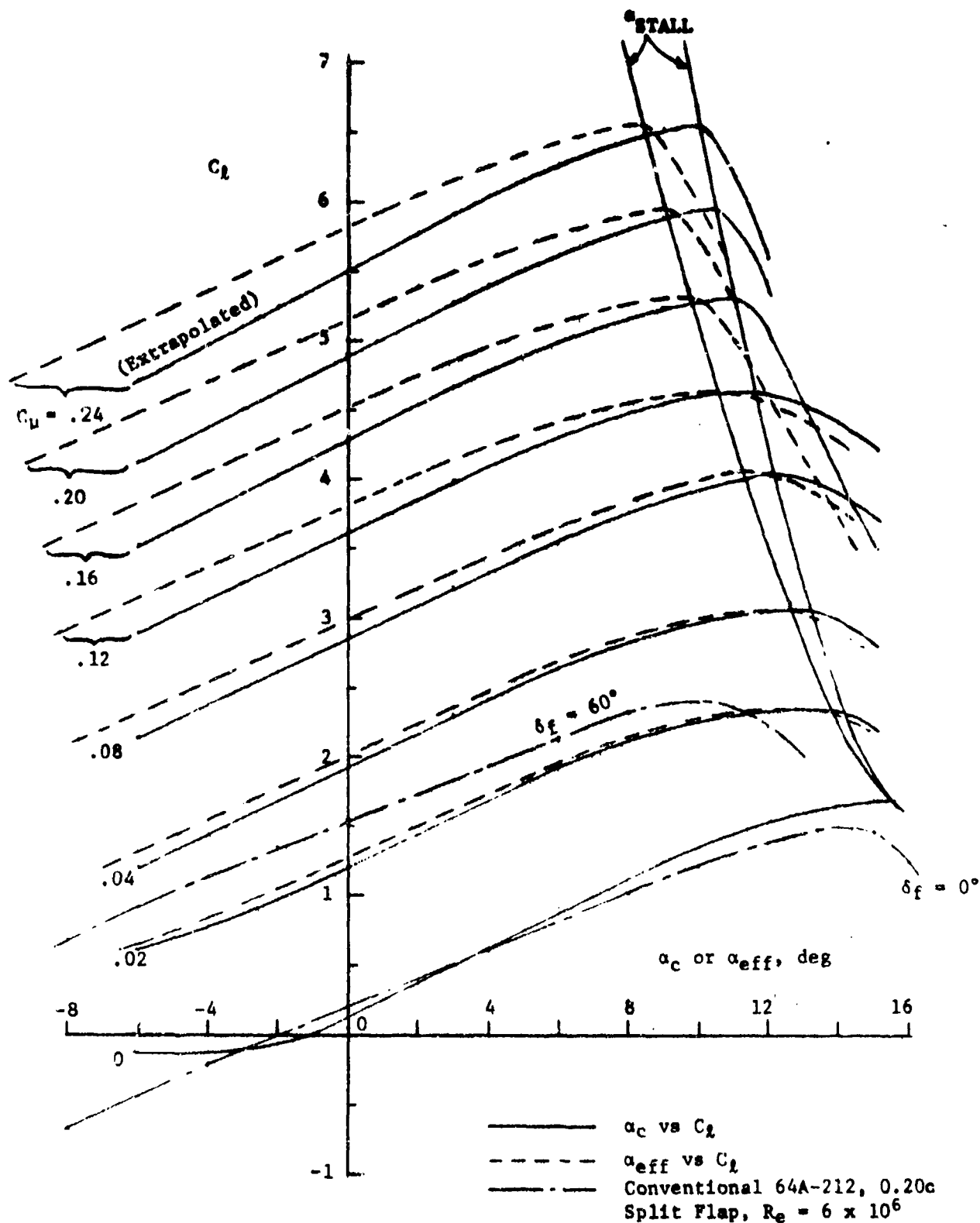


Figure 23 - Lift Curves at Constant Momentum Coefficient for 64A-212/CCW Airfoils  
 $q = 30 \text{ psf}$ ,  $R_e = 1.98 \times 10^6$ ,  $h = .027''$   
 (a) CCW 241,  $\delta_f = 180^\circ$ ,  $\delta_{LE} = 30^\circ$

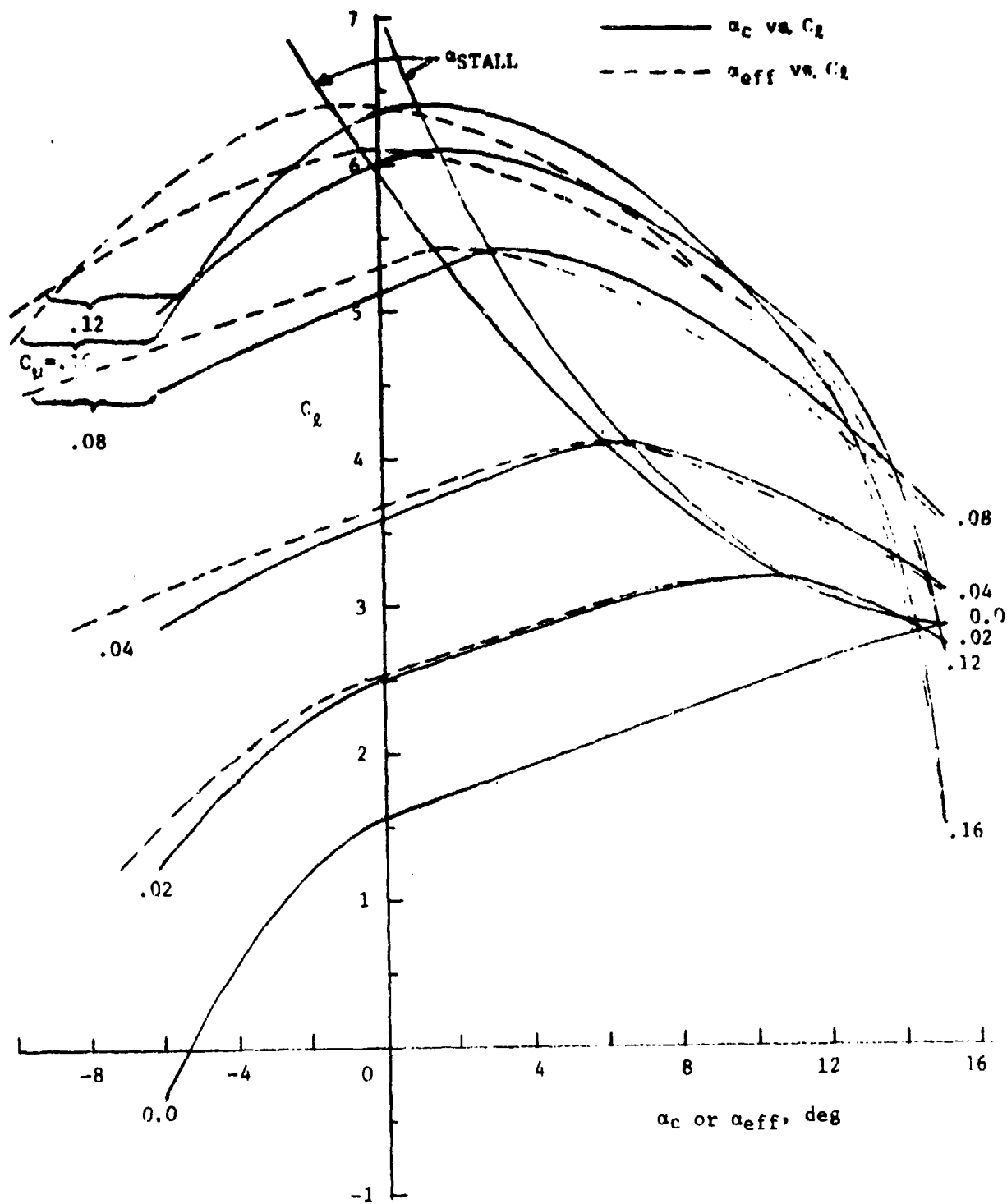


Figure 23 - Continued  
 (b) CCW 242,  $\delta_f = 90^\circ$ ,  $\delta_{r,E} = 30^\circ$

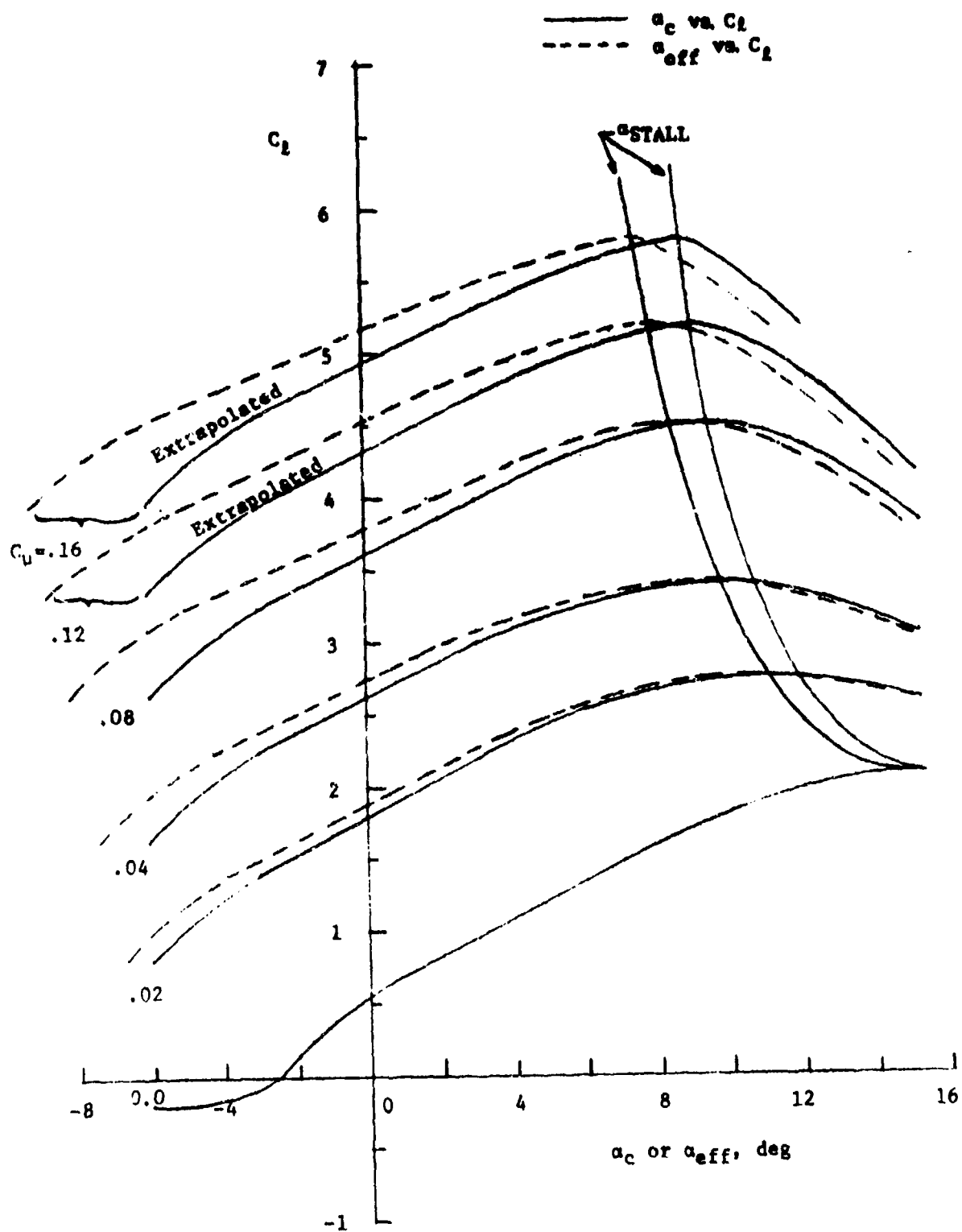


Figure 23 - Continued  
(c) CCW 243, Extended T.E.,  $\delta_{LE} = 30^\circ$

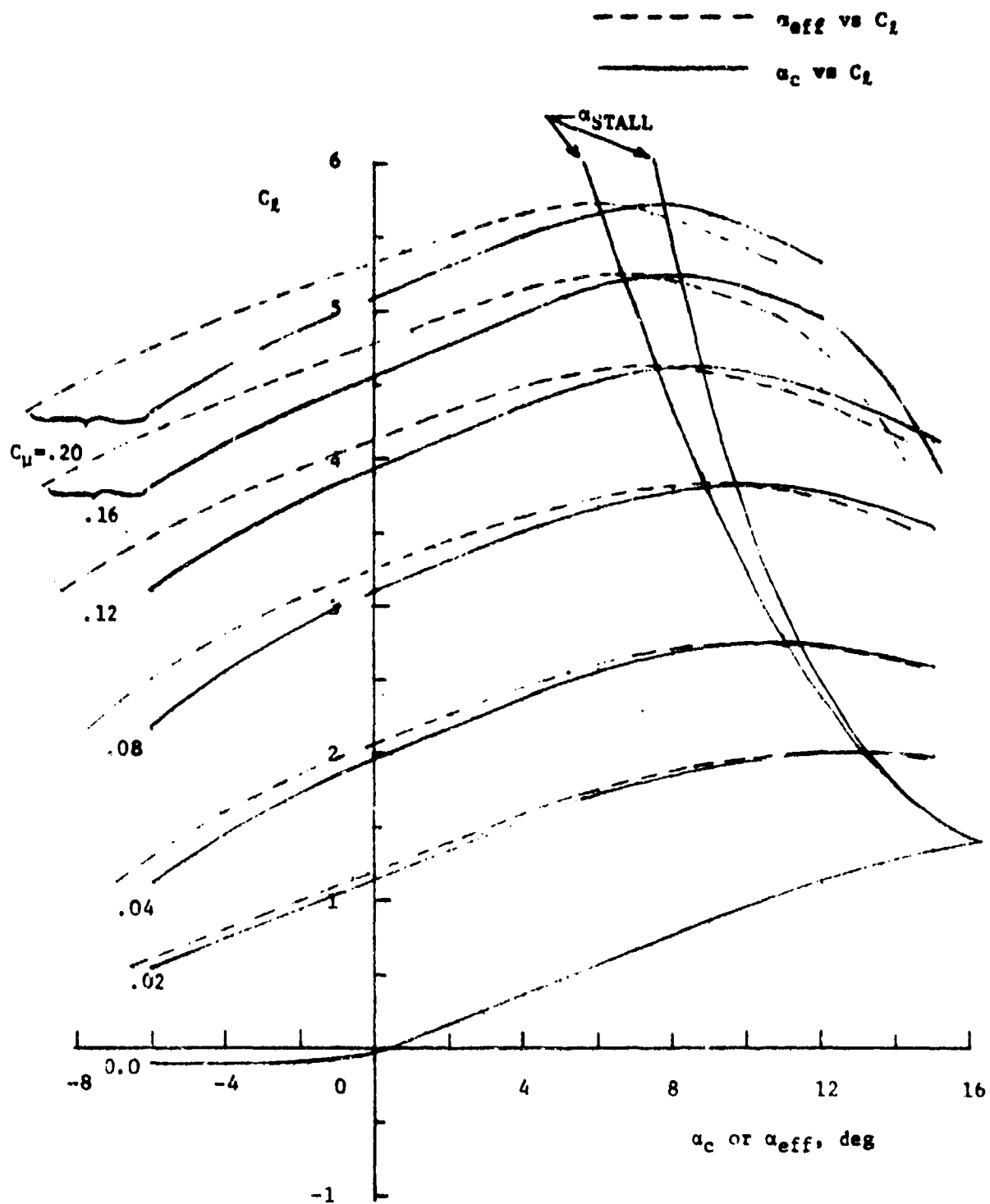


Figure 23 - Continued  
 (d) CCW 244, Reduced T.E.,  $\delta_{LE} = 30^\circ$

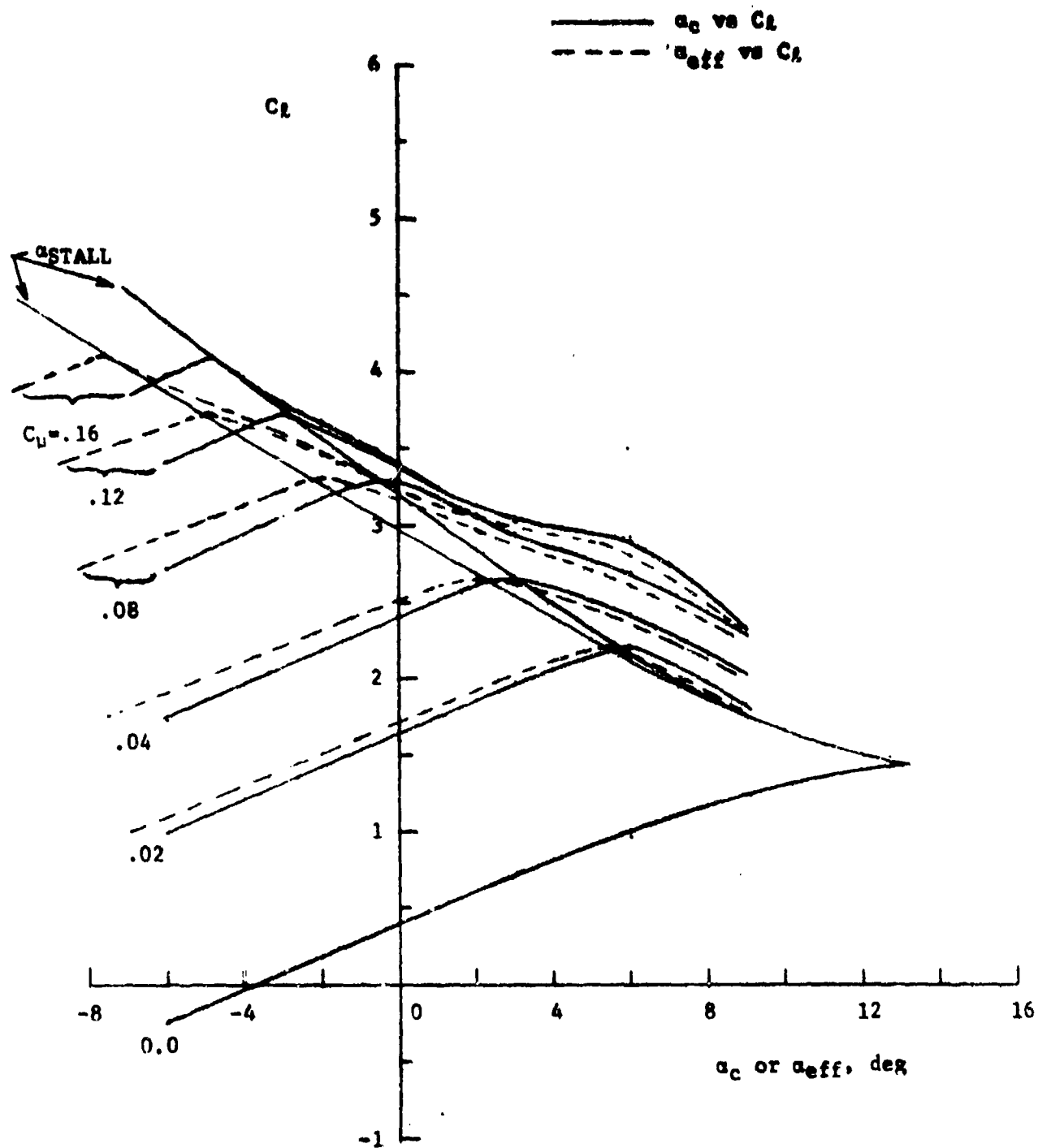


Figure 23 - Concluded  
 (e) CCW 245,  $\delta_f = 180^\circ$ ,  $\delta_{LE} = 0^\circ$



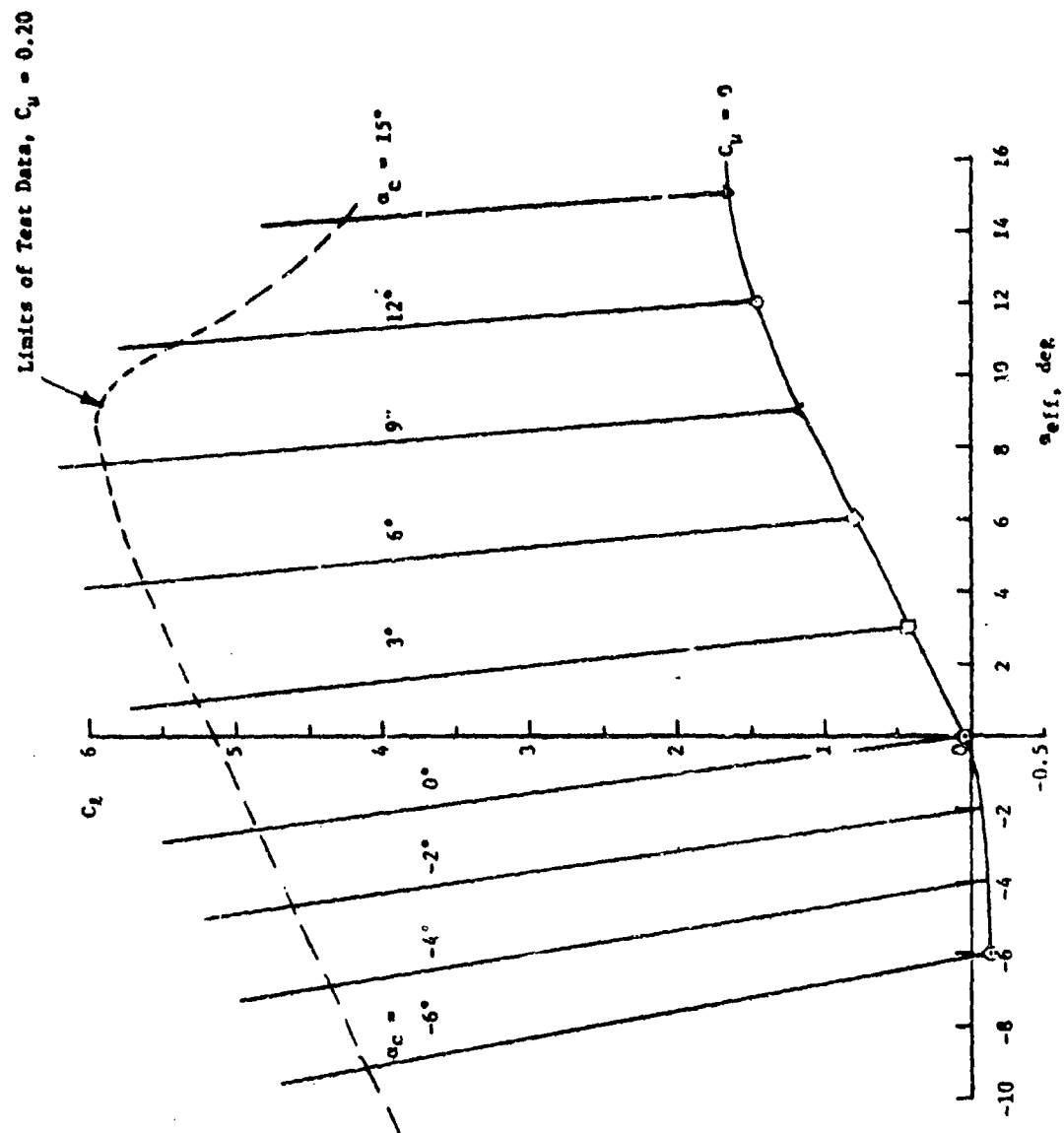


Figure 24 - Effective Incidence Corrections for Configuration CCN 241

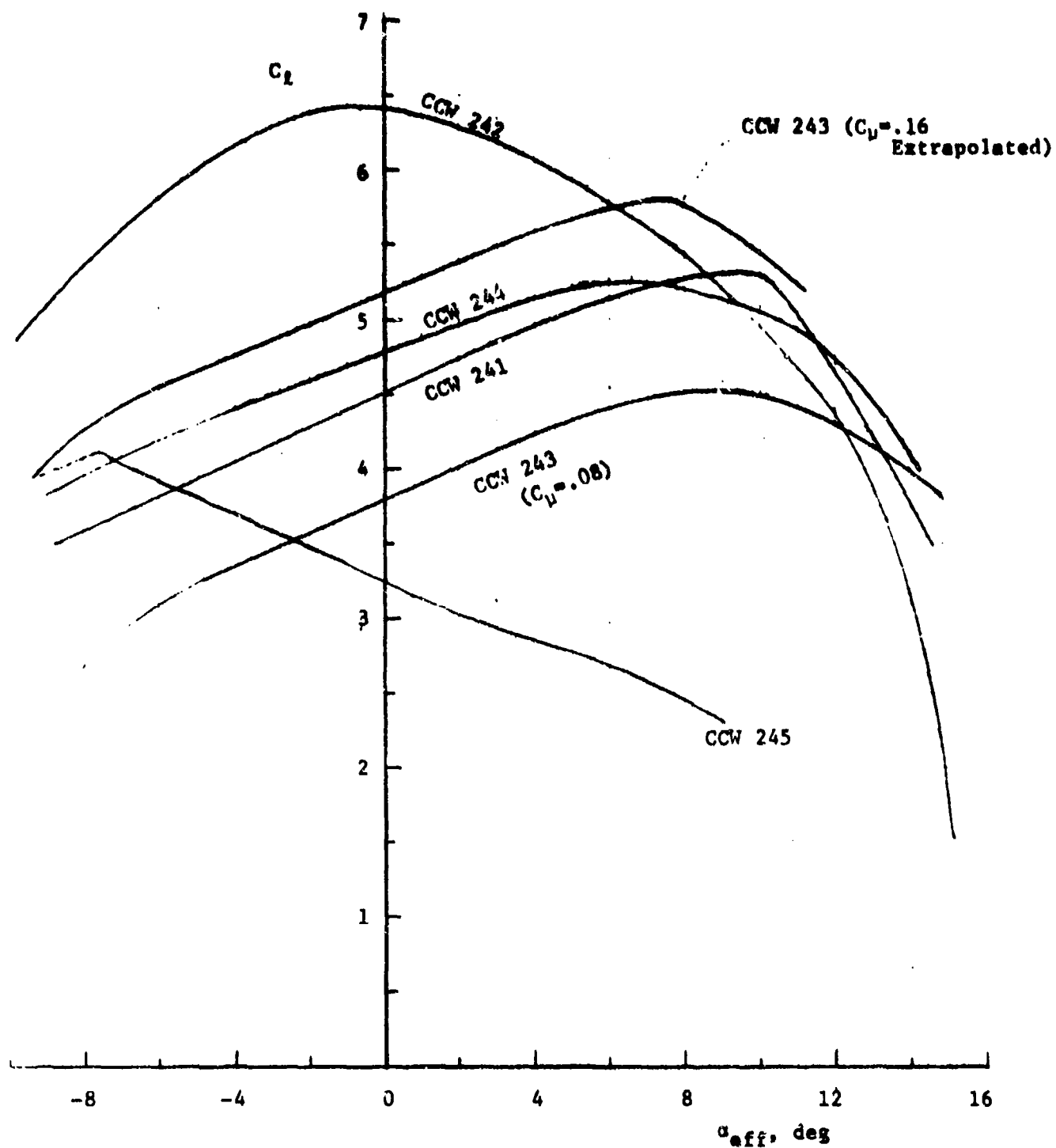


Figure 25 - Lift Curve Comparison for the 64A-212/CCW Airfoils At  
 $C_D = 0.16$ ,  $\alpha_g \leq 15^\circ$ ,  $h = .027''$ ,  $q = 30$  psf

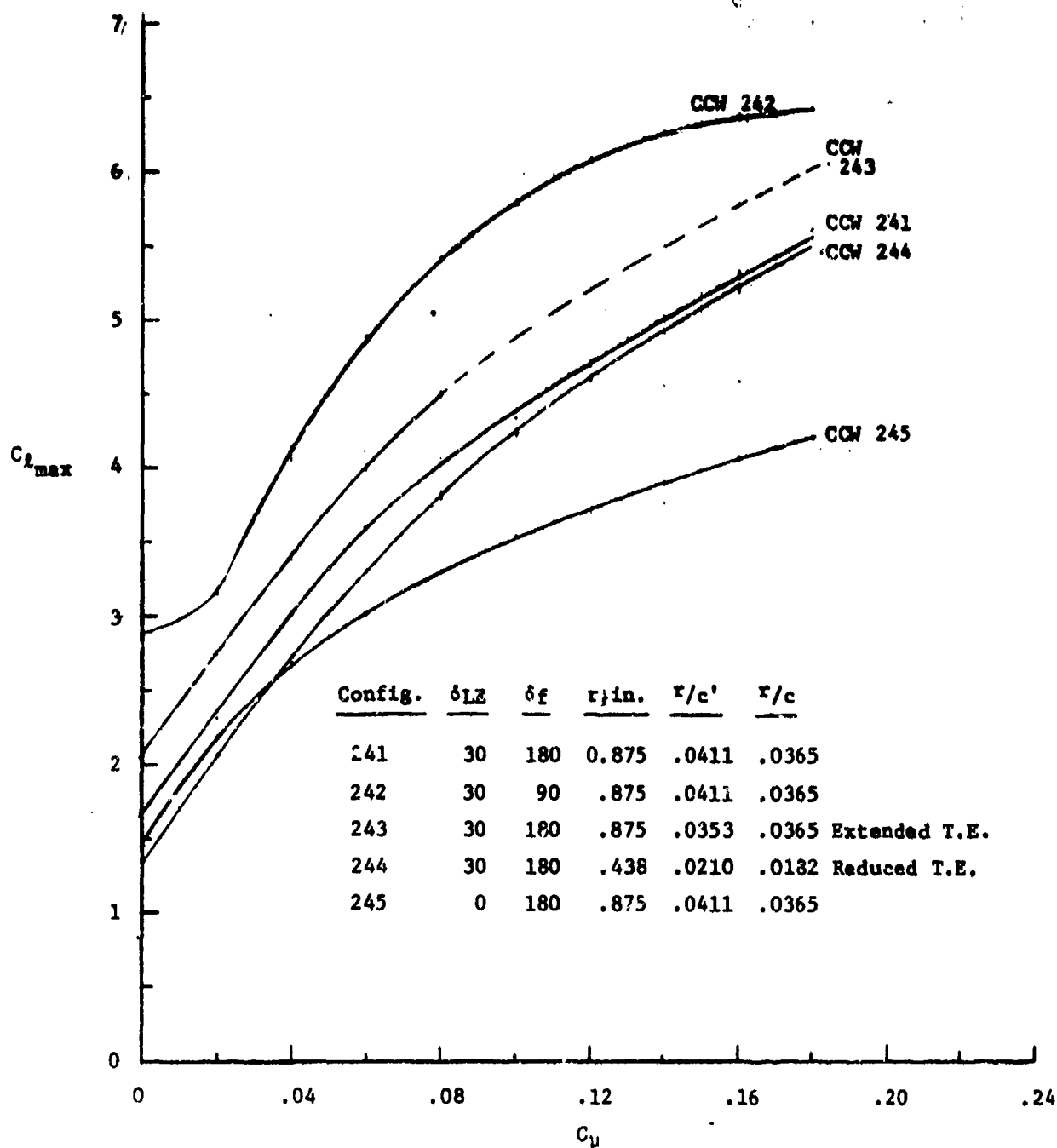


Figure 26 - Maximum Lift Coefficients within Test Limitations for  
5 Configurations of a C.C. Wing on a 2-D NACA  
64A212 Airfoil ( $\alpha_g \leq 15^\circ$ ,  $h = .027''$ ,  $q = 30$  psf)

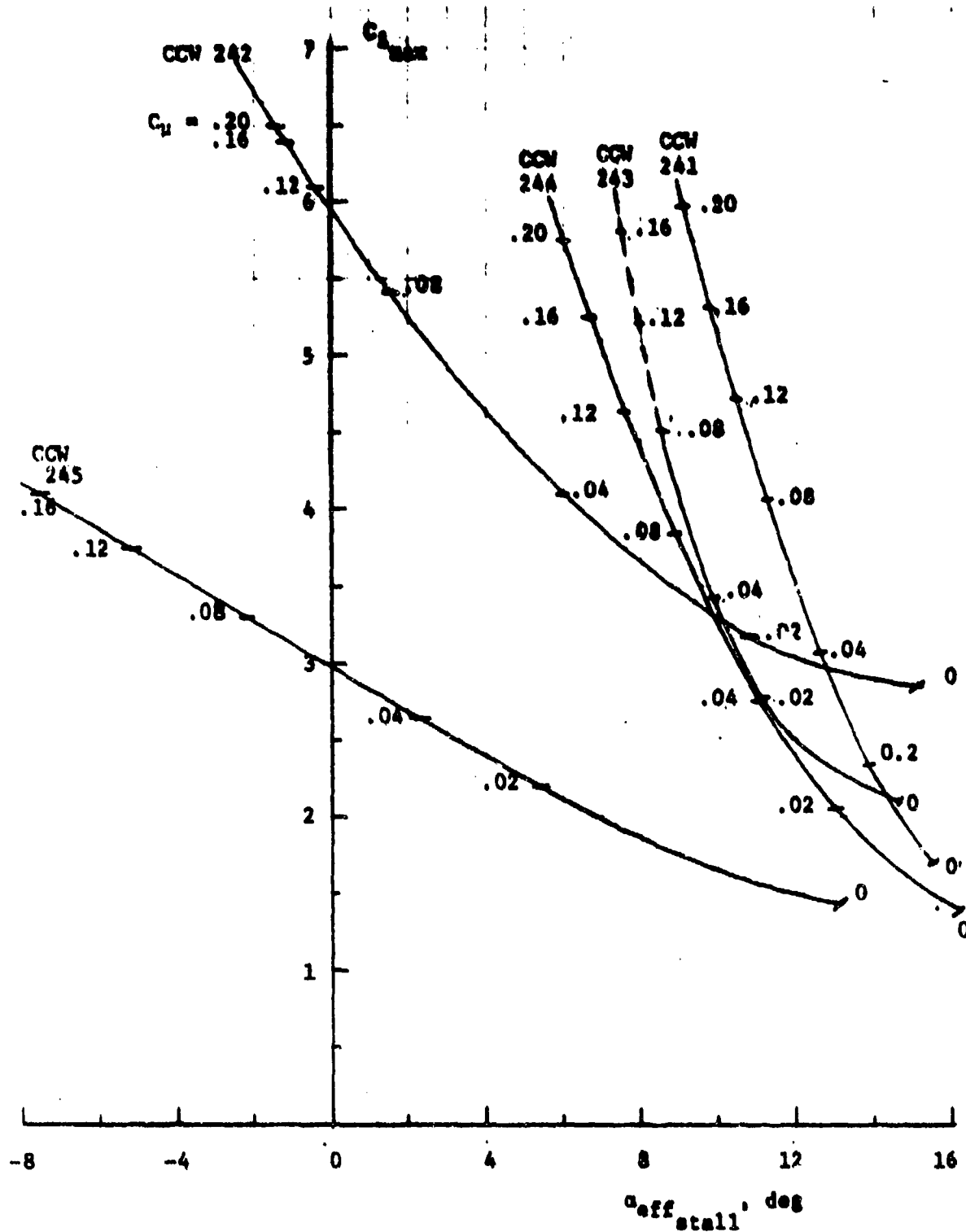


Figure 27 -  $C_{L_{max}}$  and Stall Angles for the 64A-212/CCW Airfoils ( $h = .027''$ ,  $q = 30$  psf)

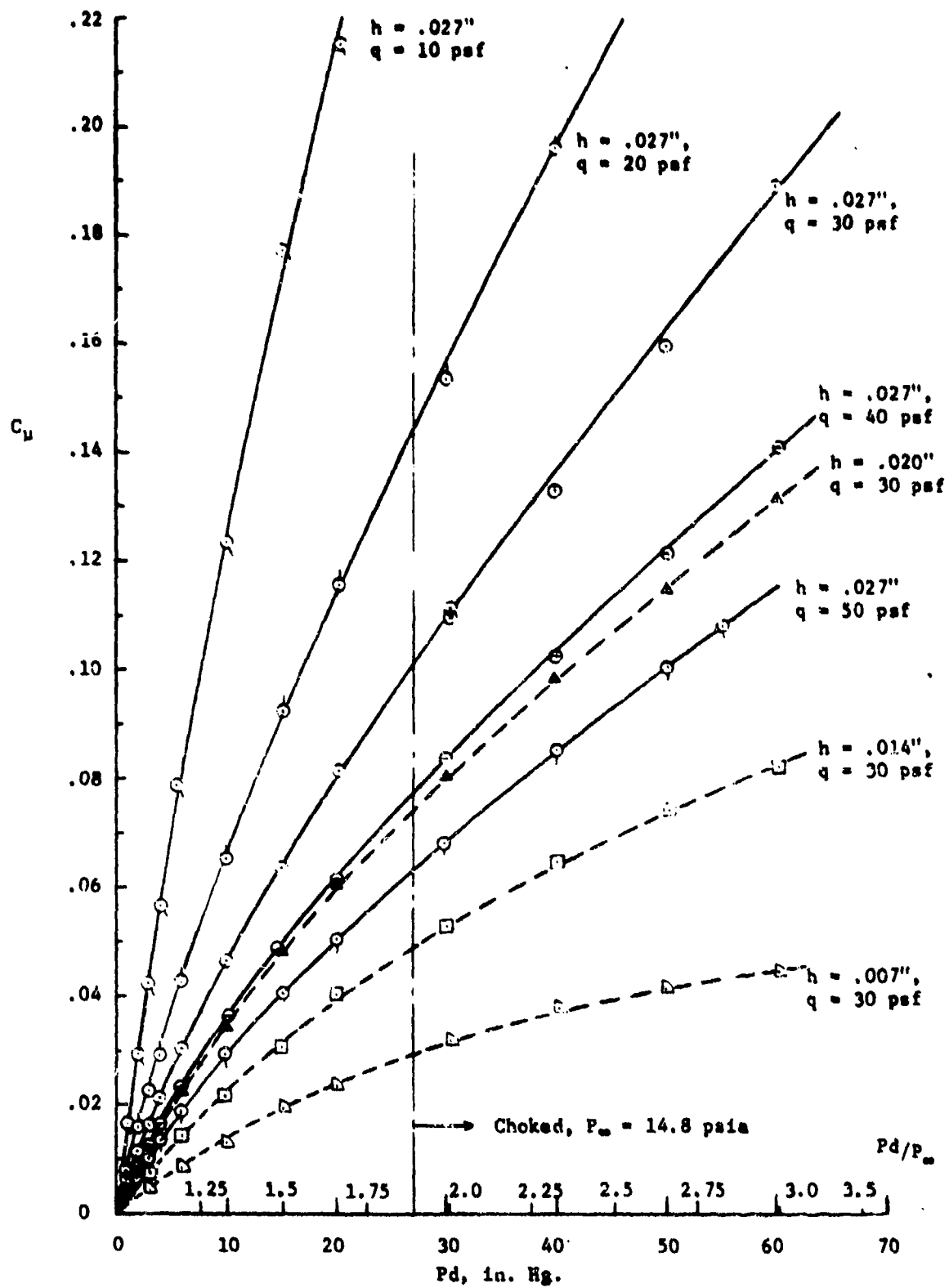


Figure 28 - Slot Height and Dynamic Pressure Effects on  $C_\mu$ ,  
CCW 241,  $\alpha_g = 9^\circ$ ,  $c = 24''$

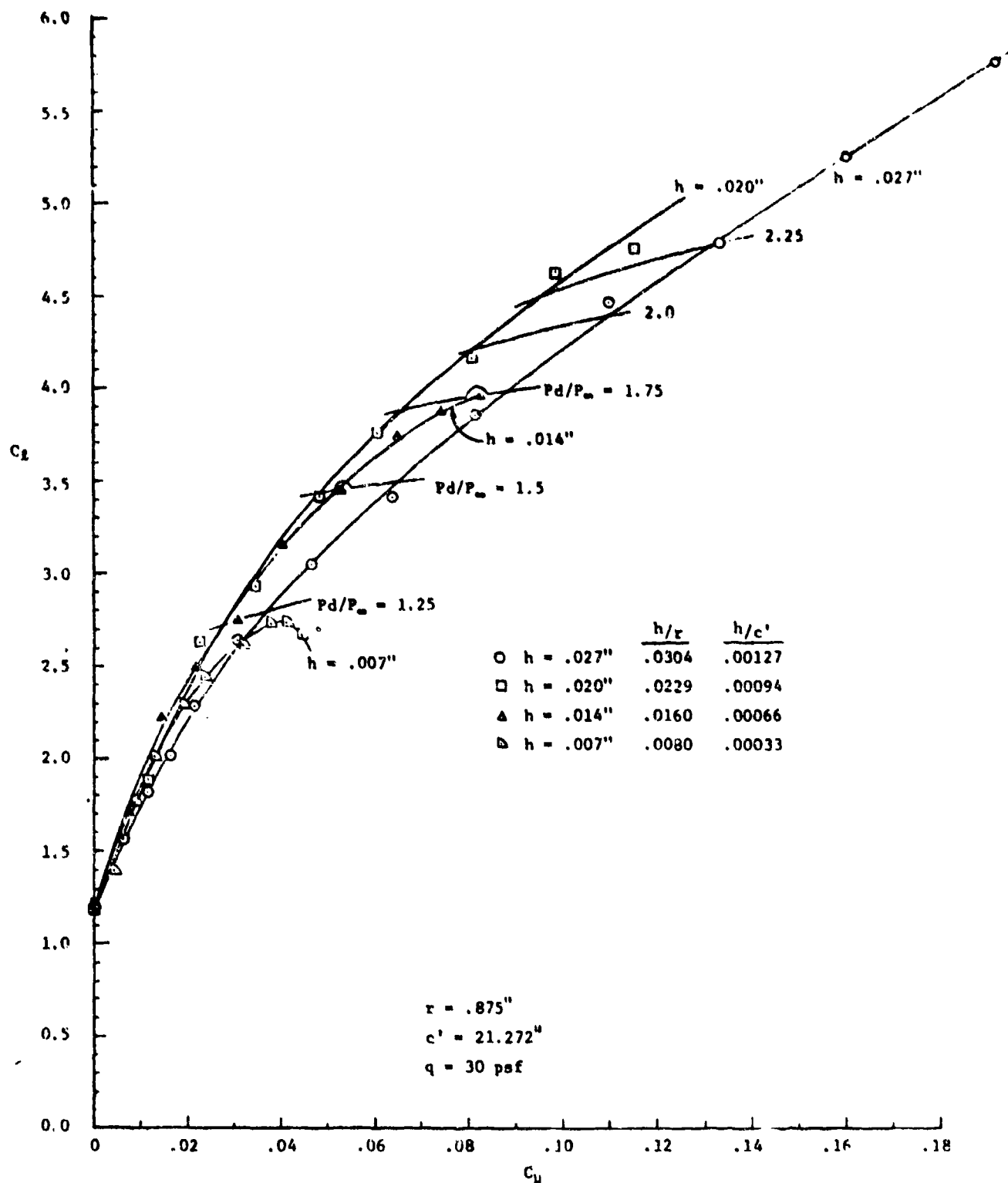


Figure 29 - Slot Height and Pressure Ratio Effects on CCW 241,

$\alpha_c \approx 9^\circ$

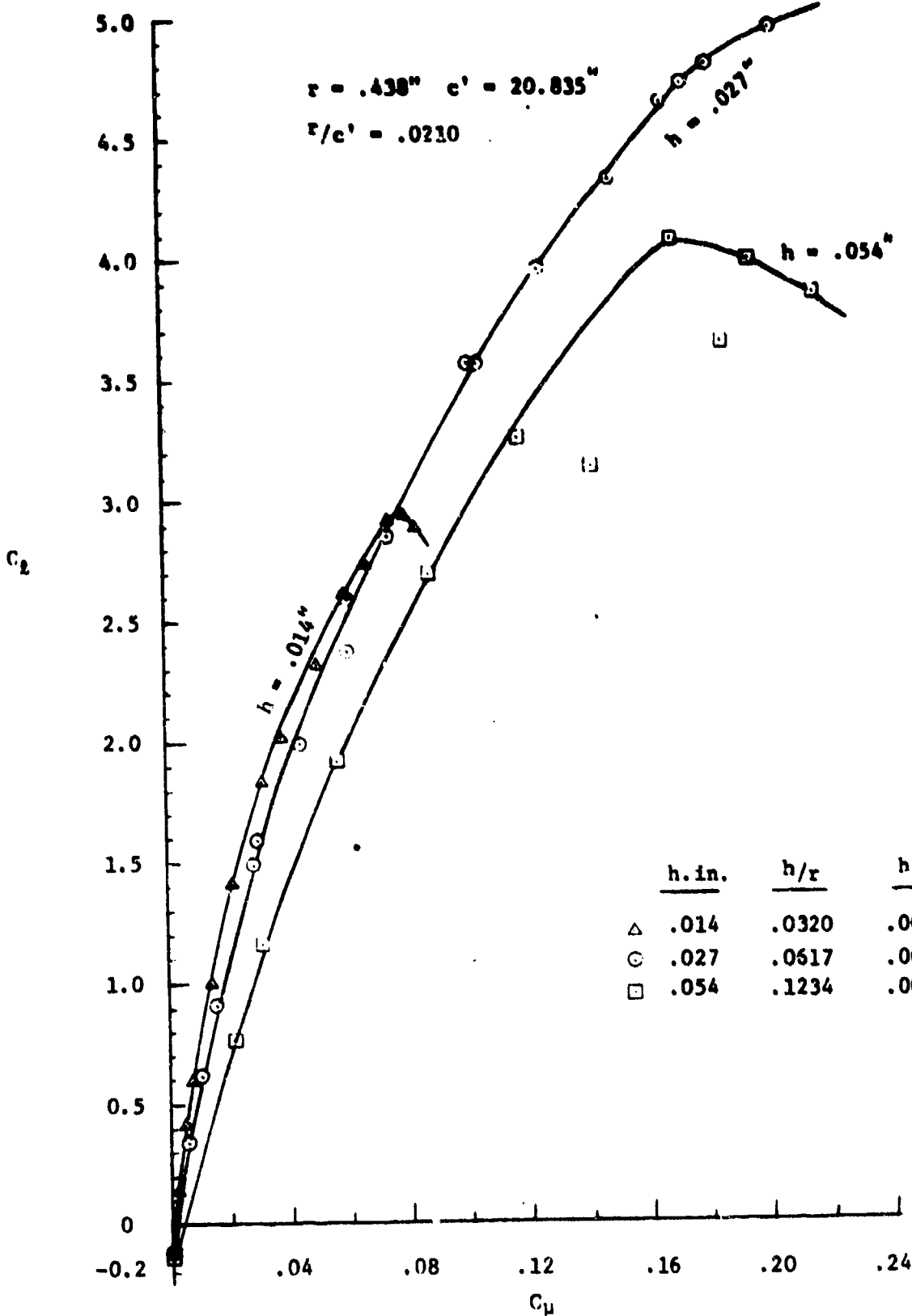


Figure 30 - Slot Height Effects on CCW 244,  $\alpha_c = 0^\circ$

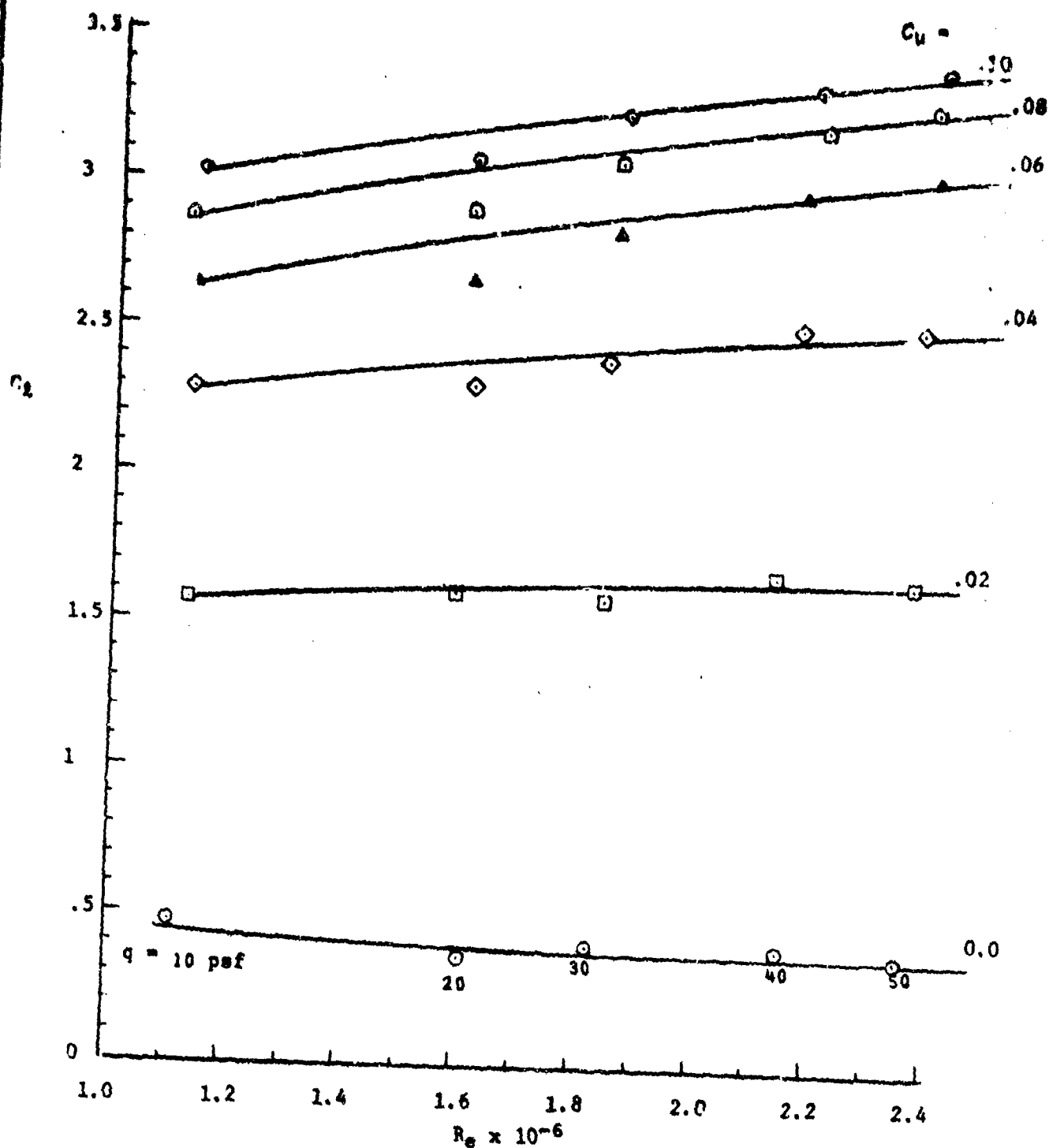


Figure 31 - Effect of Reynolds Number on Lift, CCW 245  
 ( $\delta_{LE} = 0^\circ$ ,  $\delta_f = 180^\circ$ ).  $\alpha_c = 0^\circ$ ,  $h = .027''$



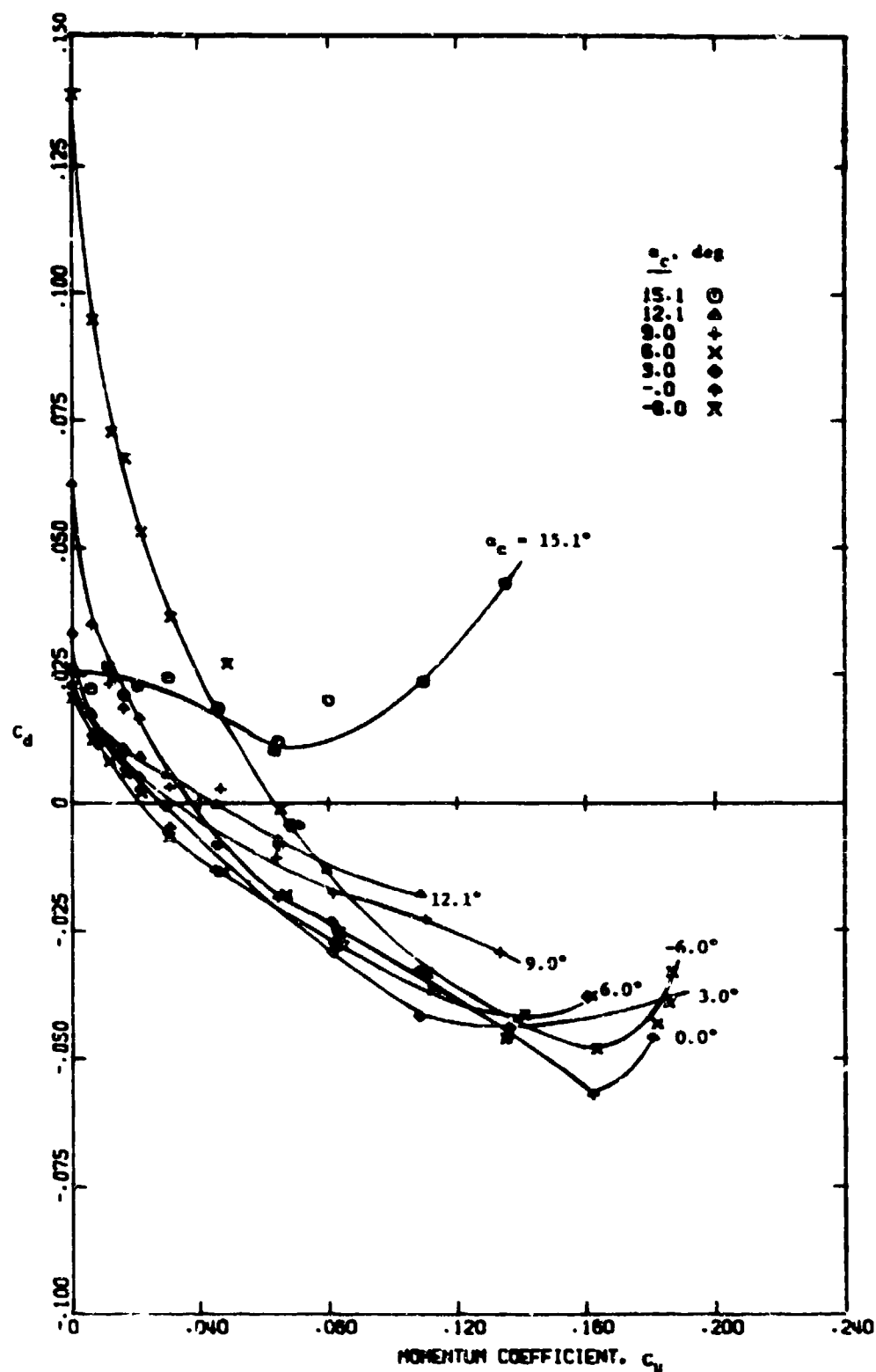


Figure 32 - Drag as a Function of Blowing for NACA 64A-212/CCW Airfoils,  $q = 30$  psf,  $R_e \approx 1.98 \times 10^6$ ,  $h = 0.027''$   
 (a) CCW 241,  $\delta_f = 180^\circ$ ,  $\delta_{LE} = 0^\circ$

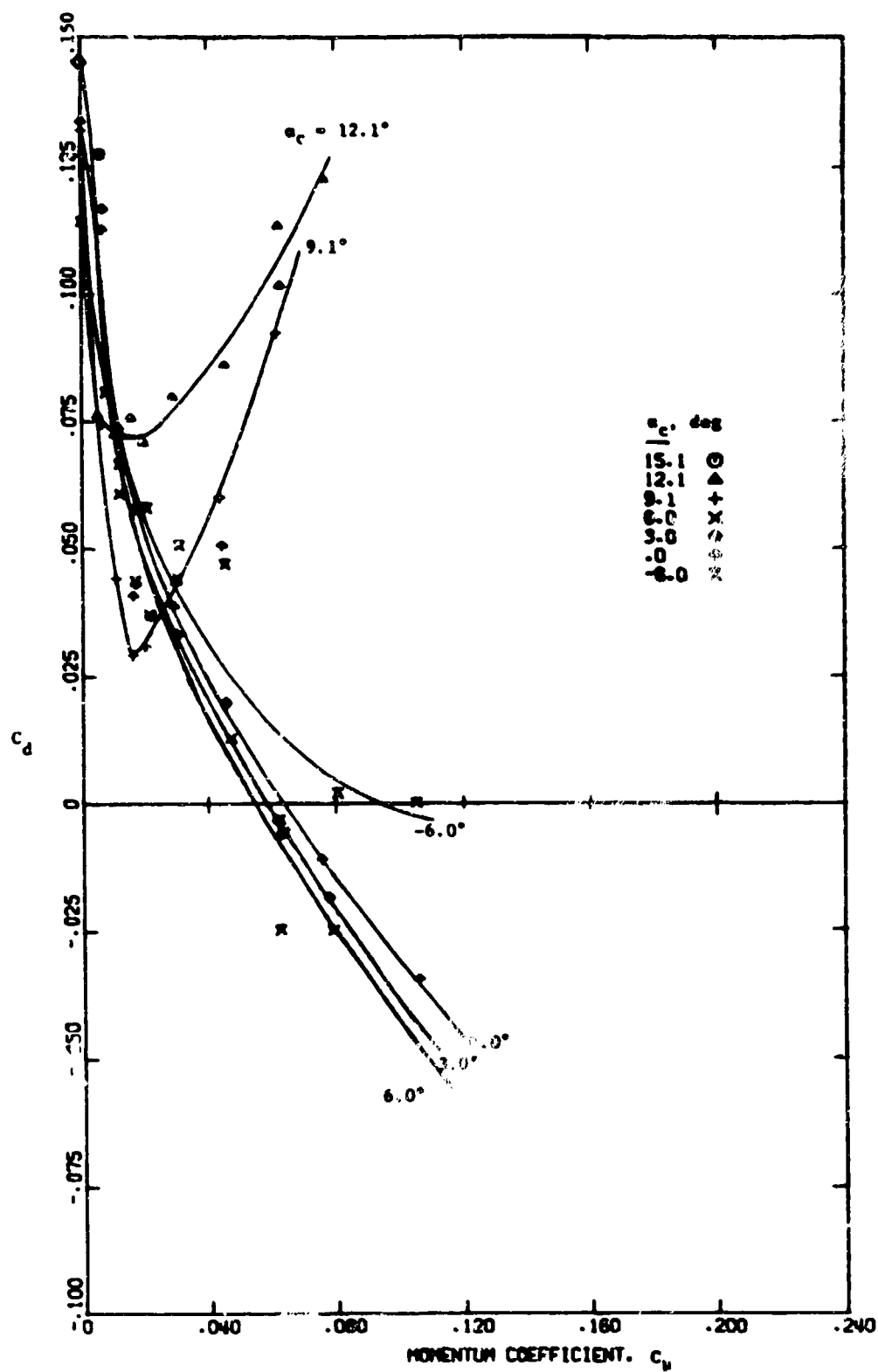


Figure 32 - (Continued)

(b) CCW 242,  $\delta_f = 90^\circ$ ,  $\delta_{LE} = 30^\circ$

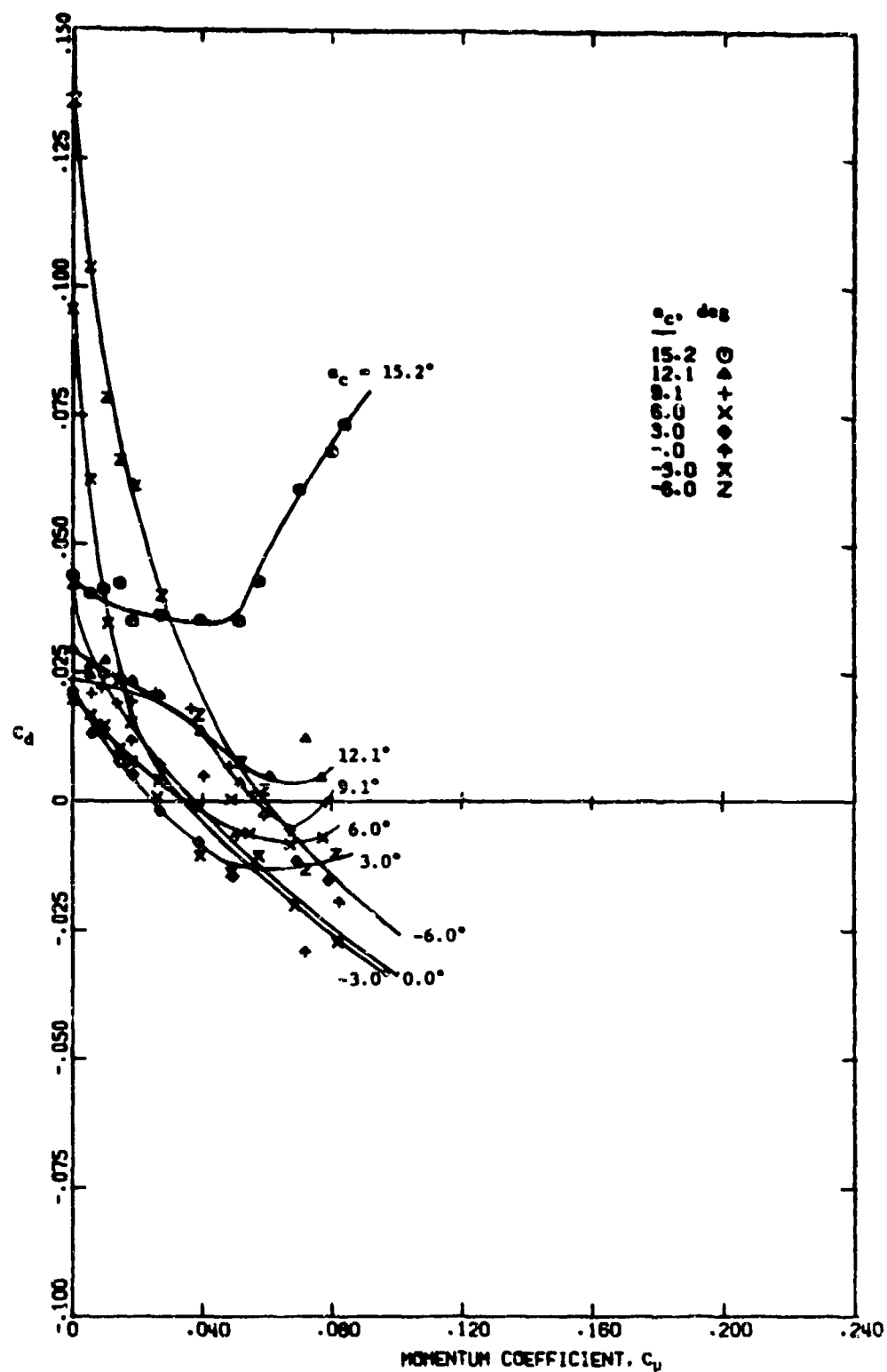


Figure 32 - (Continued)

(c) CCW 243, Extended T.E.,  $\delta_{LE} = 30^\circ$

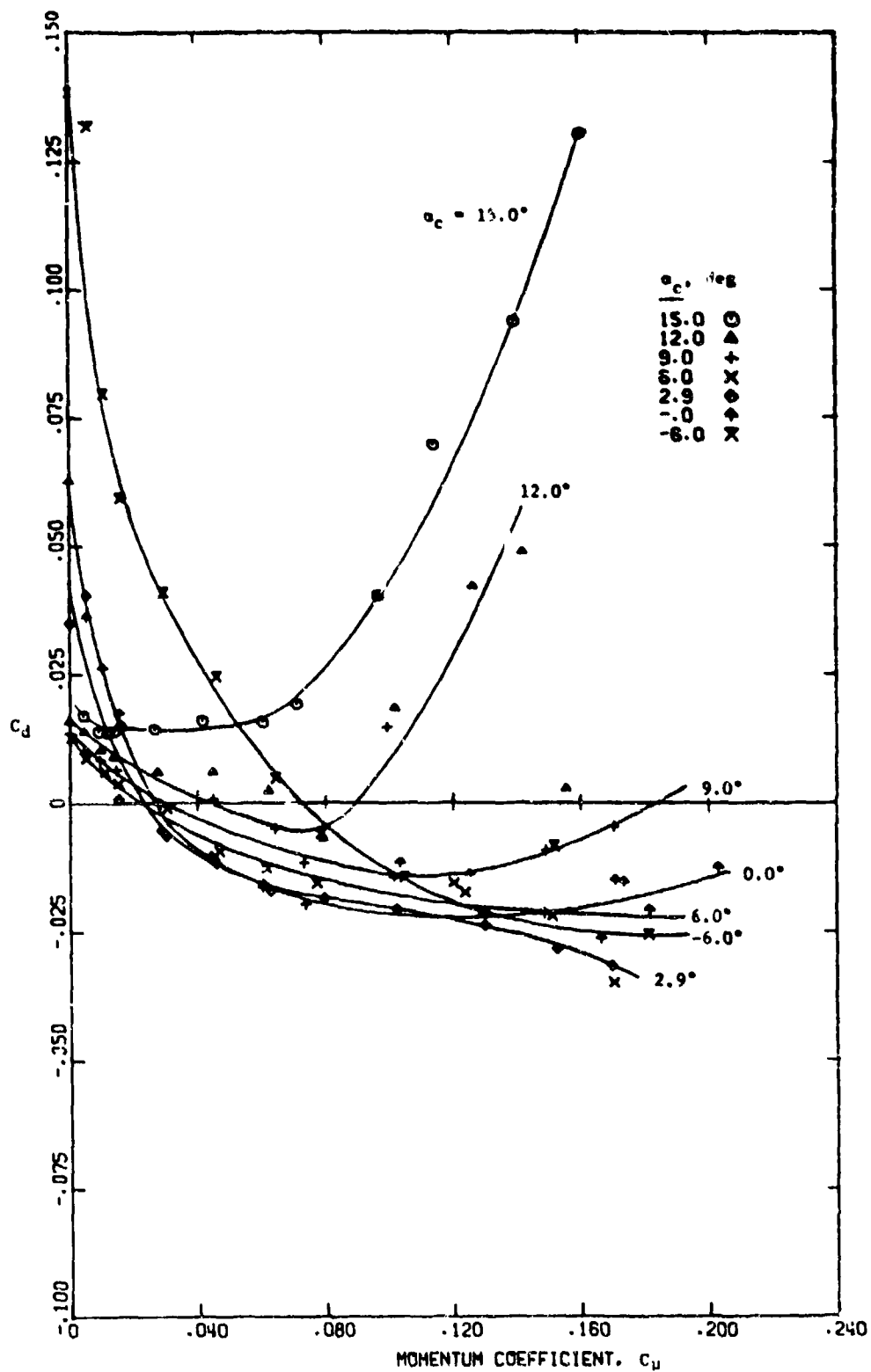


Figure 32 - (Continued)

(d) CCW 244, Reduced T.E.,  $\delta_{LE} = 30^\circ$

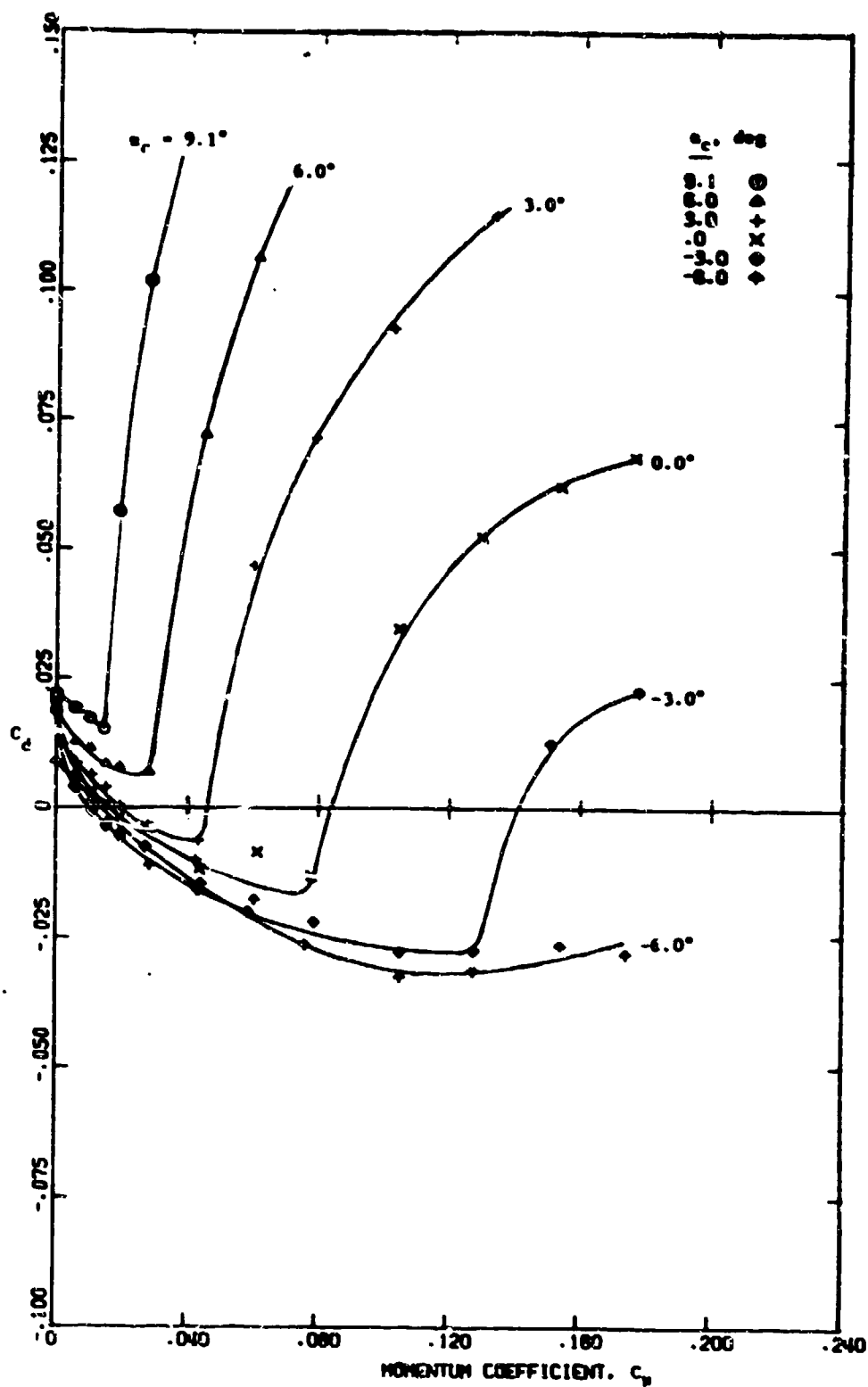


Figure 32 - (Concluded)

(e) CCW 245,  $\delta_f = 180^\circ$ ,  $\delta_{LE} = 0^\circ$

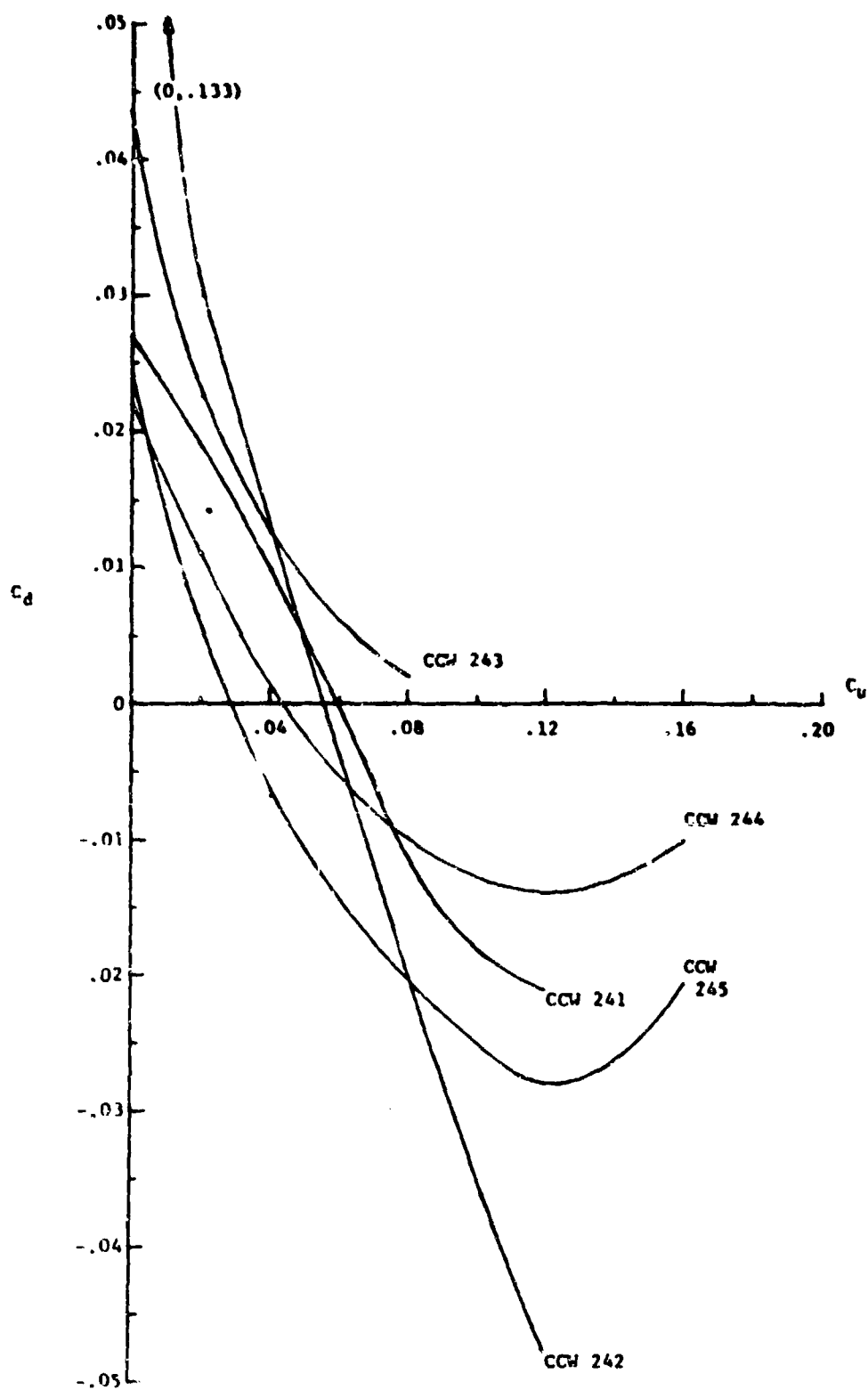


Figure 33 - Drag Coefficient at  $C_{l_{max}}$  within Test Limits for NACA 64A-212/CCW Airfoils,  
 $\alpha_g \leq 15^\circ$ ,  $h = 0.027"$ ,  $q = 30$  psf

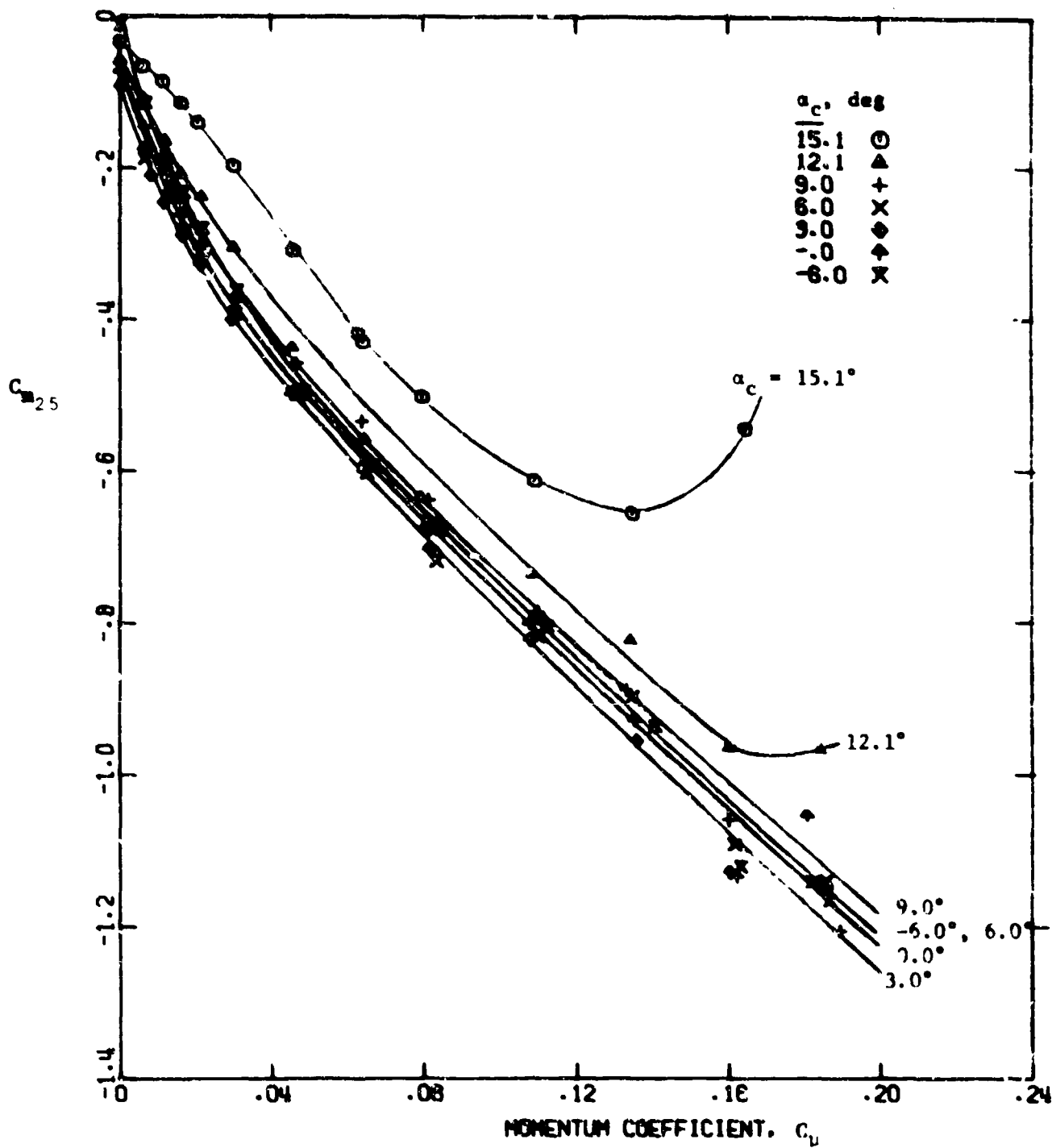


Figure 34 - Pitching Moment Variation with Blowing for CCW 241,  
 $h = 0.027''$ ,  $q = 30$  psf

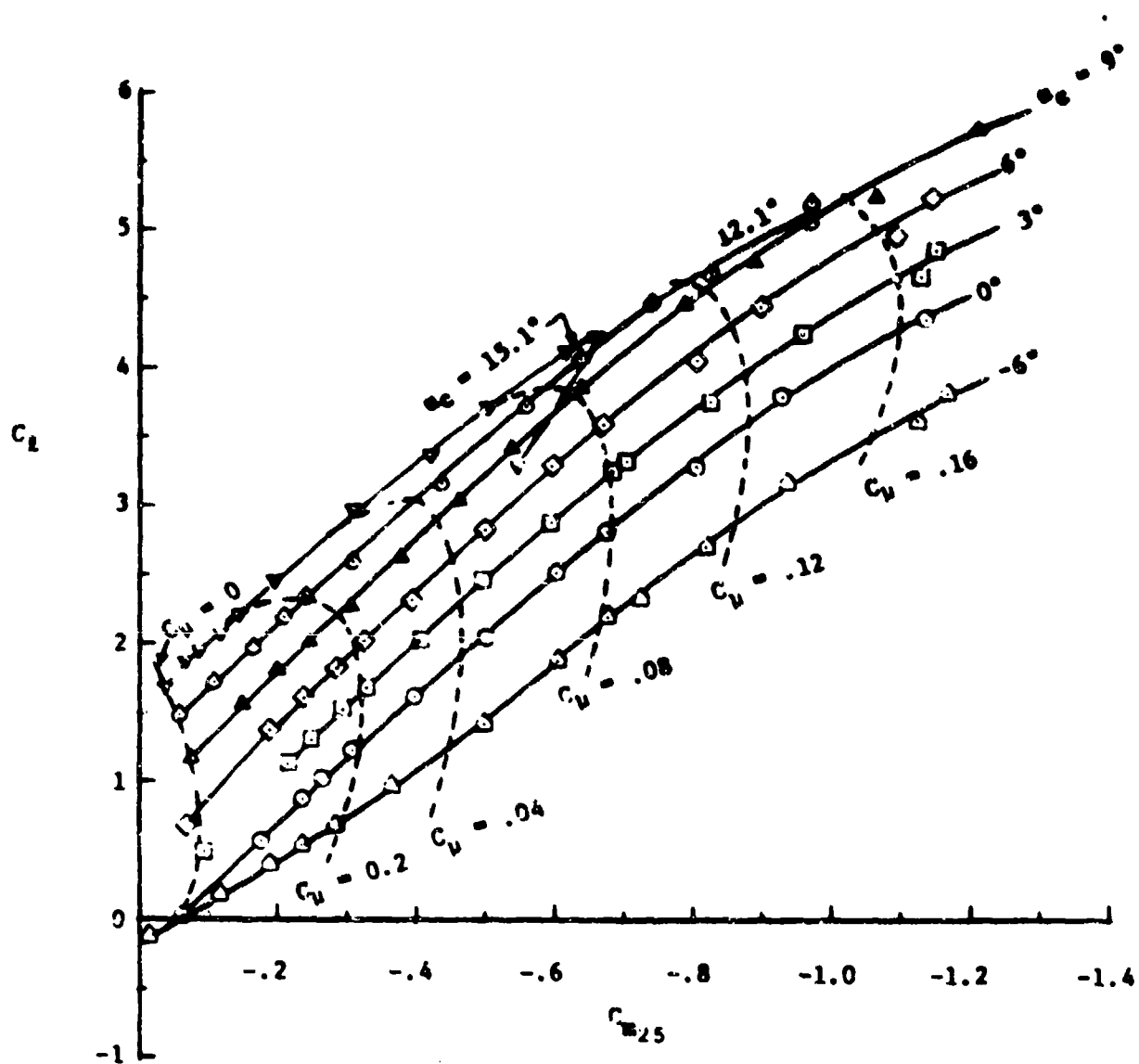


Figure 35 - Pitching Moment as a Function of Lift, Incidence and  $C_d$   
for NACA 64A-212/CCW Airfoils ( $h = .027''$ ,  $q = 30$  psf)

(a) CCW 241,  $\delta_f = 180^\circ$ ,  $\delta_{LE} = 30^\circ$



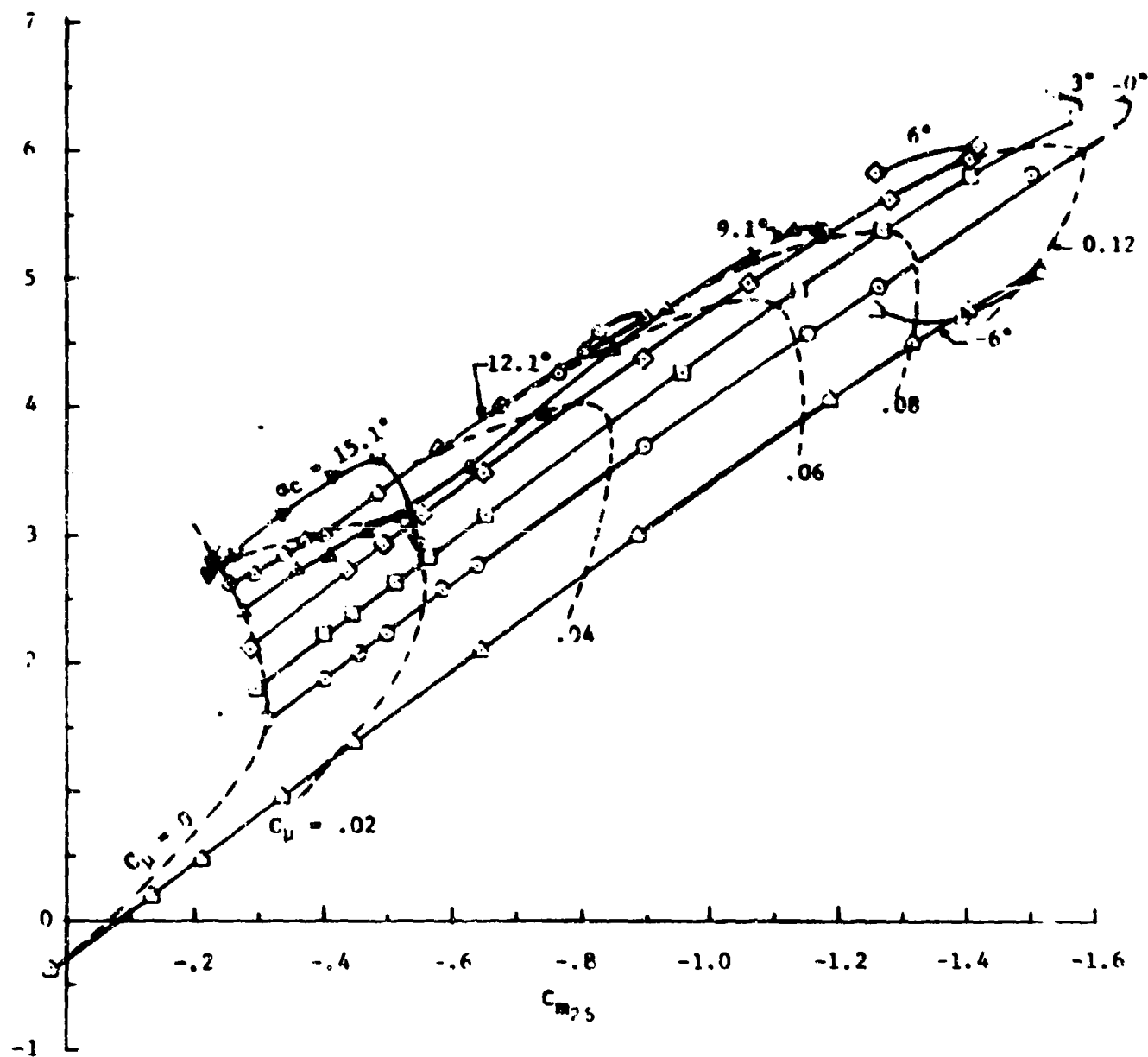


Figure 35 - Continued  
 (b) CCW 242,  $\delta_f = 90^\circ$ ,  $\delta_{LE} = 30^\circ$

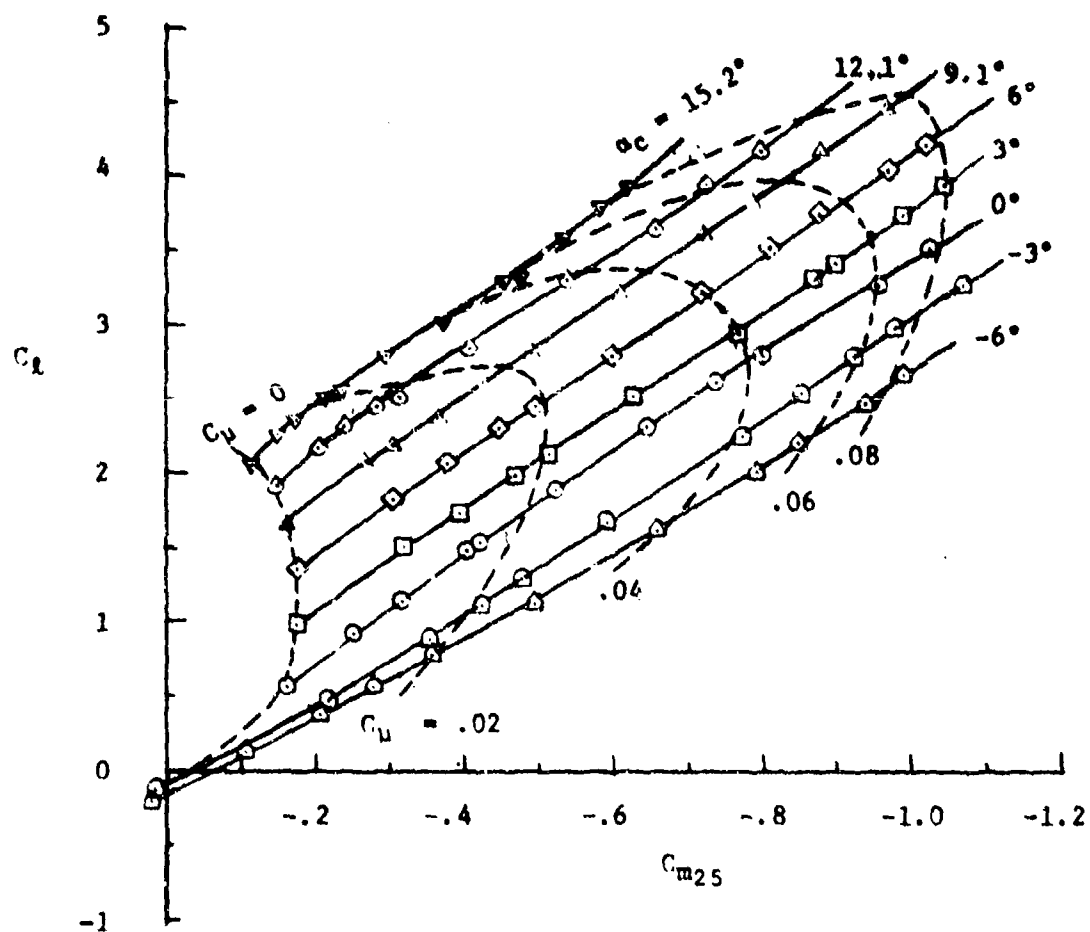


Figure 35 - Continued  
(c) CCW 243, Extended T.E.,  $\delta_{LE} = 30^\circ$

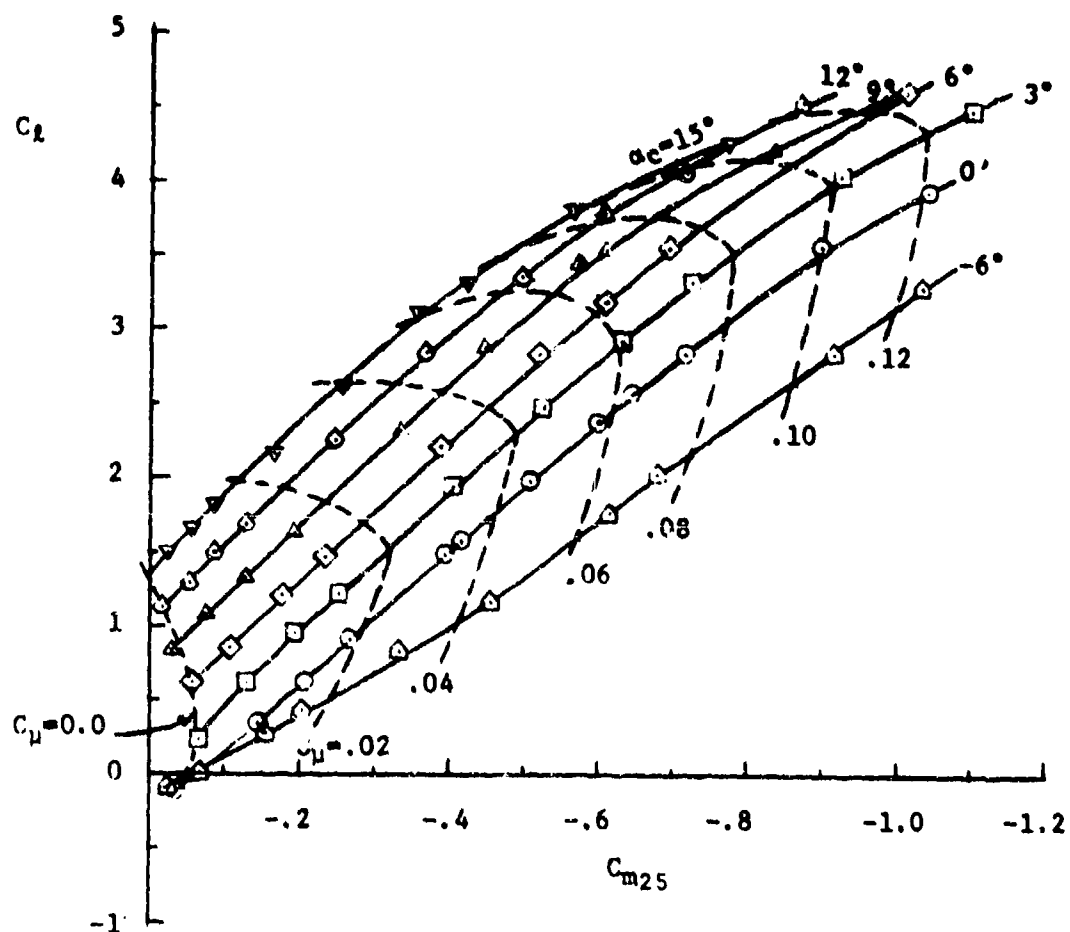


Figure 35 - Continued  
 (d) CCW 244, Reduced T.E.,  $\delta_{LE} = 30^\circ$

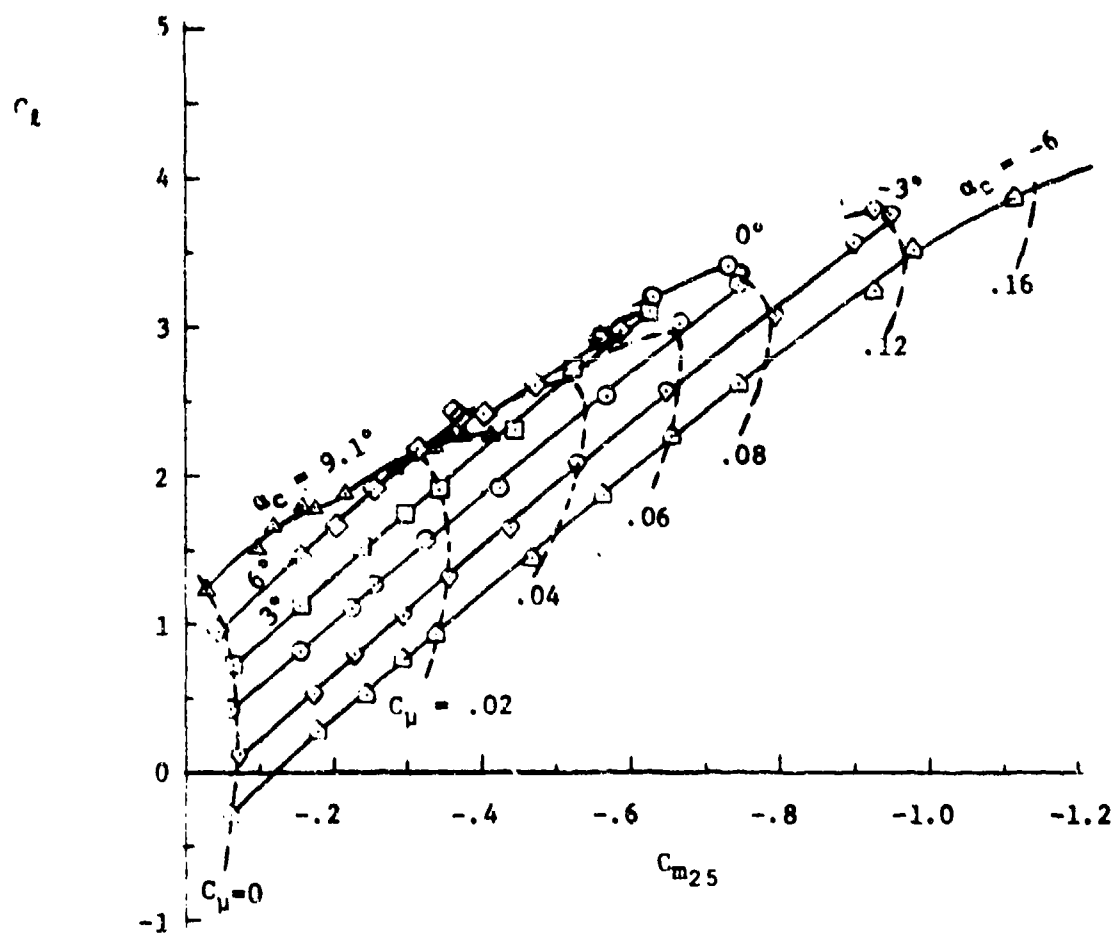


Figure 35 - Concluded  
(e) CCW 245,  $\delta_f = 180^\circ$ ,  $\delta_{LE} = 0^\circ$

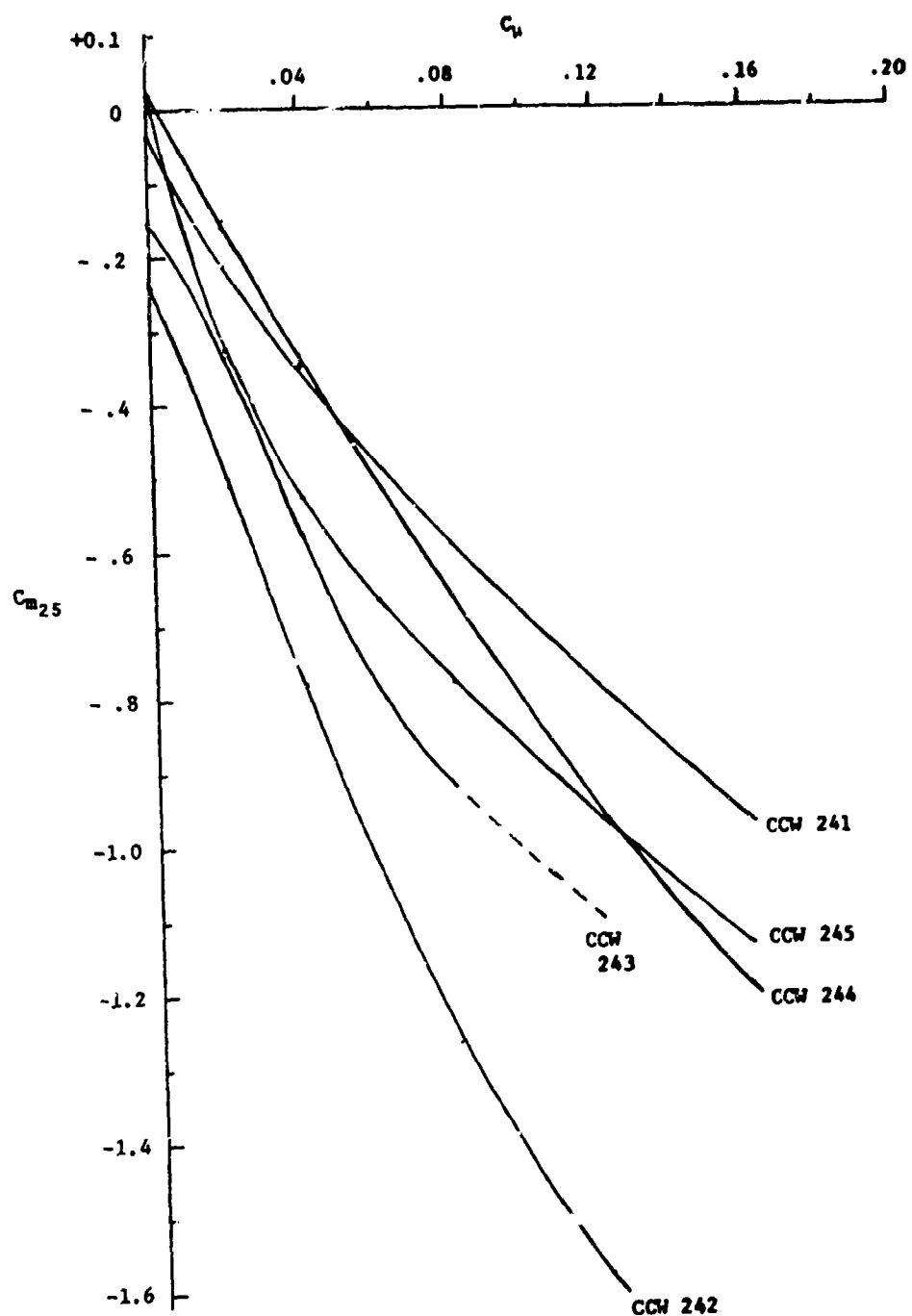


Figure 36 - Pitching Moment Coefficient at  $C_{l_{max}}$  within Test Limits  
for NACA 64A-212/CCW Airfoils,  $\alpha_g \leq 15^\circ$ ,  
 $h = 0.027''$ ,  $q = 30$  psf

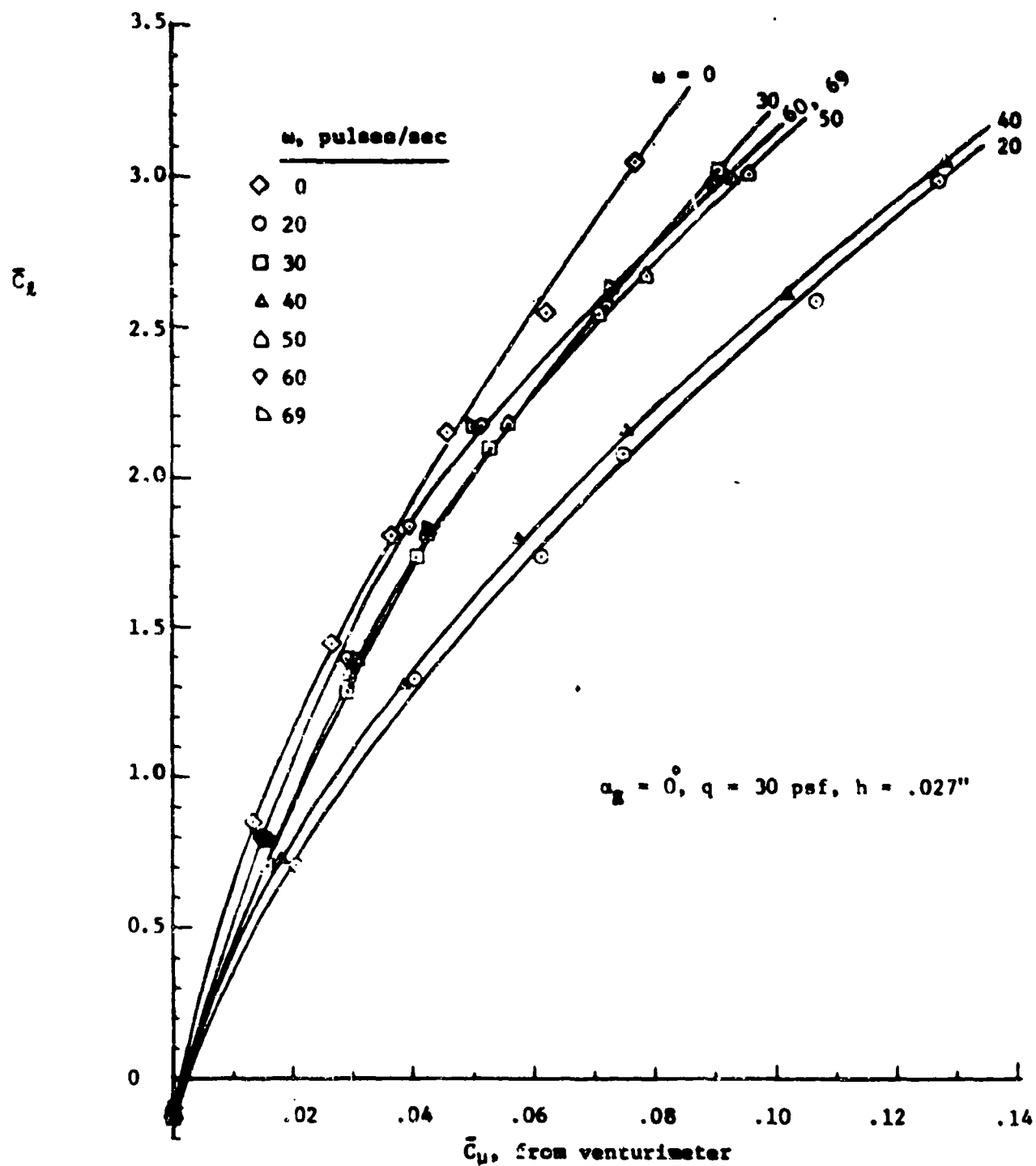


Figure 37 - Mean Lift and Momentum Coefficients as Functions of Pulsing Rate, CCW 244

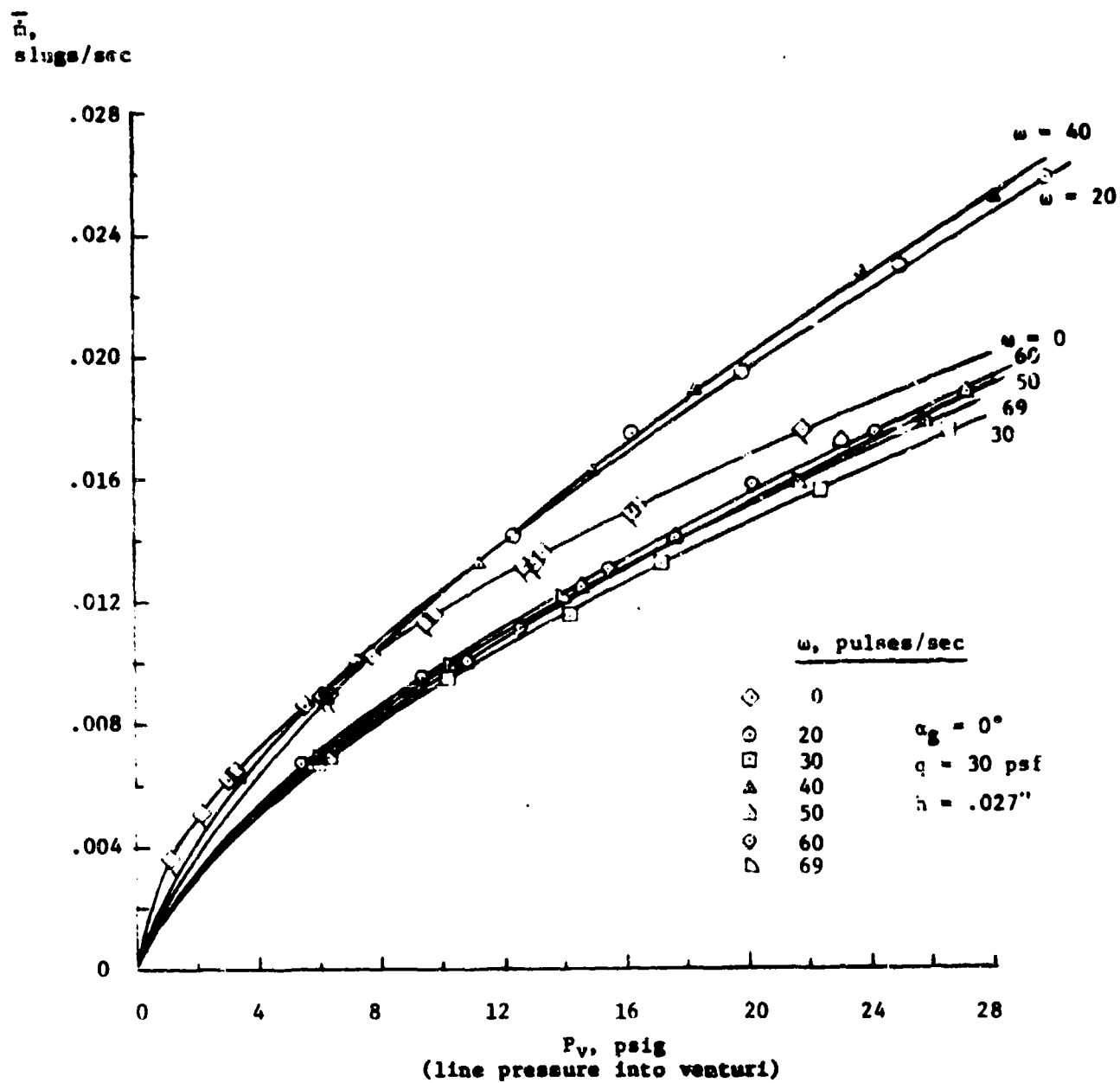


Figure 38 - Mean Mass Flow Measured by the Venturimeter, CCW 244

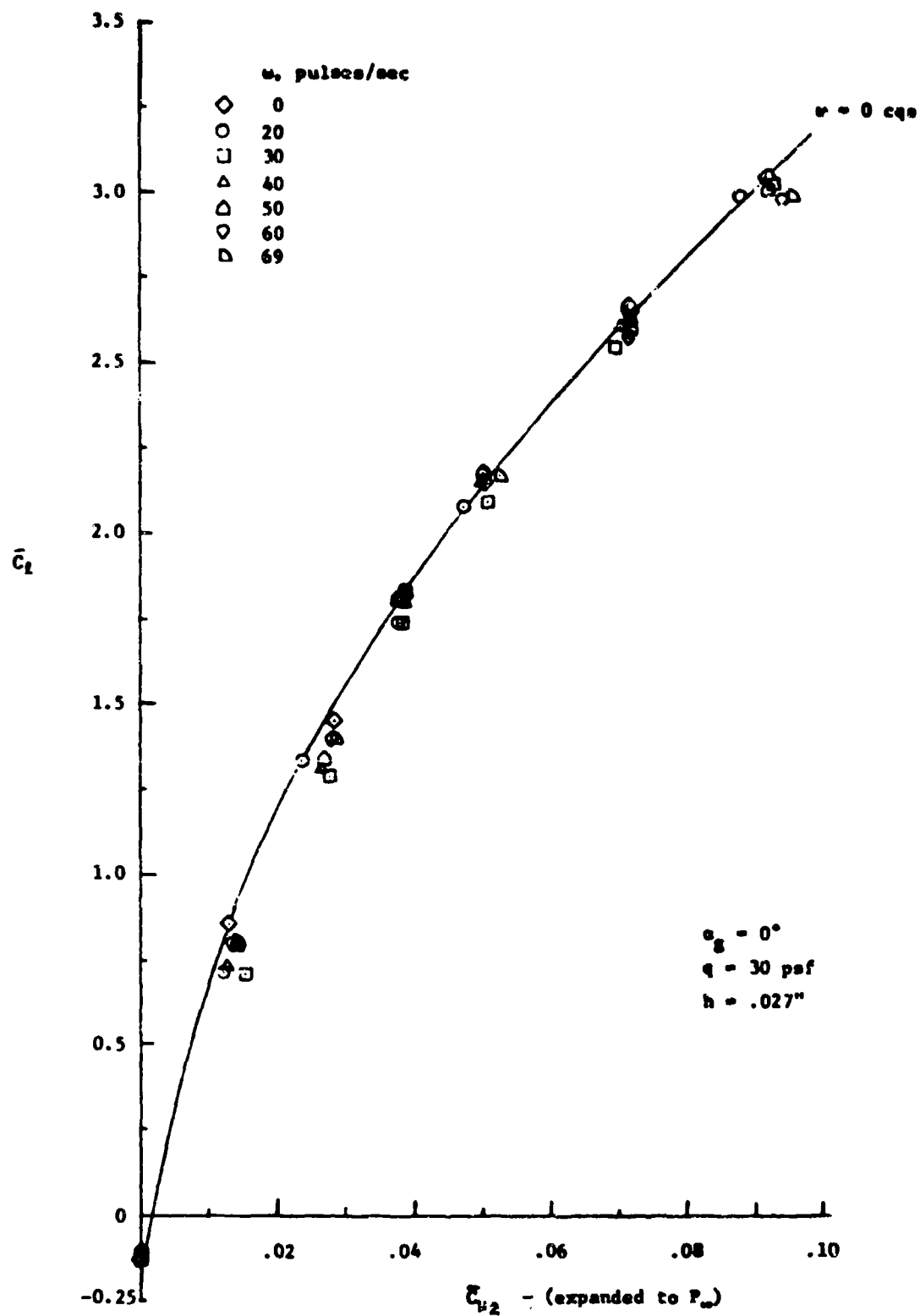


Figure 39 - Corrected Mean Lift and Momentum Coefficients as Functions of Pulse Rate, CCW 244



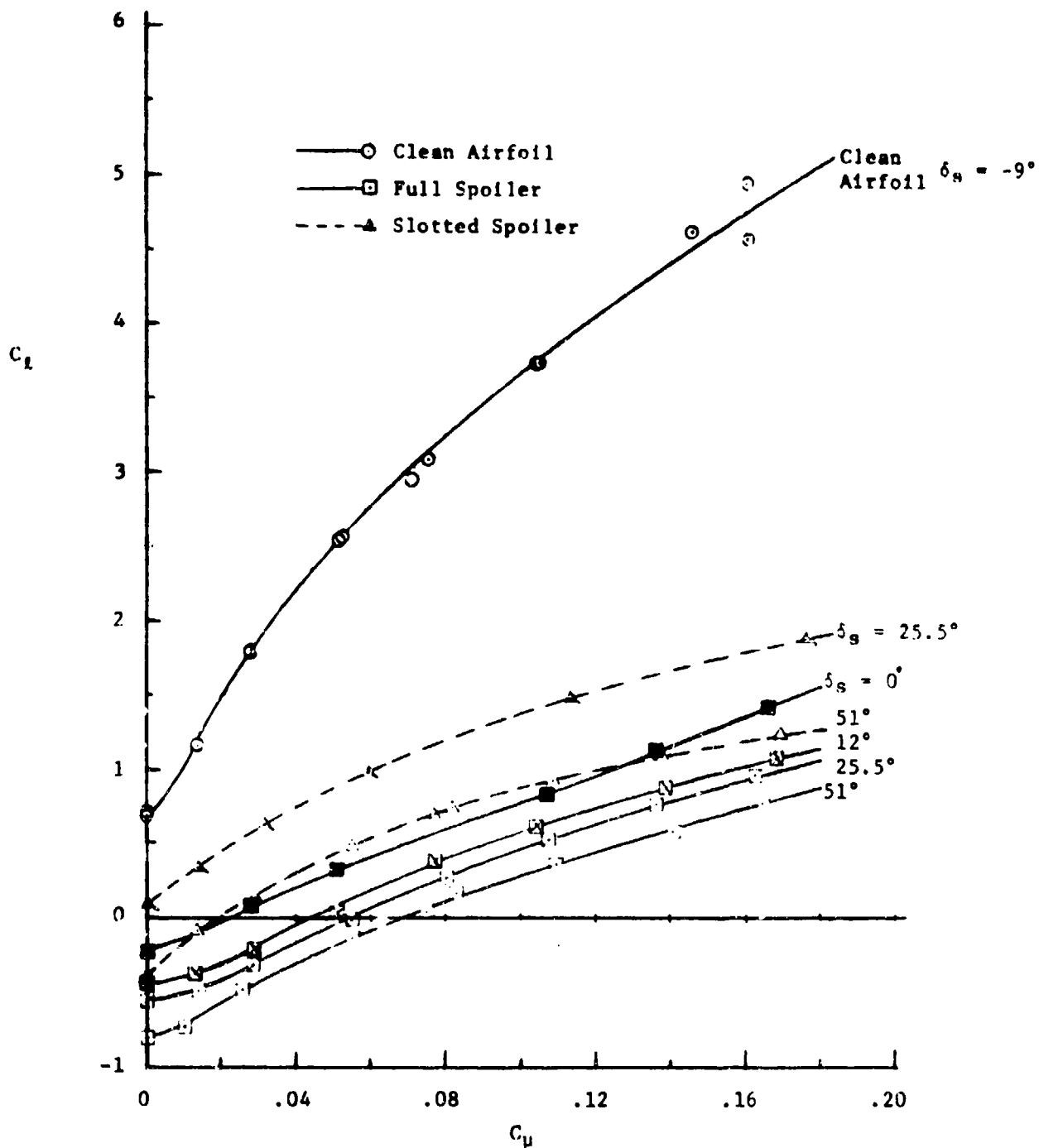
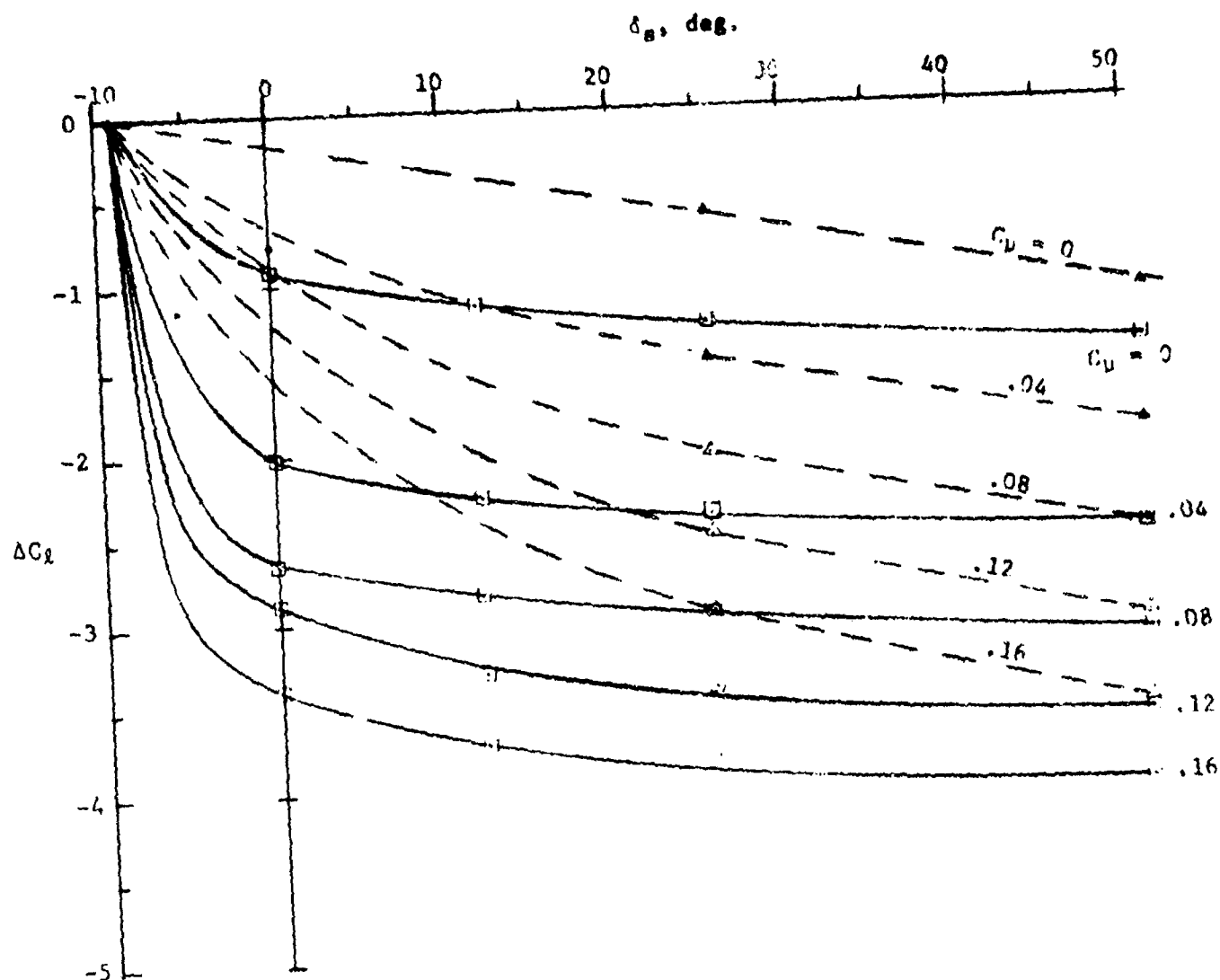


Figure 40 - Effect of Spoiler Deflection on Lift of Elliptical C.C. Airfoil ( $\alpha_g = 0^\circ$ ,  $q = 20$  psf,  $h = .009''$ )



$\Delta C_L = C_L - C_{L_{clean}}$   
 $\alpha_g = 0^\circ, q = 20 \text{ psf}, h = .009''$   
 —□— Full Spoiler  
 ---Δ--- Slotted Spoiler

Figure 41 - Lift Loss as a Function of Spoiler Deflection

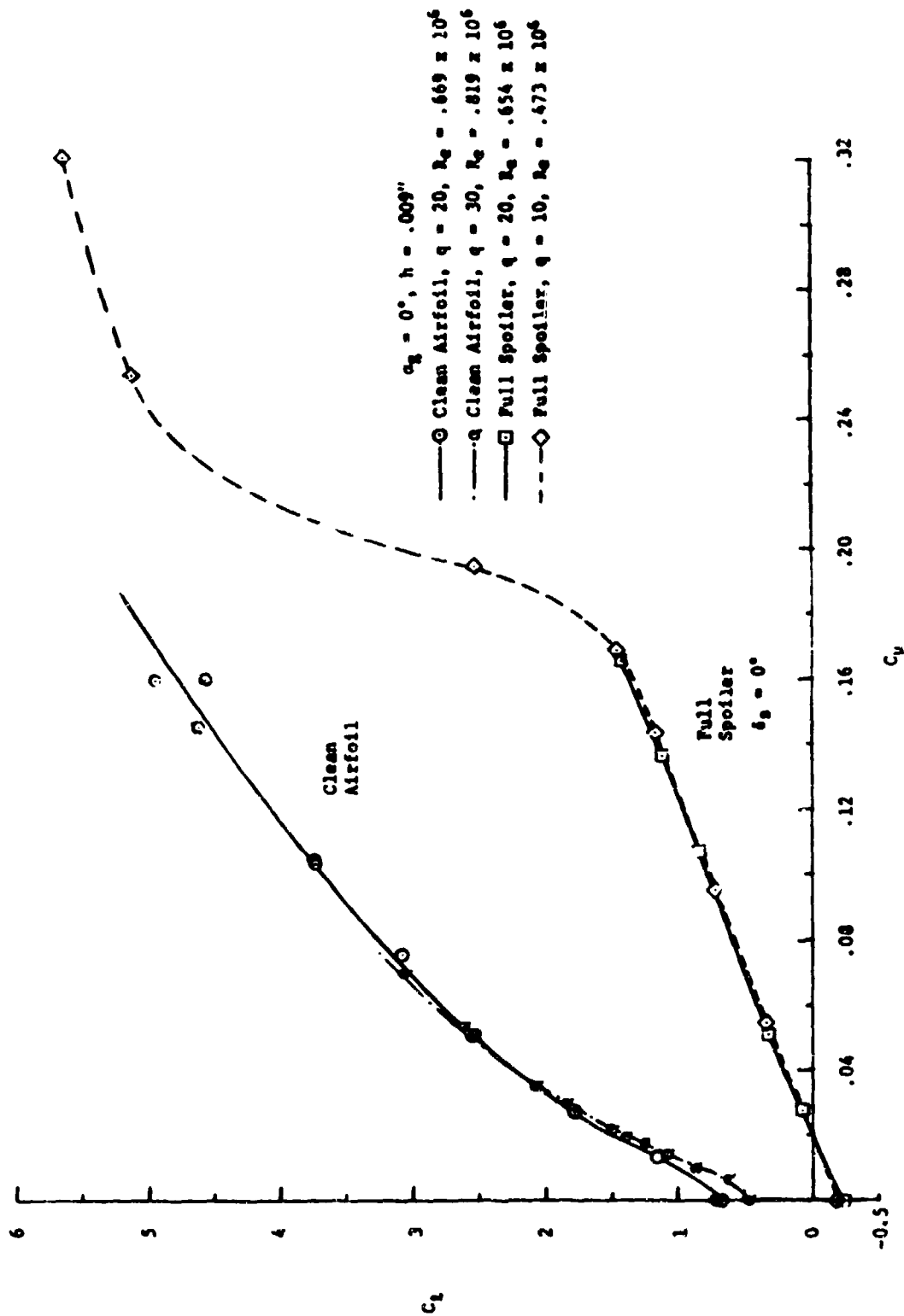


Figure 42 - Reynolds Number and Flow Reattachment Effects on Elliptical C.C.  
Airfoil with Spoiler

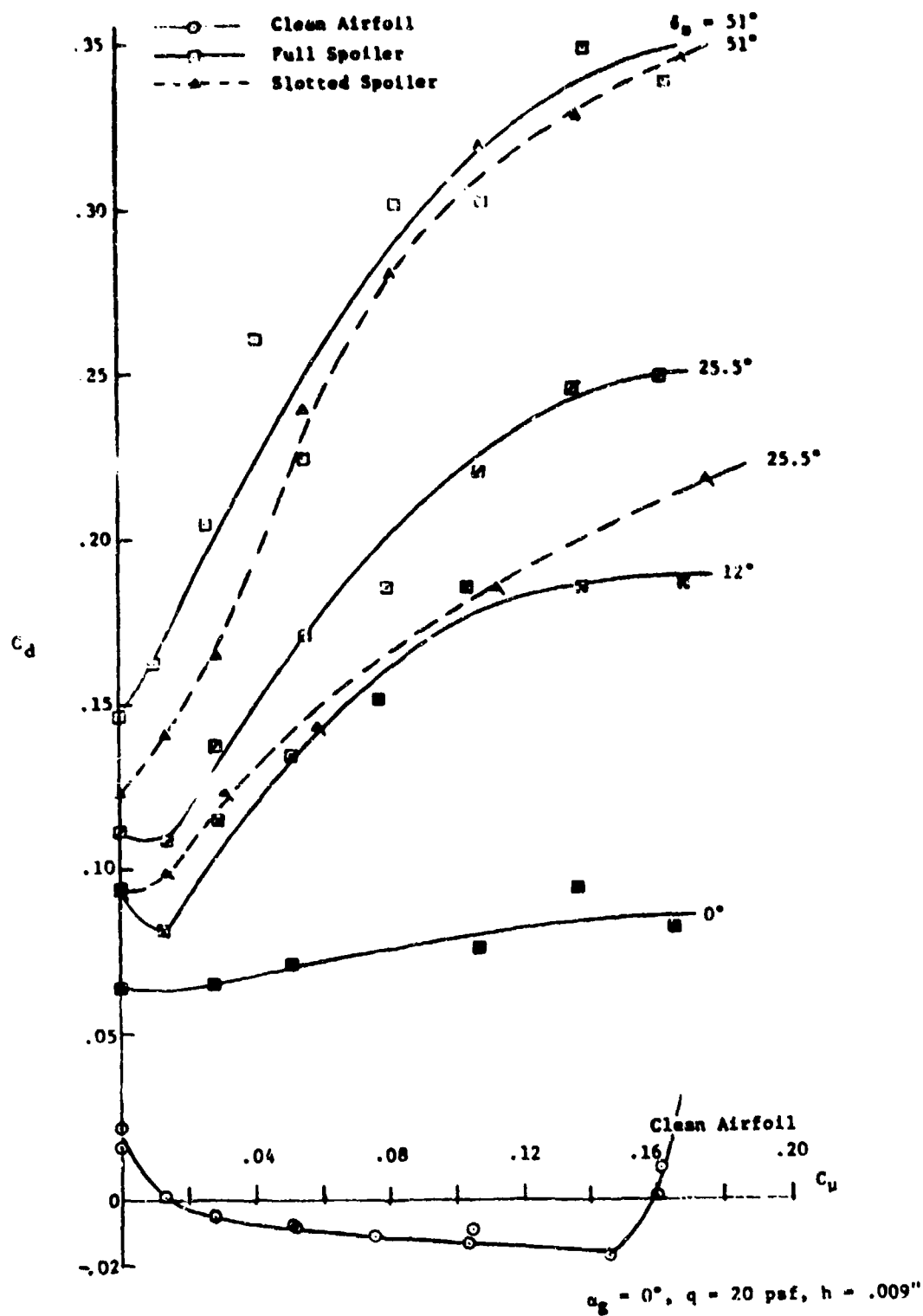


Figure 43 - Drag Increase due to Spoiler Deflection  
on Elliptical C.C. Airfoil

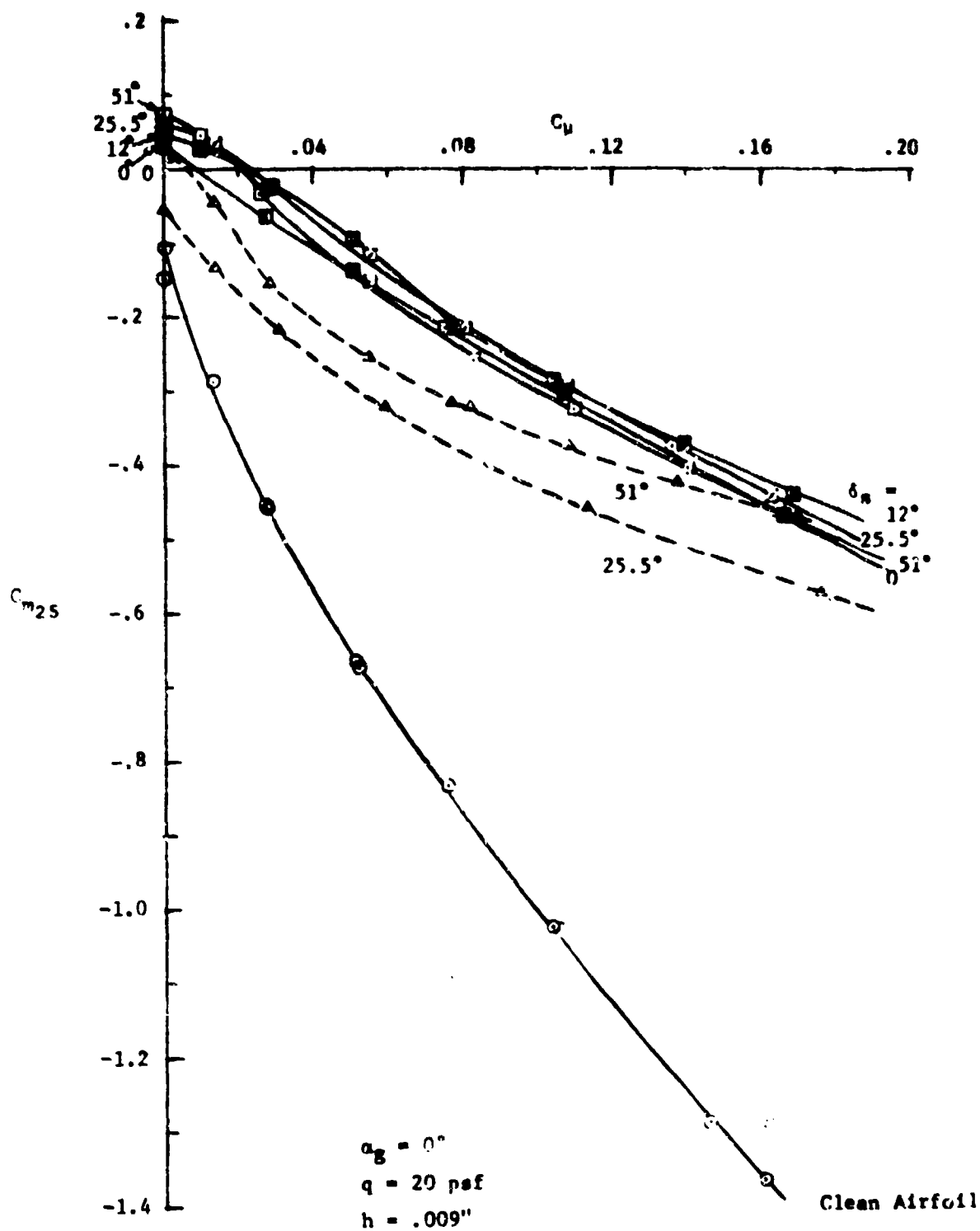


Figure 44 - Pitching Moment Variation with Spoiler Deflection